DYNAMIC MOTION DETECTION TECHNIQUES FOR MICROMECHANICAL DEVICES AND THEIR APPLICATION IN LONG-TERM TESTING

WONG CHEE LEONG
(B.Eng. (Hons.), NUS)

**A THESIS SUBMITTED
FOR THE DEGREE OF DOCTOR OF PHILOSOPHY**

**DEPARTMENT OF
ELECTRICAL AND COMPUTER ENGINEERING**

NATIONAL UNIVERSITY OF SINGAPORE

2010

ACKNOWLEDGEMENTS

The completion of my thesis marks the end of an extraordinary four-year journey in NUS. And while I reminisce about the many fond memories that I have gathered over these years, I would also like to express my appreciation to a host of wonderful people whose contributions have made these four years an enjoyable experience. I would first like to thank Dr. Moorthi Palaniapan, my supervisor, for his professional guidance throughout my reseach, without which this thesis would never have been possible. Special thanks also go out to the staff at the Center for Integrated Circuit Failure Analysis and Reliability (CICFAR), especially Mr. Koo Chee Keong and Mrs. Ho Chiow Mooi, whose support on the technical and logistics side has been invaluable in helping me to complete various aspects of my work.

During my time at CICFAR, I've also had the good fortune to be associated with a terrific group of students and colleagues. To my fellow group-mates Meenakshi Annamalai and Niu Tianfang, I am grateful for your ideas and your support in many of my experiments. My thanks to Wang Rui, Wang Ziqian, Jason Teo, Zhang Huijuan, Pi Can and Ren Yi. I have enjoyed our discussions about research, life and everything else in between. And to Meng Lei, Liu Dan and Huang Jinquan, I will always remember the great times we've spent together. Your friendships will be a lasting part of my memory.

I would like to thank my family, especially my parents Richard and Wendy, for their loving support over many years and for putting up with my perpetual student status. I attribute the fact that I have made it this far to their constant reminders to me to be persistent and hard-working. And finally, I wish to thank Sung Ying Ying, my best friend, who has always been there for me throughout these years. I am always grateful for her love, support and encouragement.

CONTENTS

ACKNOWLEDGEMENTS **i**

CONTENTS **ii**

SUMMARY **iv**

LIST OF TABLES **vi**

LIST OF FIGURES **viii**

LIST OF SYMBOLS **xii**

CHAPTER 1 INTRODUCTION **1**

1.1. Background 1
1.2. Objectives 4
1.3. Overview 5

CHAPTER 2 REVIEW OF TECHNOLOGIES FOR CHARACTERIZING DYNAMIC MEMS DEVICES AND THEIR APPLICATIONS **7**

2.1. Introduction 7
2.2. Laser-based techniques 8
2.3. Optical microscopy and optical stroboscopy techniques 13

2.4. Scanning electron microscopy 15
2.5. Electrical measurements 18
2.6. Applications in micromechanical resonator testing 20
2.7. Conclusions 34

CHAPTER 3 ACOUSTIC PHONON DETECTION FOR DYNAMIC MOTION CHARACTERIZATION IN MEMS DEVICES 36
3.1. Introduction 36
3.2. Acoustic phonon generation by dynamic MEMS structures 38
3.3. Piezoelectric sensing 47
3.4. Experimental setup 53
3.5. Proof-of-concept experiments on MEMS switches and resonators 60
3.6. Conclusions 74

CHAPTER 4 STROBOSCOPIC SCANNING ELECTRON MICROSCOPY FOR NANO-SCALE IN-PLANE MOTION MEASUREMENT 76
4.1. Introduction 76
4.2. Principle of stroboscopic imaging using SEM 78
4.3. Experimental setup 80
4.4. Stroboscopic imaging for measuring in-plane motion of micromechanical resonators 82
4.5. Conclusions 99

CHAPTER 5 LONG-TERM FREQUENCY STABILITY OF SILICON CLAMPED-CLAMPED BEAM RESONATORS 101
5.1. Introduction 101
5.2. Micromechanical comb actuated clamped-clamped beam resonators 103
5.3. Experimental setup 111
5.4. Long-term frequency stability measurements for clamped-clamped beam resonators 120
5.5. Conclusions 131

CHAPTER 6 CONCLUSION 133
6.1. Conclusion 133
6.2. Recommendations for future work 136

REFERENCES 138

LIST OF PUBLICATIONS 148

SUMMARY

This thesis describes the development of two techniques for detecting nano-scale motion of micromechanical structures which can potentially be applied for long-term MEMS device testing. The first technique, acoustic phonon detection, utilizes mechanical waves or phonons generated by surface interaction or energy loss during device actuation to sense motion. A piezoelectric element is employed to convert the generated phonons into an electrical signal which can then be used for measurement. Phonon detection is able to provide similar information on the short-term performance parameters of MEMS devices as more established electrical characterization techniques. In addition, as the detection signal arises from mechanical phenomena, phonon detection has the unique capability of being able to provide insight into device mechanical state. This is particularly useful for assessing long-term performance of MEMS devices since device mechanical state invariably changes over time. The technique is able to sense the vibration of state-of-the-art micromechanical resonators which exhibit sub-100 nm displacement.

The second technique, stroboscopic scanning electron microscopy (SEM), is a high resolution imaging method that can capture the in-plane motion of MEMS devices down to ~20 nm. Through secondary electron (SE) signal gating, it is possible to freeze the dynamic motion of a micromechanical structure and image it at its instantaneous position. The technique can further be applied to obtain a phase-resolved micrograph of the motion of the structure during actuation by ramping the phase delay of the gate signal while imaging. This capability is particularly handy if a graphic visualization of device motion is required. In addition, quantitative data, such as device

displacement, can also be derived from the micrograph. The current hardware implementation can achieve a displacement resolution of about 20 nm, limited mainly by the electron probe size, for motion frequencies up to 3.58 MHz. Further optimization can potentially allow the system to provide sub-10 nm imaging resolution.

Both techniques were employed to investigate the long-term behaviour of comb actuated clamped-clamped beam resonators. Fifteen random samples were tested, each over a 500-hour actuation period, and the results indicate that the long-term frequency stability of the devices is dependent on the magnitude of axial stress on the beam structure. From the measurements, it was established that a frequency drift of 1.233 Hz day^{-1} was induced in the samples for every 1 MPa of axial stress on the beam structure. The *Q*-factor and peak displacement of most of the samples remained fairly consistent throughout varying by less than 12% and 10% from their mean values respectively. More interestingly, three of the test samples exhibited possible signs of fatigue behaviour when their phonon dissipation properties were enhanced after several hundred hours of actuation. The enhanced dissipation gave rise to a 35% – 41% increase in the magnitude of the phonon voltage generated per nm of resonator displacement and also to a ~20% drop in the *Q*-factors of the three resonators. Such a change in the mechanical characteristics (i.e. phonon dissipation) of the device cannot be identified by current electrical testing methodologies.

LIST OF TABLES

Table 3.1. Summary of dimensions, physical and piezoelectric properties of the transducers used in the phonon detection setup [89]. The transducers are made from APC840 material. **57**

Table 3.2. Comparison of switch performance parameters that can be obtained by electrical testing and by phonon detection. × denotes parameter is not quantifiable by the technique. **64**

Table 3.3. Comparison of state-of-the-art micromechanical resonator characterization techniques with phonon detection. **69**

Table 3.4. Measured phonon coupling factor improvement provided by applying various filler materials in between sample and piezo sensor.......................**74**

Table 4.1. Ramp rate and phase resolution values for the micrographs in Fig. 4.5. ....**87**

Table 4.2. Standard deviation of the data points in the three resonator displacement..**89**

Table 4.3. Measured velocity values for the 8 resonator beam motion positions shown in Fig. 4.9. The deviation is the difference between the estimated and best fit values...**92**

Table 4.4. Average gray level intensity for all 512 y-pixels at 12 x-lines around the cut-off pixel (obtained from Fig. 4.4(b)). **97**

Table 4.5. Mean and standard deviation of gray level intensity variation caused by background noise for image captures performed using different t_{gate}. This variation translates into a pixel error during the displacement profile extraction. **97**

Table 4.6. Comparison of other techniques for measuring the dynamic motion of micromechanical structures with the stroboscopic SEM developed in this work. **98**

Table 5.1. Summary of some published studies on long-term performance of micromechanical resonators. **103**

Table 5.2. Summary of the fifteen devices used in these long-term stability experiments. The voltage-displacement gain was derived as described in Section 5.3.1. ....**121**

Table 5.3. Measured frequency drift $\partial f_0/\partial t$ of the twelve devices compared with the derived axial stress σ_T (calculated using Equation (5.9)) at 28 °C (301 K) on the clamped-clamped beam. The devices are arranged in order of axial stress with positive values denoting tensile stress and negative values denoting compressive stress. [1]The frequency drift of Devices R04 and R13 could not be determined as they displayed large f_0 swings during the actuation period (see Fig. 5.10). Data recording for these two devices was terminated at 120 hours. **122**

Table 5.4. Mean and standard deviation of the *Q*-factor and peak in-plane displacement of the fifteen devices over the 500-hour actuation period. The coefficient of variation *CV* is calculated using Equation (5.12). [1]Data recording for Device 04 and Device 13 was terminated at 120 hours. [2]Shows data recorded before bifurcation point. **127**

Table 5.5. *Q*-factor, in-plane displacement and voltage-displacement gain of Device R07, R10 and R14 before and after the bifurcation points for each device. **128**

LIST OF FIGURES

Fig. 2.1. A laser interferometry system for measuring out-of-plane motions of various MEMS devices [17]. **9**

Fig. 2.2. A typical laser Doppler vibrometer (LDV) setup [24]. **11**

Fig. 2.3. An optical microscopy setup with digital image capture capability for MEMS device characterization [34]. **14**

Fig. 2.4. SEM micrograph showing blurring of structural features due to device motion [35]. **16**

Fig. 2.5. Network analyzer setup for characterizing micromechanical resonators. ...**20**

Fig. 2.6. Temperature compensated micromechanical resonators which utilize α mismatch to counteract the negative thermal frequency shift resultant from Si material softening [66]–[67] **27**

Fig. 2.7. Reaction-layer fatigue model for silicon thin-film failure [75]. **32**

Fig. 3.1. Generation of mechanical waves or phonons during MEMS cantilever switch operation. **39**

Fig. 3.2. Clamped-clamped beam and actuation shape at fundamental frequency f_0. Phonon dissipation occurs at the anchor structures during device actuation. **42**

Fig. 3.3. A circular piezoelectric element with surface electrodes connected to a voltmeter. The axis convention is shown on the upper left. **49**

Fig. 3.4. Schematic of the phonon detection setup for MEMS devices. **54**

Fig. 3.5. Block diagram of the in-vacuum phonon detection test system for MEMS devices. **55**

Fig. 3.6. (a) Optical image of the MEMS switch and (b) electrical schematic diagram. **61**

Fig 3.7. Screenshot of voltage measurements recorded by the oscilloscope during ~2 cycles of switch operation. **62**

Fig. 3.8. SEM image of the clamped-clamped beam resonator. For this particular device design L = 480 μm and w = 6 μm, therefore the theoretical resonance frequency f_0 = 200 kHz. The anchor width W = 100 μm. **65**

Fig. 3.9. (a) Phonon waveform $V_{phonon}(t)$ generated by the resonator device actuated with DC bias V_B = 10 V and AC drive input v_d = 25 mV in a vacuum ambient (pressure ~10^{-3} Pa). The peak-to-peak voltage of the phonon waveform is 230 mV_{pp}. (b) Corresponding sinusoidal physical displacement of the device observed with stroboscopic SEM. The measured peak-to-peak displacement is 112 nm. **66**

Fig. 3.10. Frequency response of the resonator, actuated with DC bias V_B = 10 V and AC drive input v_d = 25 mV, obtained using phonon detection and stroboscopic SEM (displacement measurements). Both techniques predict the same resonance frequency f_0 = 212.653 kHz and Q-factor ~ 10,600 for the device. **67**

Fig. 3.11. ln (V_{phonon}) vs. ln (u) at various linear drive conditions. From the slope of the best-fit line though all the points, n ~ 1.0 indicating a linear first-order relationship between the two parameters.. **71**

Fig. 3.12. Phonon voltage vs. displacement plots for the sample at the three linear operating biases. From the best-fit line through all three sets of points, the average K is determined to be 2.246 mV nm^{-1}. **72**

Fig. 4.1. Schematic diagram of time-gated signal detection for stroboscopic imaging. **79**

Fig. 4.2. Block diagram of the stroboscopic imaging system. **82**

Fig. 4.3. SEM images showing the comb actuated resonator (labeled Device 1) used for measurement. (a) The overall resonator device. (b) 200X magnified image of the comb structures. Circled in white (arrowed) is the portion of the 6 µm support beam used for imaging. (c) The portion of the 6 µm beam circled in (b) at 10,000X magnification.. **83**

Fig. 4.4. Stroboscopic micrographs of 6 µm support beam at its peak velocity point captured using gate width t_{gate} of (a) 10 ns, (b) 30 ns, (c) 100 ns, (d) 300 ns, (e) 1 µs and (f) 3 µs.. **85**

Fig. 4.5. Micrographs captured with different gate delay ramp rates to show several cycles of resonator beam displacement in a single micrograph. (a) Ramp rate 2.4° s^{-1} – 1 cycle, (b) ramp rate 4.8° s^{-1} – 2 cycles, (c) ramp rate 9.6° s^{-1} – 4 cycles, (d) ramp rate 16.8° s^{-1} – 7 cycles and (e) ramp rate 21.6° s^{-1} – 9 cycles. The gate width t_{gate} for all the captures is 30 ns. **86**

Fig. 4.6. (a) A 512 pixel-wide gray level intensity lineprofile of *y-y'* in the stroboscopic micrograph (b). **88**

Fig. 4.7. Quantitative displacement plots (shown in white) for stroboscopic resonator imaging over (a) one (ramp rate 2.4° $s^{-1)}$, (b) four (ramp rate 9.6° s^{-1}) and (c) nine (ramp rate 21.6° s^{-1}) cycles of motion. The solid line shows the best-fit curve through the extracted data points. From (a), the fitted parameters for resonator peak displacement A_0 was 265 nm and the phase shift ϕ_0 was 127° (phase lead with respect to the AC drive signal). **88**

Fig. 4.8. Motion of 6 μm support beam (one cycle) captured using varying gate widths t_{gate} (a) 10 ns, (b) 30 ns, (c) 100 ns, (d) 300 ns, (e) 1 μs and (f) 3 μs. **90**

Fig. 4.9. Velocity profile (white curve) of resonating beam at 8 selected points of its motion. The peak velocity of the structure occurs at the point where the micrograph (Fig. 9(e)) shows the most blurring. From the best-fit curve, the estimated maximum velocity is 0.192 m s^{-1}. **93**

Fig. 4.10. 30 keV gold on carbon calibration micrographs (120,000X magnification) used for determining effective resolution of the S-3500 SEM: (a) Spatial resolution of ~20 nm for in-situ resonator experiments with working distance (WD) = 17.8 mm. (b) Best case resolution of ~10 nm with WD = 11.0 mm. **94**

Fig. 4.11. Actual 1 μs gate signal provided by the SR250 gated-integrator/boxcar averager compared with ideal. **95**

Fig. 5.1. (a) SEM micrograph of a specimen of the comb actuated clamped-clamped beam devices used in the long-term stability experiments. The devices were fabricated using the SOIMUMPs process. (b) Magnified image of the resonator anchor structures with W = 100 μm and w = 6 μm. The beam length L = 400 μm is shown in (a). (c) Cross-section schematic of the device showing the SOI structural layer and the substrate. **104**

Fig. 5.2. Variation of mode constant β with axial stress. The numerical solution predicts a non-linear relationship between β and the stress parameter. For small stresses, a linear approximation about the zero stress point can be applied. **107**

Fig. 5.3. f_0-temperature plot for Device R01. The temperature coefficient of resonance frequency TC_f of the device is determined from the slope of the linear best-fit line. The best-fit line is obtained using line regression by the method of least squares. In this case, the TC_f of Device R01 is –12.67 Hz $°C^{-1}$ or –73.87 ppm $°C^{-1}$. **109**

Fig.5.4. Automated phonon detection setup for monitoring the long-term stability of resonator devices. **112**

Fig. 5.5. Frequency response curve of Device R01 obtained using phonon detection at 28.6 ^{o}C and ~2 x 10^{-2} Pa. The device was actuated with V_B = 6.0 V and v_d = 30 mV. The measured f_0 = 171.589 kHz and Q = 10,200 as determined from the best-fit Lorentzian curve. **114**

Fig. 5.6. (a) Non-linear frequency response of Device R01 obtained by phonon detection (V_{phonon}) and by stroboscopic SEM (displacement) at 28.6 ^{o}C and ~2 x 10^{-2} Pa. The resonator was actuated at with V_B = 15.0 V and v_d = 60 mV. (b) Voltage-displacement relation of the phonon detector obtained using six points from both curves in (a). The gradient of the best fit equation (by linear line regression) gives the voltage-displacement gain of the detector for this particular device. **115**

Fig. 5.7. (a) Recorded f_0 of Device R01 over the 500-hour actuation period. The resonance frequency of the device has a substantial dependence on temperature, resulting in large fluctuations in the measured f_0. (b) Measured surface temperature of Device R01. This data was used to decompose the effects of temperature variations on f_0. The average surface temperature over the actuation period was ~27.9 ±1.8 °C. (c) Plot of temperature compensated f_0 after temperature effects have been decomposed. The frequency drift $\partial f_0/\partial t$ of Device R01, obtained using linear line regression, is –4.512 Hz day^{-1}. **118**

Fig. 5.8. Q-factor variation and in-plane displacement of Device R01 throughout the actuation period. The displacements were derived from the recorded phonon voltages at the resonance frequency f_0 using the voltage-displacement gain of 0.0780 mV nm^{-1}..**119**

Fig. 5.9. Graphical representation of f_0 drift vs beam axial stress for thirteen of the fifteen test devices (Device R04 and Device R13 were omitted). The slope of the linear-fit line suggests that an f_0 drift of 1.233 Hz day^{-1} is induced for every 1 MPa of stress acting on the clamped-clamped beam. **123**

Fig. 5.10. Temperature compensated f_0 variation of Device R13 over the first 120 hours of the actuation period. The device displayed periodic frequency swings of ~100 Hz throughout the actuation period. Compare with Fig. 5.7(c) which shows the compensated f_0 variation for a typical device......**125**

Fig. 5.11. Q-factor variation and phonon voltage V_{phonon} of Device R14 over 500 hours. Note the drop in Q-factor at the bifurcation point t = 406 hr. The concurrent observation of an increase in V_{phonon} prompted a recalibration of the voltage-displacement gain. It was found that the voltage-displacement gain this device increased from 0.0428 mV nm^{-1} to 0.0612 mV nm^{-1} (~43%) after t = 406 hr. **128**

LIST OF SYMBOLS

δ_i	Strain in the *i*-direction
σ_i	Stress in the *i*-direction
α	Coefficient of thermal expansion
ρ	Density
T	Temperature
E	Young's modulus
ω	Angular frequency
Q	*Q*-factor
f_0	Resonance frequency
ε	Dielectric constant
d_{ij}	Piezoelectric strain constant
Z	Acoustic impedance
R	Wave reflection coefficient
U	Wave transmission coefficient
κ	Phonon coupling factor
K	Phonon voltage-displacement gain
TC_f	Temperature coefficient of resonance frequency

CHAPTER 1

INTRODUCTION

1.1. Background

Rapid progress in microsystems technology in the past two decades has enabled the development of many microelectromechanical systems (MEMS) devices such as resonators, micromirrors, microswitches, etc. and the increasing application of these MEMS devices in electrical products and systems over the years is a testament to the growing acceptance of MEMS as a viable future technology. The automotive industry was the first to commercially embrace MEMS devices as early as the 1990s. MEMS airbag accelerometers [1], which replaced their bulky macro counterparts due to their small size, relative low cost and high degree of sensitivity, were the first devices that saw high volume application. Since then, MEMS fuel pressure sensors, air flow sensors and tire pressure sensors are just some of the new devices that have found their place in the modern automobile [2]. In the wireless domain, future developments may

see discrete passives such as RF-switches, high-Q resonators and filters be replaced by their RF-MEMS counterparts [3]–[5], offering significant space and cost savings and allowing smaller form factors for RF chips. Devices for applications in biomedical science, telecommunications, video projection and a variety of other fields have been proposed with some already in production. The global market for MEMS devices totaled US$7 billion in 2007 and is forecasted to reach US$15.5 billion by 2012 [6].

This mammoth growth in device development cannot possibly proceed without characterization tools. State-of-the-art MEMS device characterization tools typically utilize imagining or electrical measurements in order to measure motion parameters such as displacement and velocity. Currently, this has proven to be sufficient for functional assessment of the device and to evaluate its short-term performance. However, present tools do possess a common drawback in that they have limited capability when assessing device mechanical state. Mechanical energy dissipation, actuation force and contact surface tribology are some examples of mechanical phenomena which are also present during MEMS device actuation but are difficult to quantify using imaging techniques or electrical measurements. Therefore, it would be worthwhile to develop new testing methodologies that can detect changes in these mechanical phenomena and hence offer a different perspective on device performance from current characterization techniques. One possible application of such testing methodologies could be in the area of long-term device testing. Device long-term performance is an indication of reliability and ultimately quality, and is expected to grow in importance especially considering the increasing volume of MEMS devices that will eventually find their way into consumer products. The wear and tear in micromechanical structures that occurs during long-term operation will lead to changes

in various aspects of their mechanical state and having a test technique that can detect these changes will therefore be useful in assessing long-term performance.

Long-term stability tests are a key aspect of the device developmental process and are typically carried out with the purpose of identifying time-dependant failure mechanisms and establishing projected life estimates. The information provided by these tests is a quantitative measure of the reliability of a product, which in turn is a benchmark for product quality. Of the diverse array of MEMS devices currently available in the market, the long-term stability of micromechanical resonators appears to have the greatest scope for study. Silicon resonators are one of the latest micromechanical structures to make the leap form developmental stage to full-scale production. Oscillator products that encompass micromechanical resonators have shipped since 2007 and by 2009 have become ubiquitous, finding applications in many consumer electronic products. The take-up rate of silicon oscillators has been remarkable, leading to the technology being proclaimed as the heir to quartz in the US$5 billion timing market. Judging by these current trends, micromechanical resonators have a very bright future. While the short-term performance parameters of resonators are fairly well understood, precious little published work exists on their long-term stability and it is this particular issue which this work intends to address. Resonator long-term stability experiments documented thus far have utilized network analyzer measurements, which are sufficient to track frequency changes but, in fact, provide no additional mechanical information (such as energy dissipation) on device performance. This form of device testing has also been unsuccessful in identifying a failure mode for micromechanical resonators.

1.2. Objectives

This work first aims to develop a phonon detection technique for the characterization of MEMS devices. MEMS devices are known to exhibit phonon generation and dissipation mechanisms during actuation [7]–[9] and these have been studied in the context of maximizing device performance [10]. However, these generated phonons can also play a crucial role in functionality assessment as they carry information on the dynamic mechanical state of the device. This property is particularly useful for monitoring long-term performance since device mechanical state inevitably degrades with wear and tear. The concept of acoustic phonon generation and detection has been demonstrated elsewhere for characterizing IC devices [11]–[12], hence it is expected that it can be viably extended to motion detection of dynamic MEMS structures.

A high resolution imaging technique is also required for subsequent motion calibration of the phonon detection technique. The micromechanical resonators used as test structures in experiments in this work typically exhibit ~100 nm displacement when actuated in their linear modes and hence their motion cannot be imaged by conventional optical/laser methods which are diffraction limited (~0.5 μm resolution). A stroboscopic technique based on the scanning electron microscope (SEM) is proposed to achieve the required high resolution. The physical motion measurements obtained through imaging will be matched against the detected characterization signal from phonon detection for verification purposes.

The second objective of this work is to employ the phonon detection technique which has been developed to investigate the long-term stability of micromechanical resonators. This particular aspect is targeted for two reasons: one, the need for long-

term stability data by device manufacturers and two, the lack of said data. The specimen of choice for study is the clamped-clamped beam resonator. This particular device architecture, which has reported applications in frequency reference and signal processing [13]–[16], is structurally simple and fairly straightforward to theoretically model. Working samples can also be fabricated consistently and reliably using commercially available MEMS fabrication processes. It is anticipated that this testing methodology will provide information from a mechanical perspective which will complement the performance parameters provided by current reported studies carried out using conventional network analyzer measurements.

1.3. Overview

This thesis documents the development of a phonon detection technique that can be applied for long-term testing of micromechanical resonators. Chapter 2 examines a number of state-of-the-art approaches for characterizing the motion of MEMS devices to provide a comparison for the proposed testing methodology. A review of recent studies on short-term performance and long-term stability of micromechanical resonators is also presented.

The phonon detection technique which has been developed is detailed in Chapter 3. This chapter covers phonon generation mechanisms of dynamic structures and highlights the difference in the phonons generated by contact and non-contact mode MEMS structures. The theory behind piezoelectric sensing is discussed as it is the method which was used to detect the generated phonons. The chapter also presents

calibration experiments, error source analysis and proof-of-concept experiments on MEMS switches and resonators.

Chapter 4 introduces stroboscopic SEM for nano-scale motion measurement. The technique was developed in-house for the purpose of providing in-plane physical displacement measurements for the resonator samples. A modified form of this chapter was published in *Sensors and Actuators A* 138 (2007), 167. The technique was used extensively during calibration experiments for the phonon detection test setup.

The long-term stability studies on micromechanical clamped-clamped beam resonators are detailed in Chapter 5. Theory and modeling of clamped-clamped beam structures is first presented. Of notable interest is the influence of temperature on resonator frequency shift, an effect that must be decomposed when determining long-term frequency drift. A study on this subject, which was part of this work, was published in *Journal of Micromechanics and Microengineering* 19 (2009), 065021. The measured long-term stabilities of a number of sample devices are presented next. Some of the performance parameters monitored include resonance frequency, *Q*-factor, in-plane displacement and phonon dissipation. Observation of a possible form of resonator fatigue response is also discussed. Part of these results has been submitted for publication in *Measurement Science and Technology*.

CHAPTER 2

REVIEW OF TECHNOLOGIES FOR CHARACTERIZING DYNAMIC MEMS DEVICES AND THEIR APPLICATIONS

2.1. Introduction

Most MEMS devices are designed to display mechanical motion upon actuation. Microcantilevers and resonators exhibit in-plane or out-of-plane vibrations when excited by an AC drive signal, micromirrors are designed to flex and rotate during operation, while accelerometers function based on capacitive plate rotation, etc. Hence, MEMS device characterization focuses on detecting and measuring the displacement of the devices' moving parts.

This chapter reviews various techniques which have been designed for sensing dynamic motion in the micro-scale. These techniques can be broadly classified into four categories: laser-based techniques, optical methods, SEM imaging and electrical measurements. Laser-based techniques and optical methods have proven to be popular

measurement techniques because of their good performance, cost effectiveness and operational simplicity. The SEM is a high resolution option for imaging static structures that can be adapted for distinguishing dynamic motion. Electrical measurements can be carried out on packaged samples and are useful in the characterization of a variety of MEMS devices including switches and oscillators. Different implementations of these techniques will be presented in the following sections along with their strengths and associated drawbacks.

The application of some of these techniques to study various aspects of resonator behaviour will also be reviewed. Silicon micromechanical resonators have been selected as the subject of study due to their prospects as one of the most exciting emerging micromechanical technologies. The long-term performance of these devices has received far less attention than short-term parameters such as thermal frequency stability and phase noise. In addition, the current methods being utilized for long-term performance characterization reveal little about the change in mechanical state of the device over extended actuation. Hence, it is this lack of insight into the long-term mechanical performance of resonators that this work intends to address.

2.2. Laser-based techniques

Laser-based techniques have long been applied for accurately measuring the velocity and displacement of vibrating structures in many engineering applications. Due to the non-contact nature of these methods, measurements can be performed even on small structures without interfering with their operation. Hence, laser-based techniques are well-suited for MEMS characterization. In fact, both laser interferometry and laser

Doppler vibrometry (LDV) have been demonstrated for measuring the motion of a variety of microstructures including micromechanical resonators and cantilevers.

2.2.1. Laser interferometry

Laser interferometry utilizes wave inteference to detect device motion. In a typical interferometer system, a single laser beam is split into two identical beams, a measurement beam and a reference beam, by a grating or a partial mirror. Each of these beams will travel a different path before they are recombined at a detector. The path difference creates a phase difference between them and it is this introduced phase difference that generates an interference pattern between the initially identical waves. When the measurement beam interacts with a vibrating microstructure, a phase change in the beam occurs resulting in a corresponding change in the interference pattern. This change in the inteference pattern can be measured using a photodetector and the photovoltage generated is directly representative of structure displacement.

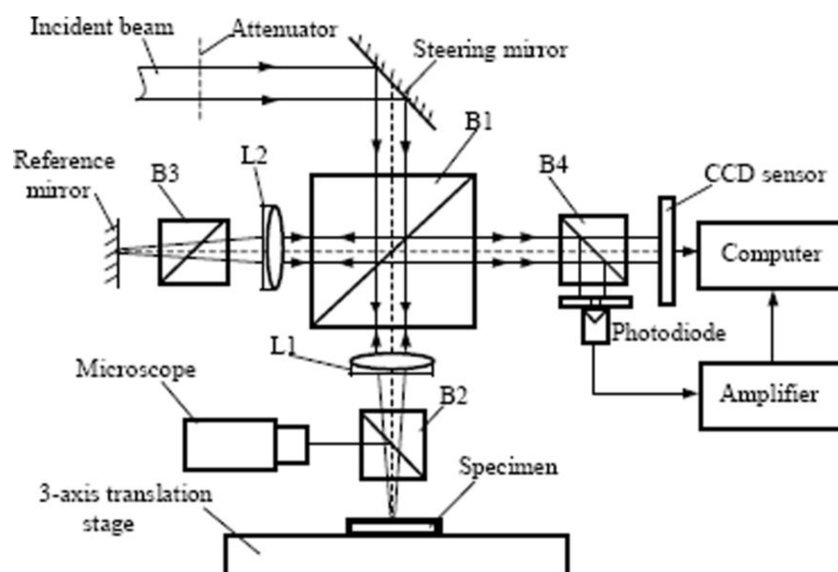

Fig. 2.1. A laser interferometry system for measuring out-of-plane motions of various MEMS devices [17].

Regular interferometer systems have been demonstrated for characterizing the out-of-plane motions of various MEMS structures such as microcantilevers [17] and switches [18]. These systems managed to achieve resolutions of up to 0.1 μm [17] and laser spot diameter (which determines in-plane spatial resolution) of ~10 μm. More sophisticated systems also incorporate stroboscopy for motion freezing by pulsing the laser source [19]–[20]. Stroboscopic optical interferometry systems which can characterize both the in-plane and out-of-plane motions of MEMS devices have also been reported [21]–[22]. These systems combine stroboscopic optical microscopy (which captures in-plane motion) and laser interferometry (for measuring out-of-plane motion) to achieve three dimensional motion characterization of the device-under-test (DUT). Image sequence processing by optical flow techniques, such as gradient methods, allow for out-of-plane measurement accuracies in the nanometer range [22] although in-plane spatial resolution is limited to ~2 μm due to light diffraction.

2.2.2. Laser Doppler vibrometry

LDV works based on the detection of the Doppler shift of coherent laser light that is scattered from a small area of the test sample. The sample scatters or reflects light from an incident laser beam and the Doppler frequency shift is used to measure the component of velocity which lies along the axis of the laser beam. An interferometric system is usually applied for extraction of the Doppler frequency information [23]. LDV can be applied to the dynamic evaluation of microstructure motion as the measurement system does not to impose undefined loads on the structure.

LDV systems or hybrid systems which incorporate the LDV for vibration measurements have grown increasingly popular due to the sensitivity and accuracy of the technique in detecting out-of-plane motion. In their work, Burdess et al. present a two-channel vibrometer system to measure sub-micron oscillations of micromachined structures at positional resolutions of approximately 10 μm [24]. The LDV unit in their system has a signal bandwidth of 150 kHz and a 0.6 μm s^{-1} velocity resolution over this bandwidth. A lateral resolution of ~5 μm was attained, limited by the laser spot diameter. This system was used to measure the dynamic characteristics of the microstructure including the mode shapes of vibration, modal damping factors and natural frequencies. LDV has also been applied by [25] to characterize the in-plane motion of comb actuated rotor/stator structures. In-plane displacement measurement was achieved by tilting the laser source and aiming the laser spot on exposed sidewalls of the structural layer.

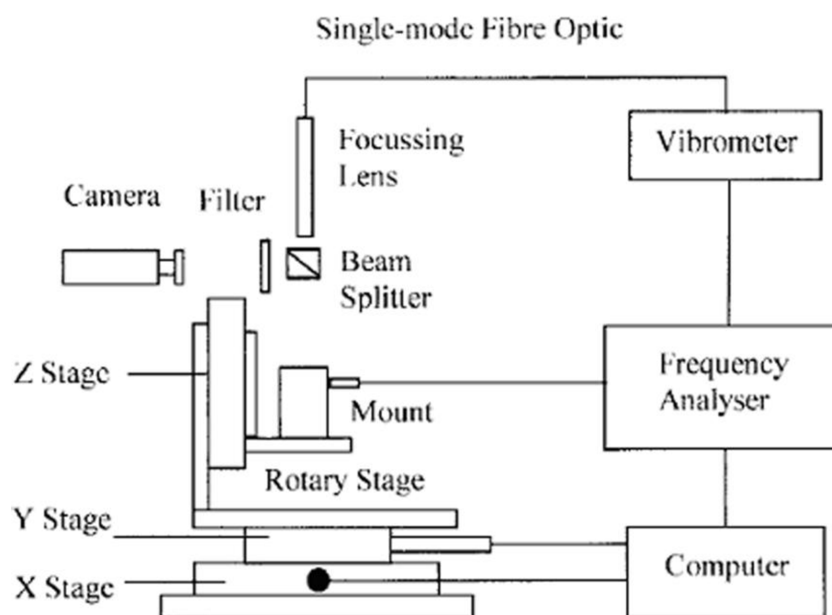

Fig. 2.2. A typical laser Doppler vibrometer (LDV) setup [24].

However, one major drawback of conventional LDV systems is that they are only able to perform point measurements and hence if measurements at multiple locations on the device are required, one has to physically move either the laser source or the sample. To overcome this issue, Vignola et al. have demonstrated a scanning LDV system which they have used to characterize the motion of micro-oscillators [26]. The laser spot was scanned over the sample surface by physically stepping the laser source with a mechanical sub-system. The typical achievable laser spot diameter was ~2.5 μm. Hybrid systems have also been proposed for improving the in-plane spatial resolution (laser spot diameter) capabilities of LDV. The confocal vibrometer microscope (CVM) demonstrated by [27] is essentially a LDV where its measurement beam is the laser beam of a confocal microscope. The confocal microscope component of the CVM system is able to reduce the laser spot diameter down to ~700 nm, allowing the CVM to characterize the out-of-plane motions of sub-micrometer devices. Out-of-plane resolution was claimed to be in the picometer (10^{-12} m) regime. The scanning function provided by the confocal microscope component also allows the system to map out-of-plane motion over the entire topography of the device.

Although laser-based techniques fair well in terms of measurement accuracy and throughput, a major downside is that laser probes utilize wavelengths in the visible spectrum. This, in effect, means that the lateral resolution of these techniques is diffraction limited to about 0.5 μm. Optical engineering methods, like confocal microscopy [27], would contribute minimal improvement to this resolution. Hence 0.5 μm is probably the best resolution the system can achieve. For direct imaging of the microstructure or its motion, optical microscopy is perhaps the most frequently used technique and this method is discussed next.

2.3. Optical microscopy and optical stroboscopy techniques

Optical microscopy and optical stroboscopy techniques are perhaps the most common and intuitive means of capturing dynamic micro-device motion. A typical optical setup for characterizing MEMS devices would feature a high-magnification light microscope whose optical output is linked to some form of image or video capture system (e.g. video camera). The resolution limits of these systems are determined primarily by the microscope lenses with aberrations in the lenses being the largest contributors to inaccuracies.

Measurement systems combining a conventional optical microscope with a charge-coupled device (CCD) camera have been presented to analyze the in-plane motion of MEMS structures [28]–[29]. A video recording of structural motion is first obtained and quantitative measurement data is then extracted using image processing techniques. Nanometer accuracy is achieved through sub-pixel extraction algorithms although spatial resolution (i.e. minimum resolvable feature size) is limited in the micrometer regime. The method of confocal microscopy is sometimes also utilized to improve the spatial resolution. The confocal optoelectronic holography microscope developed by [30] utilizes a confocal optical microscope and piezoelectric stepping (in the *z*-direction) to image MEMS structures. By applying back-end processing of the image data, they are able to generate 3D images of structures with micometer lateral resolution and nanometer depth resolution.

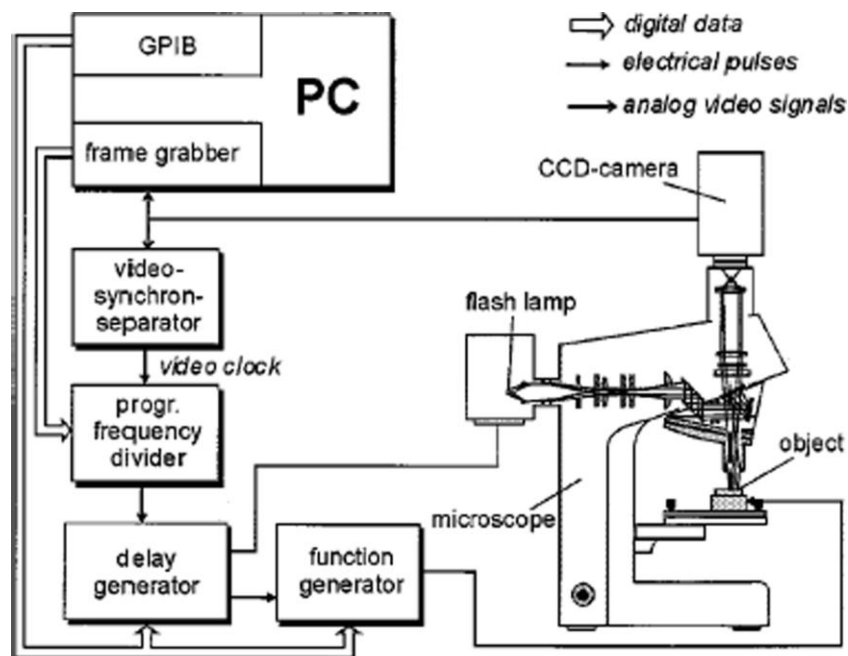

Fig. 2.3. An optical microscopy setup with digital image capture capability for MEMS device characterization [34].

Since measurement of dynamic motion is required when studying MEMS devices, most optical characterization systems also feature stroboscopic illumination for motion freezing. The stroboscopic effect is usually achieved by either blanking or pulsing the light source. Freeman has demonstrated optical microscopy with stroboscopic illumination to achieve bi-directional in-plane measurements of MEMS device vibrations [31]. Optical stroboscopy was also applied by Smith et al. in determining the resonant frequencies of a variety of MEMS actuators [32]. Both systems were able to detect device displacements in the micrometer regime. By performing sub-pixel processing on the images captured by their stroboscopic optical microscopy system, Davis et al. were able to attain displacement measurements of dynamic motion with nanometer accuracy [33]. However, their system is still limited to imaging devices with micrometer dimensions due to the spot diameter.

Applying the stroboscopic principle together with high-speed cine photomicrography, Rembe and Tibken have been able to optically visualize the motion of microrelays [34]. The technique features the use of an ultra high-speed CCD camera mounted on a powerful optical microscope to capture cinematographic image sequences of microstructure motion. The image sequences allow the measurement of the position with respect to time of the moving parts in the structure. If a dynamic model of the microstructure is available, these position data are used to estimate the model parameters. Stroboscopic illumination can also be added to the system during the analysis of very fast dynamic processes. The spatial resolution of this system is approximately 600 nm and is limited by the properties of the high-speed camera.

It should be noted that optical measurement techniques suffer from the same diffraction limits (best case spatial resolution is ~0.5 µm) as laser-based techniques since both utilize probe sources in the visible spectrum. These characterization methods may still be applicable in the short- to mid-term, however, as MEMS device dimensions continue to scale down, sub-micron imaging techniques, like scanning electron microscopy (SEM), will become more relevant.

2.4. Scanning electron microscopy

The scanning electron microscope (SEM) is a high resolution (down to 2 nm) tool for imaging specimens with sub-micron features. Although it is traditionally used to image static samples, it can be adopted for characterizing the dynamic motion of MEMS devices as well.

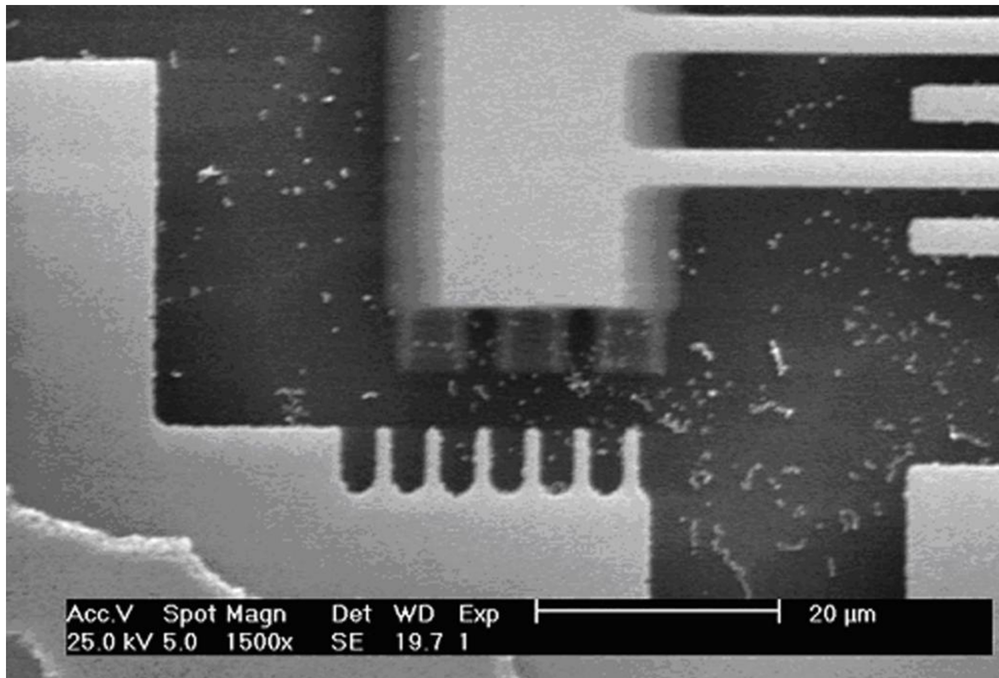

Fig. 2.4. SEM micrograph showing blurring of structural features due to device motion [35].

When imaging an actuating MEMS device, the lack of synchronization between the primary electron beam and MEMS device movement result in the device features showing up blurred in the final capture as shown in Fig. 2.4. The motion of the moving parts can be estimated from the edge blurring to provide a quantitative measure of the displacement (blur synthesis). In their work, Roy et al. applied this technique to the characterization of polycrystalline SiC resonators [35]. However, blur synthesis provides, at best, a rough approximation of the motion amplitude and its accuracy declines substantially when estimating small (nanometer) displacements. Furthermore, the actual motion of the structure cannot be ascertained from the image capture since the moving parts are blurred.

An alternative to blur synthesis was proposed by Pike and Standley in their work [36] where they utilized slow-scan SEM imaging (time-resolved digital sampling) to visualize the motion of a micro-seismometer structure. By slowing the SEM raster scan

rate to match the frequency of the structure's vibration, a time-resolved profile of its motion over a single period was obtained, from which quantitative displacement data was then extracted. However, the testing bandwidth is limited to a few hundred Hz as the required scan rate is too fast to provide images of sufficient quality for higher frequency devices.

More sophisticated SEM-based measurement systems employ some form of stroboscopy for motion freezing which not only improves the accuracy of the displacement measurements but also allows the visualization of structure movement. There are two typical methods to realize stroboscopy in the SEM. The first is to blank the primary electron beam as it scans the sample surface. The second is to gate the secondary electron (SE) signal, which has the advantages of simpler implementation and does not degrade the electron-optical performance due to primary beam blanking. Ogo et al. utilized SE signal modulation to implement a stroboscopic SEM for characterizing microcantilevers [37]. The implementation of stroboscopic SEM imaging, presented in Chapter 3, is also based on the concept of SE signal gating.

Other novel SEM-based measurement techniques include spot-mode measurement introduced by [38]. The electron beam is fixed at a static position at an edge of a moving part of the device and the SE signal is monitored using an oscilloscope. During actuation, device motion modulates the SE signal and this change in the signal level is representative of the motion. Prior calibration of the signal levels allows for quantification of device displacement while observing the SE signal magnitude. The authors have demonstrated the technique by performing displacement measurements

on microcantilevers. Similar measurement methodologies have been proposed by [39] and [40].

LDV, optical techniques and SEM measurements, although well-established and easily implementable, have the weakness of requiring a direct line of sight to the device under test. In the case of packaged devices, this would mean that decapsulation of the sample would be necessary before characterization, which may not always be desirable. In addition, the characterization signal is derived form the way the moving structural components interact with the laser, optical or electron probes (compared to a signal that is directly generated due to the motion itself). Hence, such a signal, while able to provide information on dynamic parameters such as displacement and velocity, offers no insight on the mechanical state of the test device. Next, electrical measurement techniques for sensing the motion of dynamic MEMS devices are reviewed.

2.5. Electrical measurements

Electrical tests are an important analysis platform for a large class of MEMS devices. However, while powerful electrical measurement tools exist to test their electrical behaviour, relatively few are available to measure micromechanical behaviour. Capacitive detection is perhaps the most commonly utilized methodology for electrical-based motion sensing, since most MEMS devices are electrostatically driven. Structural motion during actuation modifies the geometrical configuration of the capacitor plates in the device and hence the system displacement can be derived based on the change in capacitance. This change in capacitance can be measured by a capacitance meter. As only electrical contacts to the sample are required during

measurement, batch characterization for packaged devices is possible. Ferraris et al. applied this technique for characterizing their comb actuated stator/rotor structures [25]. The measured capacitances were verified with in-plane displacement measurements carried out using LDV.

In the case of resonant microstructures, sensing is often based on measuring the current induced by the relative motion of capacitive electrodes [41]. For electrostatic comb actuated resonators pairs, the sinusoidal motion of one resonator on actuation induces a change in capacitance in the static plate of its pair [42]. With this change in capacitance, a sense current is induced in the pair which can be detected and used to characterize the motion of the device. Resonance can be excited and detected using a network analyzer and an off-chip transresistance amplifier [43]–[44]. A network analyzer setup for characterizing micromechanical resonators is shown in Fig. 2.5. A DC polarization voltage V_P is directly applied to the resonator proof mass. The AC excitation v_d from the network analyzer is connected to the drive port. As the resonator starts to vibrate under periodic electrostatic force, the DC-biased time-varying capacitance formed between the resonator proof mass and the sense combs produces an output current i_0, which is subsequently converted to a voltage v_0 through the off-chip trans-resistance amplifier. Taking the ratio of v_0/v_d, the transmission response of the resonator can be obtained from the network analyzer measurement.

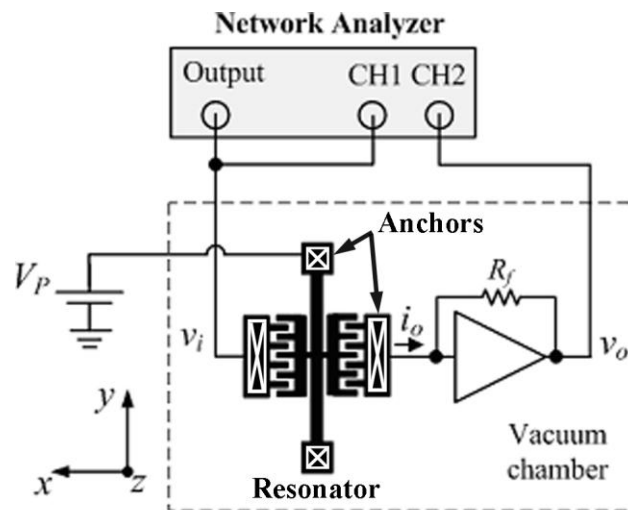

Fig. 2.5. Network analyzer setup for characterizing micromechanical resonators.

Capacitive detection has several key advantages over imaging techniques, including the ability to characterize both at the package and wafer level, parallel processing of devices and ease of implementation, which highlight its versatility and cost-effectiveness. Hence, it is one of the most commonly applied techniques in various MEMS device characterization studies. Some of these studies are reviewed in the following section. It is worth noting, however, that the technique invariably suffers from electrical parasitic effects such as the fringing capacitance [45] and feedthrough interference [46] which distort the measured frequency characteristics and hence give rise to errors in the measurements. Furthermore, the voltage-to-displacement conversion is highly based on mathematical equations and thus it cannot directly quantify device motion. There is also a lack of mechanical information from the electrical signal.

2.6. Applications in micromechanical resonator testing

The motion detection techniques discussed in the previous sections have the capability of sensing most forms of micro-mechanical motion and hence can be applied for

characterizing various MEMS devices including accelerometers, micro-motors, switches and resonators. However, silicon micromechanical resonators have been selected as the subject of study in this work due to their prospects as one of the most exciting emerging micromechanical technologies.

Silicon resonators are one of the latest MEMS structures to make the leap form developmental stage to full-scale production. The technological drive behind this transition is spearheaded by start-up companies such as Discera Inc. [47], SiTime [48] and Silicon Clocks [49], as silicon-based oscillators attempt to stake a claim in the US$5 billion timing industry currently dominated by quartz-based components. MEMS oscillator products have shipped since 2007 and by 2009 have become ubiquitous, finding applications in flat panel televisions, laptop PCs, networking equipment, cameras, phones, printers, set-top boxes and disk drives. The momentum that silicon timing has gathered in the past two years has shown that it has the potential, in time, to replace the legacy of quartz timing.

The recent rise of micromechanical resonators therefore represents an opportunity: studies on the performance of these devices will no doubt take on more significance since resonators have a long-term future. It is thus the aim of this work to develop techniques to assess certain aspects of resonator operation. While short-term parameters such as phase noise and temperature frequency stability are well-understood, long-term stability of these devices has received significantly less attention. Considering the importance of long-term stability data from a manufacturing standpoint, it is appropriate that this work should target measurement of long-term

stability parameters. The following sections review a selection of current work on both short-term and long-term parameters of micromechanical resonators.

2.6.1. Phase noise

Among the primary short-term stability concerns for MEMS oscillator systems is the phase noise. Phase noise can generally be defined as the frequency domain representation of rapid, short-term, random fluctuations in the phase of the waveform generated by the oscillator. An ideal oscillator would generate a pure sine wave. In the frequency domain, this would be represented as a delta function at the oscillator's frequency (i.e. all the signal's power is at a single frequency). However, real oscillators have phase modulated noise components and these phase noise components spread the power of the signal to adjacent frequencies, resulting in noise sidebands.

In a MEMS oscillator system, phase noise can arise due to instabilities either in the micro-mechanical resonator or in the oscillation sustaining circuitry or both. Therefore, a variety of phase noise reduction stratagies that target either one noise source or both have been proposed. For the resonator structure, phase stability can be improved by increasing the Q-factor of the device or by enhancing its power handling capability [45]. This is a fairly well-understood field considering the large body of work that has been published on the subject.

On maximizing Q-factor, this is typically achieved by minimizing energy loss mechanisms through optimized device design. More conventional resonator architectures such as capacitively-transduced beam [50] and folded-beam [51]

structures with Q-factors of ~13,000 in vacuum have been demonstrated. Novel designs including square [52]–[53] and disk [54] resonators, which operate in the bulk acoustic mode, are able to achieve substantially higher Q-values in excess of 98,000. Oscillators built with some of these resonators can achieve phase noise levels of –138 dBc/Hz [52], which meet the Global System for Mobile Communications (GSM) reference oscillator phase noise performance specifications. Oscillator designs incorporating the concept of enhancing power handling have also been presented. The series-resonant micromechanical resonator oscillator proposed by [55] features the use of three different resonator structures combined with some on-chip components to boost the overall power handling capability of the oscillator. The final phase noise of –125 dBc/Hz is close to GSM specifications. Other phase noise reduction techniques include tuning the electrode-to-resonator capacitive gaps via the use of atomic layer deposition as presented by [56]. By depositing hafnia (HfO_2) between the capacitive gaps of a disk resonator, the authors were able to increase the power handling of the device and reduce its phase noise.

Device characterization in the above mentioned studies were typically performed using capacitive measurements. The Q-factors were derived from network analyzer scans of the capacitively-generated currents at the device sense electrodes. In the case of phase stability, the power spectral density of the time-domain current signal induced at the sense electrode at resonance was studied to determine the phase noise. Phase noise in micromechanical oscillator systems is fairly well understood and therefore has much less scope for further study. Next, a second important short-term stability parameter is reviewed: temperature frequency stability.

2.6.2. Temperature frequency stability

One of the major issues micromechanical resonator manufacturers face is the frequency sensitivity to temperature of such devices. This frequency sensitivity is characterized by the temperature coefficient of resonance frequency TC_f of the resonator which is defined as the rate of change of frequency with temperature with respect to a reference frequency.

For resonators, in general, the TC_f is determined by the material properties of the device as well as the resonator geometry [57]. The two key material properties which influence the TC_f are the Young's modulus E_{Si} and thermal expansion coefficient α_{Si} of the resonator's silicon structural layer. E_{Si} was studied by Kahn et al. [58] for temperatures up to 450 °C and the measurements made were used to generate a second order polynomial fit,

$$E_{Si}(T) = 1.6806\times10^{11} - 8.2225\times10^{6}T - 5.9816\times10^{3}T^{2} \quad (Pa) \qquad (2.1)$$

where T is temperature. Hence, from Equation (2.1), E_{Si} has negative temperature dependence (i.e. E_{Si} decreases with increasing temperature) and this phenomenon is known as material softening. A decrease in the E_{Si} reduces the f_0 of the resonator and therefore material softening also contributes negative temperature dependence to the f_0 of the device.

The thermal expansion coefficient determines the rate at which the dimensions of the resonator expand at elevated temperatures. α_{Si} has been empirically measured to be 2.6 $\times$ 10^{-6} – 2.9 $\times$ 10^{-6} ppm $^{o}C^{-1}$ [59]–[60]. Expansion of the device dimensions causes an overall increase in the f_0, opposite to the effect of E_{Si}. However, the negative frequency

shift resultant from material softening is far more substantial than the contribution from α_{Si} and hence the overall TC_f of the resonator is dominated by the temperature dependence of silicon Young's modulus [57].

The geometry of the resonator has a bearing on the magnitude of stress the resonator structure experiences during heating which in turn also influences the TC_f of the device. Clamped-clamped beam resonators, in particular, are prone to axial stresses resultant from mismatch in thermal coefficients of expansion. These mismatches can occur at both the die level [57] (between the structural layer and the substrate of the resonator) and the package level [61] (between the resonator die and the IC package material). Depending on the type of stress induced, tensile stress tends to increase the f_0 while compressive stress reduces it [62], and its severity, the TC_f of the device is modulated accordingly. Hence, the various influences on the TC_f of clamped-clamped beam resonators can be summarized as,

$$TC_f \cong E_{Si}(T) + \alpha_{Si} + \sigma(T) \tag{2.2}$$

where $\sigma(T)$ is variation of axial stress with temperature. To find the TC_f of a resonator, the f_0 of the device is first recorded at various operating temperatures. The slope of the f_0-temperature plot gives the TC_f of the device. Due to its good measurement throughput and relative ease of implementation, the current dominant method for determining resonator TC_f is network analyzer [63]–[65].

Thermal frequency stability is a key issue when considering silicon-based oscillators for frequency reference and timing applications. Uncompensated resonators tend to display between –16 to –30 ppm $^oC^{-1}$ of frequency shift with temperature [63]–[65]

and this is in stark contrast to AT-cut quartz crystals, currently being used, which show less than 2 ppm $^{o}C^{-1}$ frequency drift. In order for resonators to even be considered for such applications, some form of temperature compensation must first be implemented. Compensation techniques for reducing the TC_f of resonators have been explored and can be categorized as either passive or active.

Passive techniques typically use a mismatch of coefficients of thermal expansion of different materials to induce stress in the resonator [66]–[67]. Fig. 2.6 shows two modified resonator structures designed for temperature compensation. The structure in Fig. 2.6(a) is fabricated with support beams which are longer than the resonator beam. At elevated temperatures, the support beams expand faster than the resonator beam, inducing a net tensile stress on the resonator beam in the axial direction. The resultant positive frequency shift induced by the tensile stress counteracts the negative frequency shift caused by material softening, hence reducing the TC_f of the device. The TC_f of the structure was measured to be –2.5 ppm $^{o}C^{-1}$ [66] and is a substantial improvement over uncompensated devices. The resonator structure in Fig. 2.6(b) is a stiffness-compensated microresonator. The resonator beam and overhead electrode are fabricated from materials with mismatched thermal expansion coefficients so that when heated, the overhead electrode expands upwards faster than the resonator beam. This results in an increase in the gap distance between the overhead electrode and the beam, reducing the electrical spring constant of the device. When this happens, the f_0 of the resonator increases, hence opposing the negative frequency shift caused by material softening. A TC_f of –0.24 ppm $^{o}C^{-1}$ was achieved [67], making the device almost temperature insensitive.

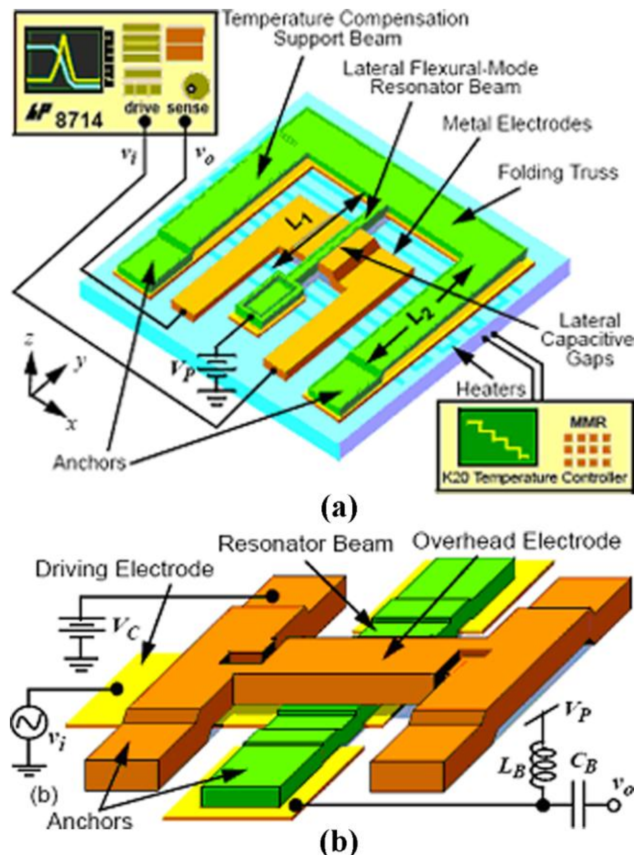

Fig. 2.6. Temperature compensated micromechanical resonators which utilize α mismatch to counteract the negative thermal frequency shift resultant from Si material softening [66]–[67].

Active temperature compensation techniques include electrostatic tuning [67]–[69] which utilizes electronic circuits to modify the bias voltage and tune the f_0 of the resonator. However, this technique is only applicable for resonators which display f_0 change with bias voltage variation. The I-shaped bulk acoustic resonators (IBAR) fabricated by [67]–[69] display resonance frequencies which can be tuned by 2580 – 4500 ppm when varying the DC bias. The resonators were closed-loop actuated and a temperature compensating bias generator circuit was designed to moderate the DC drive level and maintain f_0 with changing temperature. The compensated oscillator had a measured TC_f of –0.39 ppm $^{o}C^{-1}$ which is a 70 times improvement over an uncompensated oscillator [69].

Overall, the temperature performance of micromechanical resonators is a topic that has been well explored. Various oscillator product lines available from Discera, SiTime and Silicon Clocks already incorporate a range of temperature compensation techniques in order to meet the stringent temperature frequency stability specifications required by customer applications. Hence, future studies on this particular subject will have a lower return on investment of time and resource spent. Long-term stability issues, on the other hand, have been far less investigated. The importance of long-term stability information should not be understated since it describes the reliability of the resonator over its useful lifetime, which in turn is an indication of product quality. In the next section, some of the published studies on the long-term stability of micromechanical resonators are reviewed.

2.6.3. Resonator long-term stability

Long-term stability tests are typically carried out with the purpose of identifying time-dependant failure mechanisms and establishing projected life estimates. The information provided by these tests is a quantitative measure of the reliability of a product, which in turn is a benchmark for product quality. As oscillator devices based on micromechanical resonators transitions to manufacturing, as is the trend since 2007, long-term stability testing will become increasingly important since the data that these tests provide are an indication of device quality.

However, very few reliability studies on the long-term stability of micromechanical resonators have, so far, been published. Koskenvuori et al. are among the first to present such a study [70]. In their work, four length-extensional mode microresonators

were examined, two that were vacuum encapsulated and two control samples that were not. The four devices were housed inside a climate chamber and their frequency drifts were tracked over a 42-day actuation period (~1000 hrs) using a multi-channel network analyzer setup. It was found that the vacuum encapsulated devices showed substantially better stability (<1 ppm) compared to the non-encapsulated devices which displayed tens of ppm frequency drift. A second study by Kaajakari et al. featured eight resonators (four different designs) that were actuated continuously for 30 days using an external bias source. The transmission response of the devices was recorded at 5 min intervals using a multi-channel network analyzer. The devices were measured to have frequency shifts of 1 – 400 ppm month^{-1} depending on the device design [71]. It was noted by the authors that temperature fluctuations and package stresses can influence the frequency shift of the oscillators and hence their effects must be compensated for when determining the long-term frequency stability of the devices.

Kim et al. also demonstrate long-term frequency stability experiments on two different resonator types [72]. Six devices were continuously actuated for ~10000 hrs (>1 year) with their frequency characteristics measured every 30 min. Both device designs did not show significant frequency drift during the test period and frequency fluctuations of <4 ppm about the mean f_0 value was observed. Temperature cycling also did not degrade the frequency stability of the devices. The authors note the absence of burn-in frequency drift in the resonators which is a potential advantage over quartz crystals. A more recent study presented findings on the stability of aluminum nitride (AlN) ring resonators [73]. The four devices (of the same design) that were tested showed an average frequency drift of about 600 ppm over 760 hours. Frequency monitoring was carried out using network analyzer measurements. The authors speculate that the drift

was caused by silicone contaminants coming from their vacuum chamber being deposited onto the resonator structures.

The abovementioned studies offer valuable insights on the potential long-term frequency stability of various resonator designs as well as testing methodologies for investigating long-term resonator behaviour. However, there are three important aspects of current studies which future investigations should address. Firstly, it should be noted that very small sample sizes (two devices per design for [71], three devices per design for [72] and four each for [70] and [73]) were used in current studies, which may or may not reflect the true frequency stability of the particular resonator design. Secondly, a failure mode for micromechanical resonators has yet to be identified since the various samples used in the studies reviewed here show no signs of fatigue behaviour during testing. And thirdly, long-term stability tests have so far utilized network analyzer measurements, which are sufficient to track frequency changes but, in fact, provide no additional mechanical information (such as energy dissipation) on device performance. Since the failure modes of the resonators are expected to be in mechanical form (device operation is afterall mechanical in nature), it is perhaps prudent to also consider alternative testing techniques which have the capability of providing information on the long-term mechanical state of the device. Considering the importance of long-term testing for resonator manufacturing and the current lack of investigation on this particular subject, it is the aim of this work to develop techniques to study resonator long-term behaviour, specifically addressing the three points mentioned above.

Lastly, some of the published work on the fatigue behaviour of silicon structures undergoing cyclic stress (the structure of a vibrating resonator experiences cyclic

stresses during actuation) are presented. These studies are pertinent as they provide an insight on the possible failure modes or fatigue behaviour that may occur during long-term testing.

Possible failure modes

Although bulk silicon, being a brittle material, is not known to exhibit susceptibility to cyclic fatigue, micron-scale structures made from silicon films have been discovered to be vulnerable to degradation by dynamic fatigue – delayed fracture under applied cyclic stresses [74]–[78]. This is particularly relevant to micromechanical resonators since these structures are designed to undergo high frequency (kHz to MHz) cyclic displacement when actuated. Hence, fracture of the resonator beam after many cycles of actuation is a very possible device failure mode, although there have not yet been reports published on this occurrence.

The many proposed mechanisms explaining the dynamic fatigue of silicon are summarized in [79]. The two most widely discussed mechanisms are: reaction-layer fatigue [74]–[75] and mechanically induced subcritical cracking [76]–[77]. The reaction-layer fatigue model involves the silicon structure first undergoing cyclic stress enhanced surface oxide thickening and then environmentally assisted stress corrosion cracking. Fig. 2.7 details the failure process.

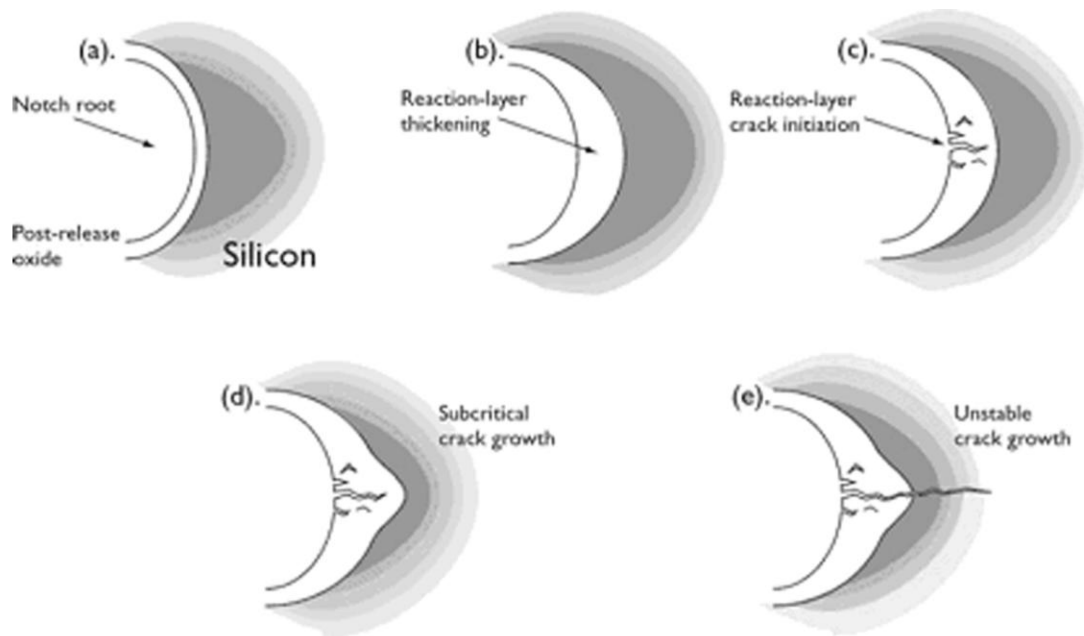

Fig. 2.7. Reaction-layer fatigue model for silicon thin-film failure [75].

The native oxide initially forms on the exposed silicon surface with a thickness and composition dictated by the environment and processing history. This oxide then thickens in high stress regions during subsequent fatigue loading and becomes the site for stress-corrosion cracks which grow stably in the oxide layer. Oxide thickening and sub-critical crack growth also tends to reduce the resonance frequency of the structure [80]. The process then repeats until a critical crack size is reached, whereupon the silicon itself fractures catastrophically by transgranular cleavage. The rate-dependence of this failure mechanism is dictated by the cycle-dependent oxide thickening process and the time-dependent, environmentally assisted, subcritical crack growth in this oxide layer [75]. Note that cyclic fatigue damage only occurs on the surface oxide which suggests that this failure mechanism is only applicable for structures actuated in an air or oxygen ambient.

The mechanically induced subcritical cracking model states that subcritical cracking occurs in the silicon itself when subjected to cyclic loads, particularly cyclic loads with

large compressive components [77]. Failure again occurs when a critical crack size is reached and the silicon fractures catastrophically. Subcritical cracking can take place in both vacuum and air environments. In an air ambient, surface oxide formation on mechanically induced subcritical cracks result in wedging effects that increase the applied stress intensity at the crack tips and speed up subcritical crack propagation and failure.

Prior knowledge of the possible failure modes of micromechanical resonators and the mechanisms behind them would certainly aid in designing experiments to study the long-term or fatigue behaviour of these devices. From the above mentioned mechanisms which describe silicon thin-film failure, it can be deduced that test ambient does have some influence over the time-to-failure (or cycles-to-failure) of the device, allowing accelerated testing methodologies to be designed. For example, air and high humidity test ambients should accelerate failure since oxygen and water vapour promote silicon dioxide formation. The experimental results by [74]–[78] also suggest that, in order for catastrophic fracture to occur, the thin-film must undergo very large cyclic stresses, usually several GPa. However, resonators operating in the linear (small signal) mode usually only experience structural stresses in the MPa range, a difference of 2 – 3 orders of magnitude. Hence, it would be unlikely to induce any form of mechanical cracking or fracture in resonators within a reasonable time period (<1000 hrs) unless they are actuated well into their non-linear regime (very large displacement amplitudes). These are some of the considerations which must be taken into account when designing experiments to study the fatigue behaviour of micromechanical resonators.

Of course, whether or not micromechanical resonators actually fail by structural fracture is still an open question since there is currently no publication on the observation of such phenomena. The truth of the matter is that there is still no known failure mode for resonator devices. It is therefore necessary for the long-term stability experiments to start from the very basic step of simply actuating sample devices under normal operating conditions and monitoring their performance for signs of fatigue. Once some form of fatigue behaviour is observed and the mechanism behind it is determined, it is then possible to further consider applying external stress (e.g. heat or humidity) to accelerate the fatigue behaviour and possibly induce a failure mode.

2.7. Conclusions

The review of motion sensing technologies in this chapter indicates that there currently exists a wide variety of techniques for characterizing dynamic micromechanical structures. Imaging techniques, such as LDV, optical microscopy and SEM, derive measurements form the way the moving structural components interact with laser, optical or electron probes. This is adequate for providing measurements on motion parameters such as displacement and velocity, but offers no insight on the mechanical state of the test device. Capacitive measurements, which are currently widely applied for characterizing electrostatically-actuated devices, suffer from the same deficiency. Hence, this work aims to develop a technique that is able to offer an alternative perspective on MEMS device performance (from a mechanical stand-point). Such a detection technique can find potential application in the long-term testing of micromechanical resonators. Micromechanical resonators are, at present, one of the most exciting emerging micromechanical technologies. Having just made the transition

to manufacturing in 2007, long-term stability data will become increasingly important in the product improvement process. Studying long-term stability with a characterization technique that can monitor the mechanical state of the resonator will hence provide complementary information to state-of-the-art network analyzer measurements. In addition, the different data might be useful in distinguishing time-dependent failure mechanisms that have yet to be identified by current long-term testing methodologies. Chapter 3 presents the phonon detection technique which has been developed in this work that can potentially provide information on device mechanical state. This technique is later applied in studies on resonator long-term stability.

CHAPTER 3

ACOUSTIC PHONON DETECTION FOR DYNAMIC MOTION CHARACTERIZATION IN MEMS DEVICES

3.1. Introduction

The current rapid progress in MEMS technology necessitates the development of tools for functionality and reliability assessment. As MEMS device actuation is mostly dynamic in nature, evaluating device performance typically involves measurement of micro-scale motion. State-of-the-art MEMS device characterization tools in general utilize imagining or electrical sensing in order to measure motion parameters such as displacement and velocity. While this is sufficient for assessing functionality, motion measurements offer little information on long-term performance or reliability. The wear and tear in MEMS structures that occurs during long-term operation leads to changes in various aspects of their mechanical state, such as mechanical energy dissipation, actuation force and contact surface tribology, most of which cannot be detected by current testing techniques. Hence, it becomes necessary to devise new

testing methodologies which can assess device mechanical state in order to complement current technologies for long-term device testing.

It is well-known that phonon generation and dissipation mechanisms such as thermoelastic dissipation (TED) [7] and anchor losses [8] exist for both silicon and amorphous carbon-based MEMS devices [9] and these have been previously reported in the context of maximizing device performance (e.g. increasing *Q*-factor in micromechanical resonators [10]). Since the phonons are generated as a direct result of device motion, they can be utilized for MEMS device characterization as well. Locally generated acoustic phonon detection has been utilized elsewhere for non-MEMS device applications [11]–[12] and therefore it is expected that it can be viably extended to micromechanical motion detection.

This chapter describes an acoustic phonon detection technique which has been developed for dynamic MEMS device characterization. The difference between the phonons generated by contact-mode and non-contact-mode MEMS structures is first highlighted. These phonons are used as the coupling mechanism through which information on the dynamic mechanical state of the device can be obtained. This information is particularly pertinent for long-term device testing since long-term operation (wear and tear) invariably alters the mechanical state of the device. Phonon detection is achieved via piezoelectric sensing. Practical considerations with regards to piezo sensor selection and maximizing phonon transmission from device to sensor are described. Some proof-of-concept experiments carried out on MEMS switches and resonators are also presented.

3.2. Acoustic phonon generation by dynamic MEMS structures

Despite the large variety of MEMS structures currently available, these structures can be broadly classified into two categories: contact-mode and non-contact-mode structures, for the purposes of analyzing their phonon generation characteristics. The fundamental difference between the phonons that can be detected from these two types of devices lies in the nature of the motion exhibited during actuation. These are discussed in the following sections.

3.2.1. Contact-mode MEMS structures

Contact-mode MEMS structures can be defined as structures whose operation entails some form of surface-to-surface contact. Some examples include MEMS switches, where the closing of the switch typically involves the coming together of a free standing cantilever with a contact electrode on the substrate, and micro-mirrors, where rotating and tilting the mirror causes the hinges to twist and flex and hinge surfaces to abrade against each other.

Consider the case of the MEMS switches. When the cantilever beam contacts the immobile substrate electrode during switch closing, an energy transfer takes place at the area of contact as the moving beam is brought to a sudden stop. This scenario is depicted in Fig. 3.1. The energy transferred to the electrode works to deform the area of contact thereby applying a stress on the electrode.

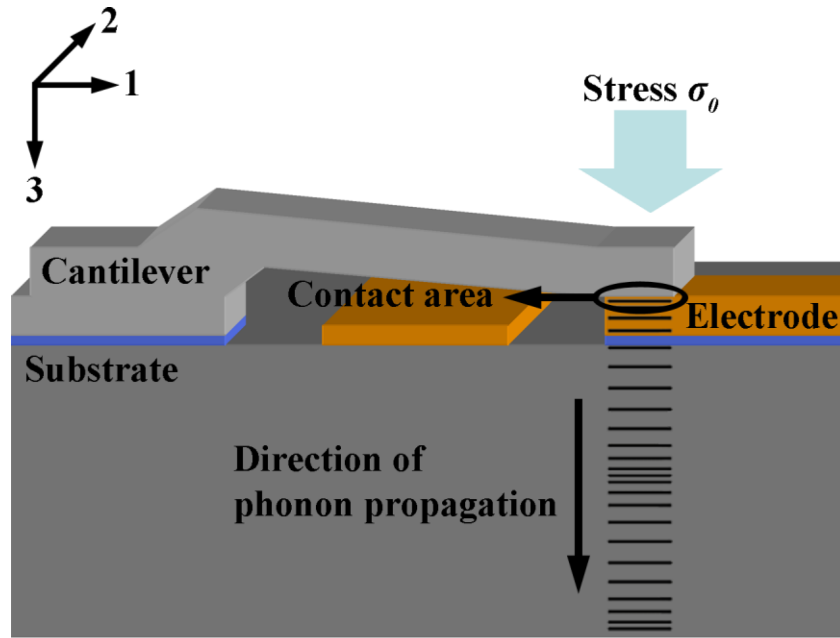

Fig. 3.1. Generation of mechanical waves or phonons during MEMS cantilever switch operation.

Taking the electrode/substrate as a 1-D elastic medium, wave theory suggests that the stress exerted on the surface of the substrate results in the generation of compressional waves that propagate through the substrate bulk. The motion of these waves is governed by the one-dimensional wave equation [81],

$$\frac{\partial^2 u_3}{\partial t^2} = \alpha^2 \frac{\partial^2 u_3}{\partial x_3^2} \tag{3.1}$$

where u_3 describes the x_3-component of the displacement field of the wave propagating in the x_3 direction. The wave velocity α is given by,

$$\alpha = \sqrt{\frac{E}{\rho}} \tag{3.2}$$

where ρ is the density and E is the Young's modulus of the material. Suppose the stress exerted on the surface of the substrate during a single operating cycle (switch-close at $t = 0$ followed by switch-open at $t = t_0$) can be described by $\sigma_{33} = \sigma_0 P(t)$, where $P(t)$ is a simple square function defined by,

$$P(t)=\begin{cases}0 \text{ when } t<0\\ 1 \text{ when } 0\le t\le t_0\\ 0 \text{ when } t>t_0\end{cases} \tag{3.3}$$

The displacement field u_3 generated in the substrate bulk due to the stress σ_{33} can be found by treating the substrate as an elastic half-space and solving Equation (3.1) with the boundary condition,

$$\frac{\partial u_3}{\partial x_3}(0,t)=\frac{\sigma_0}{E}P(t) \tag{3.4}$$

The resulting displacement field of the compressional wave propagating in the substrate is,

$$u_3(x_3,t)=-\frac{\alpha\sigma_0}{E}\left(t-\frac{x_3}{\alpha}\right)P\left(t-\frac{x_3}{\alpha}\right) \tag{3.5}$$

There are two things that are immediately apparent about u_3. First, the displacement magnitude is directly proportional to the applied stress σ_0 and second, the shape of the generated wave displacement field is dependent on the stress function *P(t)*. Since the stress function is resultant from the way the cantilever contacts the electrode/substrate surface, the above two observations imply that the generated wave is, in theory, a direct representation of the motion that occurs during switch operation. Information that can be obtained from the generated compressional wave include the switching force, which can be deduced from the wave amplitude since u_3 is proportional to σ_0, and tribological properties such as contact surface wear [82], since these phenomenon would invariably alter the stress function *P(t)*. For structures which also exhibit flexural motion during actuation, shear waves are generated as well and the displacement field of these waves can be similarly derived using Equation (3.1) and

appropriate boundary conditions. Due to the principle of wave particle duality, these compressional and shear waves are also known as phonons.

Therefore, the dynamic motion of contact-mode MEMS structures result in the generation of mechanical waves (compressional or shear waves) or phonons that are directly representative of the nature of their motion. These waves carry useful mechanical information, such as the switching force, contact surface wear and bounce, and can, hence, be utilized to characterize the motion of these structures. However, in the case of non-contact-mode MEMS structures, mechanical waves are generated via a different mechanism, which will be discussed in the following section.

3.2.2. Non-contact-mode MEMS structures

The motion of non-contact-mode MEMS structures, on the other hand, does not involve any form of surface interaction. The most basic instance of such a structure is the resonator, which generates sinusoidal vibrational motion when actuated. A typical resonator design is the clamped-clamped architecture, as shown in Fig. 3.2, which features a free-standing beam that is anchored to the substrate at both its ends. When a sinusoidal driving force, at the resonance frequency f_0 of the beam, is applied to the structure, another class of mechanical waves known as bending waves are excited within the structure which causes the entire beam to vibrate in the fundamental mode at f_0. However, since beam motion is completely restricted at the anchors, the bending waves generated during actuation are confined between the anchors and do not propagate outside of the clamped-clamped structure.

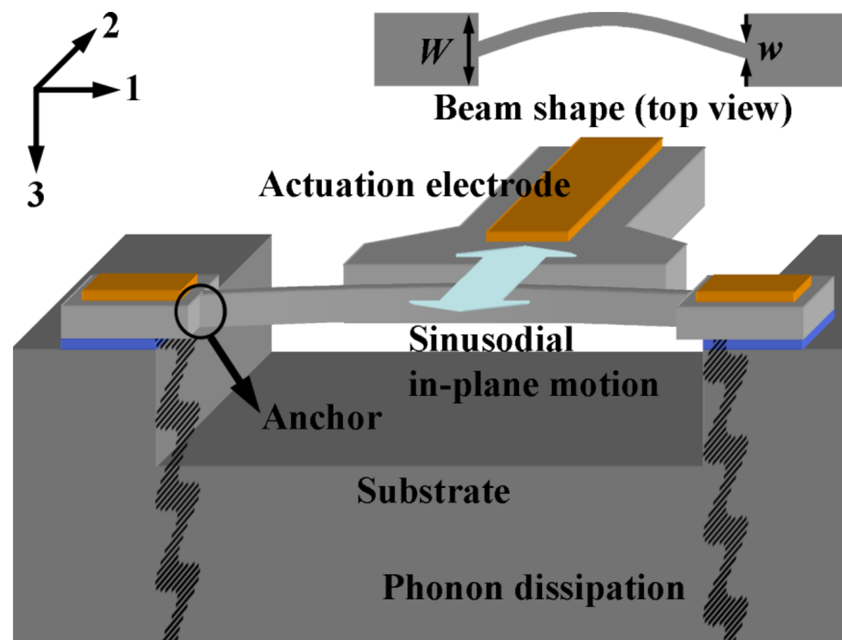

Fig. 3.2. Clamped-clamped beam and actuation shape at fundamental frequency f_0. Phonon dissipation occurs at the anchor structures during device actuation.

Of course, the bending waves can still be utilized for motion characterization by directly measuring the amplitude of the beam deflection via an optical or SEM imaging technique. Nevertheless, there is, in fact, a simpler approach which does not involve the use of optical or electron beam probes. Micromechanical resonators are known to exhibit a few types of energy loss mechanisms (which limit the maximum achievable Q-factor) and these are namely air damping [83], thermoelastic dissipation (TED) [7] and anchor losses [8]. Both TED and anchor losses will result in the generation of mechanical waves or phonons in the substrate and detecting these phonons is a possible method for motion characterization.

TED in resonant structures is a fairly well-understood phenomenon and current theoretical formulations [7],[84] of the problem are based on Zener's general theory. The theory states that, due to energy losses through thermoelastic damping, the upper limit of the Q-factor of a resonant beam can be approximated by,

$$Q_{TED} = \left(\frac{c_p \rho}{E \alpha^2 T_0} \right) \frac{1 + (\omega \tau)^2}{\omega \tau} \quad (3.6)$$

where c_p is the specific heat capacity, ρ is the density, E is the Young's modulus, α is the coefficient of thermal expansion, T_0 is the equilibrium temperature of the beam and ω is the angular frequency of mechanical resonance. τ is the time constant for temperature decay and is given by,

$$\tau = \left(\frac{w}{\pi} \right)^2 \frac{c_p \rho}{C_T} \quad (3.7)$$

with w being the width of the beam and C_T is the thermal conductivity.

The Zener theory appears to work well for simple beams and has been experimentally verified by [85]. The resonator samples used in subsequent experiments in this work are indeed simple silicon clamped-clamped beam structures (refer to Sections 4.4 and 5.2 for detailed descriptions of the devices) and hence their TED properties can be described using Equation (3.6). Consider a resonator design with beam thickness $w = 6$ μm and nominal f_0 ~ 200 kHz, Q_{TED} works out to be ~97,000. However, the average measured Q-factor of the test samples obtained during later experiments is ~15,000 (see Table 5.2) indicating the presence of another more dominant energy loss mechanism in these devices. As the devices were tested at low pressure (in vacuum), air damping is expected to have nominal contribution to energy dissipation and hence it can be deduced that anchor losses is the major loss mechanism for the clamped-clamped beam resonators used in this work. Therefore, phonon generation from these resonator test structures will be modeled based on anchor losses.

Theoretical studies [86]–[87] have shown that, although bending waves do not propagate beyond the anchors, the motion of clamped vibrating beams does result in the transmission of other mechanical waves at the anchor points. The reason for this is that although the displacement fields at the end face of the beam are zero during vibration, the stress fields are not and it is these stress fields that are the radiation sources of mechanical waves into the substrate. Since these transmitted mechanical waves carry energy away form the vibrating system, this form of energy transmission is therefore termed as anchor losses. It is interesting to note that the transmitted waves also hold information about the motion of the source, i.e. the vibrating beam, and hence are ideal for beam motion detection.

Consider a 1-D clamped-clamped beam of width w with a rectangular cross-section, anchored to the substrate by rectangular blocks of width W (as shown in Fig. 3.2). When actuated to vibrate, the bending waves generated in the beam structure is governed by the one-dimensional equation [81],

$$\frac{\partial^2 u_2}{\partial t^2} = -\frac{EI}{\rho A}\frac{\partial^4 u_2}{\partial x_1^4} \tag{3.8}$$

where E is the Young's modulus and ρ is the density of the beam material, A is the cross-sectional area and I is the moment of inertia. For a beam with rectangular cross-section, $I = Aw^2/12$. u_2 describes the x_2-component of the displacement field of the wave propagating in the x_1 direction.

Take a sinusodial incident wave traveling towards the anchor with in-plane displacement $u_2 = e^{i(kx - \omega t)}$, the boundary conditions at the anchor ($x_1 = 0$, see Fig. 3.2) are,

$$u_2 = 0$$
$$\frac{\partial u_2}{\partial x_1} = 0 \tag{3.9a}$$

However, at $x_1 = 0$ there must be continuity of the displacement u, rotation angle $\partial u_2/\partial x_1$, total moment $-EI\partial^2 u_2/\partial x_1^2$ and total force $-EI\partial^3 u_2/\partial x_1^3$. Hence, two additional boundary conditions must be applied [86],

$$\frac{\partial^2 u_2}{\partial x_1^2} = -2(1+i)k^2$$
$$\frac{\partial^3 u_2}{\partial x_1^3} = -2(1+i)k^3 \tag{3.9b}$$

where k is the wave number of the incident bending wave. These two boundary conditions suggest the presence of an alternating momentum/force (resulting in alternating stress fields) at the anchor which is directly resultant from the sinusoidal vibration of the beam structure. Solving the wave equation (Equation (3.8)) with these boundary conditions yields [86],

$$u_2(x_1,t) = \begin{cases} \left[e^{ikx_1} + ie^{-ikx_1} - (1+i)\, e^{kx_1} \right] e^{-i\omega t} & x_1 < 0 \\ \dfrac{2}{\left(\sqrt{W/w}\right)^3} \left(e^{ikx_1} - e^{-kx_1} \right) e^{-i\omega t} & x_1 > 0 \end{cases} \tag{3.10}$$

This solution suggests that in the beam structure ($x_1 < 0$), there exists three waveforms: the incident wave $e^{i(kx - \omega t)}$, a reflected wave $ie^{-i(kx + \omega t)}$ and an evanescent wave $(1 + i)e^{(kx - i\omega t)}$ that decays exponentially. More interestingly, in the rectangular anchor block ($x_1 > 0$), a transmitted transverse wave and an evanescent wave are also found, with the amplitudes of both these waveforms being inversely proportional to the cube of the ratio $\sqrt{W/w}$. The implications of this solution are that the bending waves generated by the vibrational motion of the beam also causes the transmission of transverse waves

into the anchor structures and the amplitude of the transmitted waves is proportional to the dimensions of the beam and anchor.

From the solution, it can be deduced that the transmitted transverse waves maintain the vibration characteristics of the radiation source, i.e. there is no frequency change or phase shift during transmission, and are therefore representative of the sinusoidal motion of the source. Hence, information such as the frequency and the phase of the vibrating beam can be obtained simply by detecting these transmitted waves, without having to measure the actual bending waves that are resultant from beam motion. It is also worth noting that the magnitude of the transmitted waves is dependent on the ratio W/w. For very large anchor structures, where $W >> w$, $W/w \rightarrow \infty$ and the magnitude of the transmitted waves goes to 0. This is a reasonable result as the wider the anchor width W, the stiffer the anchor structure and hence a significantly larger stress field is required to excite transverse waves within it. However, in practical devices, due to dimensional constraints, W/w is typically finite and hence energy loss by the vibrating resonator through the transmission of these transverse waves is expected. The magnitude of the bending wave displacement (i.e. the deflection amplitude of the beam) can hence also be deduced from the transverse wave amplitude, albeit scaled by a factor of $\frac{2}{\left(\sqrt{W/w}\right)^3}$.

In contrast to contact-mode MEMS structures, where mechanical waves directly generated by the interaction of surfaces can be used to characterize structural motion, motion characterization of non-contact MEMS devices can be carried out by measuring the energy loss, through the transmitted waves, by these structures. The

information that can be obtained from the transmitted waves includes the frequency, phase and amplitude of vibration. Both cases involve the detection of mechanical waves or phonons, albeit generated by different mechanisms. A common technique to achieve this is to utilize piezoelectric materials – materials that produce an electrical signal in response to applied mechanical stress. The concept of piezoelectric sensing is discussed next.

3.3. Piezoelectric sensing

Piezoelectric materials possess the ability of converting mechanical stress into electric charge. Common instances of such materials include crystals, such as tourmaline, quartz and topaz, and certain types of ceramics [88]. Peizo materials are highly sensitive to minute changes in stress/pressure, making them ideal as sensing elements for mechanical waves or phonons. In effect, phonons are material perturbations in an elastic medium generated by changes in stress fields propagating through the medium. By placing a peizo sensor below a phonon source, such as an actuating MEMS switch or resonator, the mechanical waves transmitted across the source/sensor interface give rise to stress fields in the piezo element which in turn induces a voltage across the sensor. This voltage can then be utilized as a signal for motion characterization. In the following sections, the structure and operation of piezoelectric ceramics, such as lead zirconate titanate (PZT) which is used in the phonon detection system, will be discussed. Equations relating the conversion form stress to voltage in piezo sensors will also be presented.

3.3.1. Piezoelectric ceramics

A piezoelectric ceramic is typically a mass of perovskite crystals with each crystal being composed of a small tetravalent metal ion placed inside a lattice of larger divalent metal ions and oxygen [88]. In the case of lead zirconate titanate (PZT), the divalent metal is lead and the tetravalent metal is a mixture of zirconium and titanium (the composition being dependent on the required peizo characteristics). At temperatures below the Curie temperature, each crystal has tetragonal symmetry and with it an associated dipole moment. However, as the dipoles of each crystal is in a random direction, the moments cancel out, giving rise to zero net polarization for the material.

Before a piezo ceramic element can be applied as a sensor, it must first undergo a poling process whereby the element is heated to a temperature slightly below the Curie temperature and exposed to a strong DC field. This results in most of the dipoles in the crystals being aligned in a particular direction, giving the element a permanent net polarization. This permanent net polarization, also known as the remnant polarization, makes the element permanently elongated and possessing an initial poling voltage in the direction of polarization. Now, mechanical tension or compression on the element alters the dipole moment associated with the element and creates a change in the poling voltage. Compression in the direction of polarization causes more dipoles to be aligned which in turn generates a voltage with the same polarity as the poling voltage. Tension, on the other has, has the opposite effect.

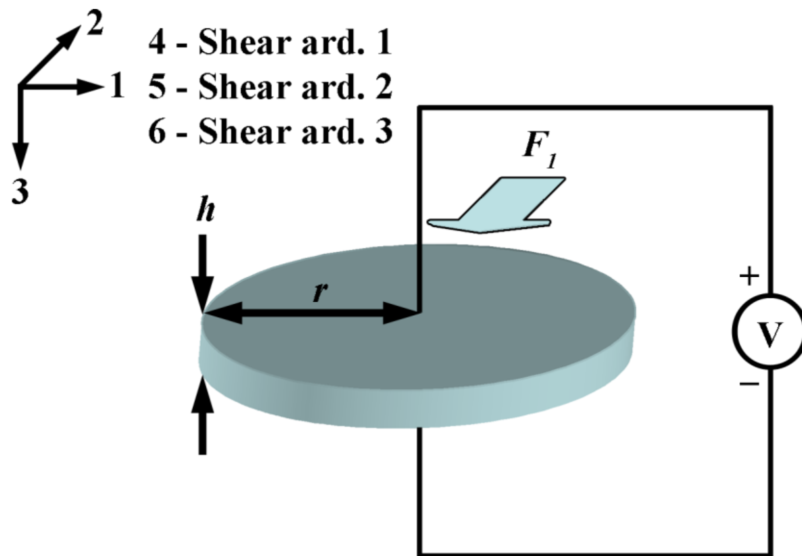

Fig. 3.3. A circular piezoelectric element with surface electrodes connected to a voltmeter. The axis convention is shown on the upper left.

The magnitude of the generated voltage change is dependent upon the material coefficients of the piezo material and governed by the piezoelectric constitutive equations. The key coefficients and electromechanical relations for sensing applications are discussed next.

3.3.2. Stress-to-voltage conversion

A direct numerical representation of a piezo material's electromechanical properties is provided by the piezoelectric strain constant d_{ij}. Consider the circular PZT element shown in Fig. 3.3. The axis convention is shown in the figure inset with directions 4, 5 and 6 denoting the shear around directions 1, 2 and 3 respectively. The element is poled along the 3-axis and connected to a voltmeter via surface electrodes. d_{ij} describes the ratio of short circuit charge per unit area collected in the *i*-direction in response to stress applied in the *j*-direction. As is the case for most piezoelectric ceramics, PZT is a transversely isotropic material and hence, its only non-zero piezoelectric strain constants are d_{31}, d_{33} and d_{15} [88]. Hence, the charge per unit area that is generated by

a PZT motion sensor in response to applied stress can be summarized in the following electrical displacement vector,

$$\begin{Bmatrix} D_1 \\ D_2 \\ D_3 \end{Bmatrix} = \begin{bmatrix} 0 & 0 & 0 & 0 & d_{15} & 0 \\ 0 & 0 & 0 & d_{15} & 0 & 0 \\ d_{31} & d_{31} & d_{33} & 0 & 0 & 0 \end{bmatrix} \begin{Bmatrix} \sigma_1 \\ \sigma_2 \\ \sigma_3 \\ \tau_{23} \\ \tau_{31} \\ \tau_{12} \end{Bmatrix} \tag{3.11}$$

where D_i is the total charge per unit area generated in the i-direction, σ_i denotes stress in the i-direction and τ_{ij} is the shear force on the i,j-plane.

Consider a phonon source that generates 1-D compressional waves propagating in the 3-direction, as is the case for a MEMS switch that displays out-of-plane motion upon actuation, located on the top surface (1,2-plane) of the PZT element. As the waves are transmitted across the source-element interface and into the peizo, a stress field $\sigma_{PZT,3}$ is set up in the element. From the electrical displacement vector (Equation (3.11)), the total charge per unit area generated is given by,

$$D_3 = d_{33}\sigma_{PZT,3} \tag{3.12}$$

Hence, the total charge q generated is,

$$q = \int_{A_3} d_{33}\sigma_{PZT,3}\, dA_3 = d_{33}\sigma_{PZT,3}\left(\pi r^2\right) \tag{3.13}$$

where r is the radius of the circular piezo element. The sensing voltage V_S generated is therefore,

$$V_S = \frac{q}{C_p} = \frac{d_{33}h}{\varepsilon_p}\sigma_{PZT,3} \tag{3.14}$$

where h is the thickness and ε_p is the dielectric constant (F m^{-1}) of the piezo element. C_p is the capacitance of the element, which can be determined from

$$C_p = \frac{\pi r^2 \varepsilon_p}{h} \tag{3.15}$$

Assuming loss-less transmission and no reflection across the source-element interface, the stress field σ_0 generated by switch actuation is maintained as it propagates into the piezo element. However, since Equation (3.14) predicts V_S based on the charge generated over the entire sensor surface, the generated stress σ_0 must be averaged over the sensor area $A_3 = \pi r^2$. Therefore,

$$\sigma_{PZT,3} = \overline{\sigma_0} = \frac{1}{\pi r^2} \int_{A_3} \sigma_0 \, dA_3 \tag{3.16}$$

Combining Equations (3.9) and (3.10),

$$V_S = \frac{d_{33} h}{\pi r^2 \varepsilon_p} \int_{A_3} \sigma_0 \, dA_3 \tag{3.17}$$

which gives the relationship between the stress produced during device actuation σ_0 and the sensing voltage V_S generated. Hence, the magnitude of the measured V_S provides a quantitative measure of the stress that is generated during switch actuation. Since the stress field σ_0 changes according to the contact condition during actuation, the fluctuations in V_S are also indicative of various mechanical phenomenon, such as bounce, which occurs during device operation.

For vibrating resonator structures, a similar derivation for the piezo voltage can be performed. In Section 3.2.2, a 1-D beam/anchor junction in a resonator was derived to be a wave source that, during in-plane vibration of the beam, injects transverse waves

into the anchor structure. Considering the junction as a radial source of transverse waves (neglecting the effects contributed by the evanescent waves), the waves propagating in the 3-direction (with displacement field u_2) will be picked up by the piezo element. The relevant stress field, in this case, is in the 2-direction. Therefore,

$$D_3 = d_{31}\sigma_{PZT,2} \tag{3.18}$$

where $\sigma_{PZT,2}$ denotes the stress in the PZT element generated in the 2-direction by the propagating transverse wave. The total charge q and sensing voltage V_P are hence,

$$q = \int_{A_3} d_{31}\sigma_{PZT,2}\ dA_3 = d_{31}E_{PZT}\pi\ r\int_r \delta_2\ dx_2 \tag{3.19}$$

$$V_P = \frac{d_{31}E_{PZT}h}{r\varepsilon_p}\int_r \delta_2\ dx_2 \tag{3.20}$$

where E_{PZT} is the Young's modulus of the piezo material and δ_2 is the strain generated in the piezo element by the transmitted transverse waves. Noting the relationship between the wave displacement and strain fields: $u = \int \delta\ dx$ and considering Equation (3.10), the relationship between V_P and the in-plane displacement of the vibrating beam (the bending wave displacement and beam displacement are synonymous) can be derived as,

$$V_P = \frac{d_{31}E_{PZT}h}{r\varepsilon_p}\frac{2}{\left(\sqrt{W/w}\right)^3}u(t) \tag{3.21}$$

Hence, the piezo voltage V_P is a direct representation of the in-plane displacement of the vibrating device. Since the transmitted waves from the vibration source (i.e. the resonator) are measured, the voltage amplitude is dependent on the dimensional characteristics of the device and is modulated by the ratio of W/w (which was derived earlier in Section 3.2.2).

The above voltage equations for contact-mode (Equation (3.17)) and non-contact mode (Equation (3.21)) MEMS structures are derived for the ideal conditions whereby no energy loss and no reflection occur as the elastic waves propagate across the structure/sensor boundaries. Hence, they tend to overestimate the generated voltages V_S and V_P. In the actual experimental setup, both these effects are present and contribute somewhat to reducing the amplitude of the piezo voltages. This reduction in signal can be tempered by simply amplifying the piezo voltage with electronics. More importantly, the frequency characteristics of the waves are actually maintained and these carry important information regarding the motion of the structure. The experimental setup for phonon detection will be described next, along with considerations for piezo selection and associated signal loss mechanisms.

3.4. Experimental setup

A setup for phonon detection can be easily realized with three basic components: a piezoelectric transducer, voltage amplification electronics and voltage detection instrumentation. Fig. 3.4 shows a schematic diagram of the phonon detector setup that has been implemented. The MEMS device-under-test (DUT), such as an electrostatic comb actuated resonator, is mounted on top of the piezo transducer which is positioned within a metallic housing. The housing provides a ground reference for the piezo voltage (V_S or V_P) and also shields the transducer form stray electric fields. Voltage amplification is provided by a two-stage preamplifier circuit with measured gain of ~200 and 3-dB bandwidth of 364 kHz. The amplified piezo voltage is then read by a digital storage oscilloscope, to provide the phonon waveform $V_{phonon}(t)$.

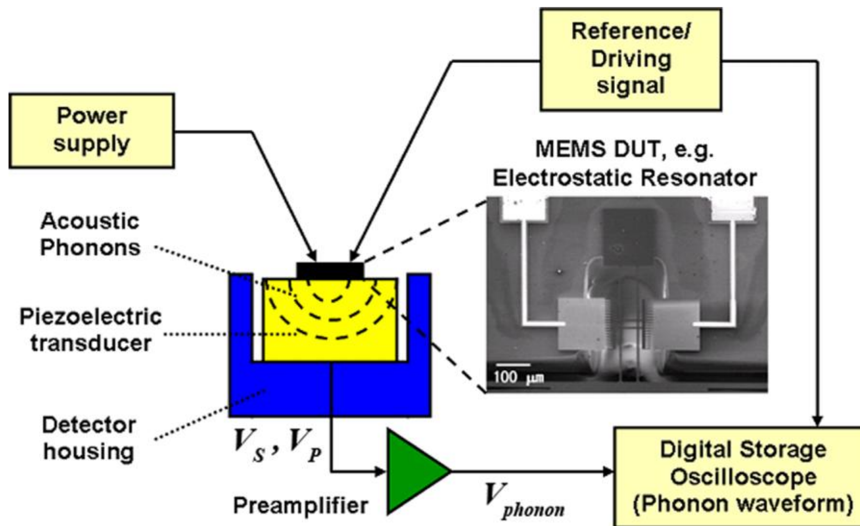

Fig. 3.4. Schematic of the phonon detection setup for MEMS devices.

Combining the phonon detector (consisting of the PZT transducer, the preamplifier circuitry and the digital oscilloscope) with various hardware components, an in-vacuum test system for MEMS device characterization was developed. A block diagram of the test system is presented in Fig. 3.5. The vacuum test system consists of the following major hardware components: a HP6634B DC power supply, a AFG3102 signal generator, the phonon detector, a Tektronix TDS5034B digital oscilloscope and the Hitachi Model S3500 SEM. The DC power supply and signal generator provide the electrical inputs necessary for device operation and the Tektronix digital oscilloscope provides a read-out of the phonon waveform $V_{phonon}(t)$. The transducer housing and preamplifer circuitry are housed inside the vacuum chamber of the S3500 SEM. Electrical contacts to the DUT and the detector are made via microprobes and flanges. The SEM chamber provides the vacuum environment (nominal base pressure 10^{-4} – 10^{-3} Pa) required by the test system. At the same time, the SEM also allows imaging of device movement. Hence, this test system provides the dual capability of phonon detection and in-situ measurement of device displacement.

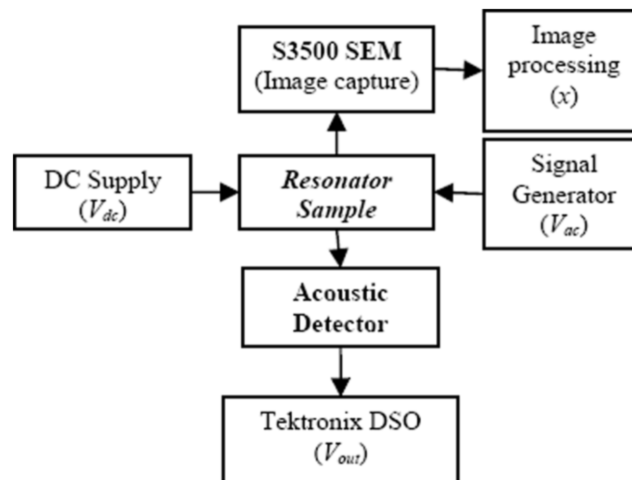

Fig. 3.5. Block diagram of the in-vacuum phonon detection test system for MEMS devices.

Automation of the in-vacuum test system was achieved using software developed with National Instruments' LabView 8.0. The automation software interfaces the HP6634B DC power supply, the AFG3102 signal generator as well as the Tektronix TDS5034B DSO with a main controlling computer (CPU). The instruments and the CPU communicate via the general-purpose interface bus (GPIB). Each instrument has a GPIB port to both send data and receive control instructions while the CPU is equipped with a GPIB card to receive data and send instructions. The automation software can be customized for device-specific characterization applications.

Two aspects of this detection system must be treated with considerable care in order to achieve the best motion detection sensitivity. The first is selection of the piezoelectric transducer and the second is the contact condition between device and transducer (which minimizes propagation loss and reflection at the device/transducer interface). Both of these will be discussed in the following sections.

3.4.1. Selection of piezoelectric transducer

Since the piezoelectric transducer is the component converting the waves representing device motion into a measurable voltage signal, selecting a material with the appropriate piezoelectric properties is of vital importance. Aside from the piezoelectric strain constant d_{ij} and the dielectric constant ε_p which determine the piezo voltage magnitude, another key characteristic to note is the operating bandwidth of the transducer, which is effectively the range of frequencies over which its piezoelectric properties are maintained. An appropriate sensor element should have a bandwidth that encompasses the frequencies of the phonons to be detected.

In this case, the frequencies of the clamped-clamped beam resonators which will be characterized in later experiments have operating frequencies which range from 100 kHz to 200 kHz and are hence expected to generate phonons in the same frequency range. The piezoelectric transducers which were procured for the phonon detection setup are made from the material APC840, which is a variant of the PZT ceramic, supplied by APC International, Ltd. The transducers are essentially discs of APC840 material sandwiched between circular metal electrodes. The dimensions, physical and piezoelectric properties of the transducer, obtained from the APC International online catalogue [89], are summarized in Table 3.1. The transducer operating bandwidth of 55 – 212 kHz is sufficient to cover the frequency range of the resonators that were characterized in later experiments. Considering also the preamplifier circuit with gain ~200 and 3-dB bandwidth of 364 kHz, the overall bandwidth of the phonon detector should be ~212 kHz, limited by the piezo transducer.

Table 3.1. Summary of dimensions, physical and piezoelectric properties of the transducers used in the phonon detection setup [89]. The transducers are made from APC840 material.

Property		**Value**
Piezoelectric strain constants, (C N^{-1})	d_{33}	2.90 x 10^{-10}
	d_{31}	1.25 x 10^{-10}
Dielectric constant, ε_p (F m^{-1})		1.11 x 10^{-8}
Radius, r (mm)		8
Thickness, h (mm)		1.43
Young's modulus, E_{PZT} (GPa)		80
Density, ρ (kg m^{-3})		7600
Resonance frequency, f_0 (kHz)		133
Operating bandwidth (kHz)		55 – 212

Using the specified properties in Table 3.1 and applying Equation (3.21), the voltage-displacement gain can be calculated to be $\frac{6.44\times10^{10}}{\left(\sqrt{W/w}\right)^3}$ V m^{-1} (inclusive of the electrical gain of 200). For a nominal device with dimensions W = 100 µm and w = 6 µm, a beam vibration with 1 nm peak amplitude would hence generate a voltage of ~946 mV. Of course, this voltage value is derived based on ideal conditions at the device/transducer interface, i.e. no transmission losses and reflection. In the practical system, both effects may actually reduce the voltage-displacement gain by a few orders of magnitude. These will be discussed in the following section.

From both the selection of the piezo transducer and the design of the supporting voltage amplification electronics, the test system has been optimized for motion sensing of low frequency devices. It is, in fact, possible to extend the technique to characterize higher frequency devices by selecting an appropriate piezo sensing element and redesigning the supporting amplification electronics. The main limiting factor to the testing bandwidth is the frequency characteristics of the piezoelectric sensor. Current commercially available transducers are still limited to relatively low

operating frequencies (<5 MHz) [88]. However, significant efforts have been directed toward the development of high frequency transducers in recent times. Piezoelectric transducers designed for medical ultrasonic imaging have already been shown to operate at frequencies ranging from 50 – 75 MHz [90] and it is likely that novel materials with even higher operating frequencies will emerge in the near future. Extending the frequency capabilities of phonon sensing by utilizing these state-of-the-art piezo materials is a distinct possibility.

3.4.2. Interface effects and phonon coupling between device and transducer

The two key factors influencing the motion detection sensitivity of the technique are reflection effects and transmission losses at the device/transducer interface. Reflection effects arise due to the mismatch in the acoustic impedances between the device (for an unpackaged device, this is usually silicon) and transducer (in this case, APC840) materials. The acoustic impedance Z of a material can be expressed as [91],

$$Z = \rho\alpha = \sqrt{\rho E} \tag{3.22}$$

where ρ is the density and E is the Young's modulus of the material and α is the wave velocity of the elastic waves propagating in the material.

Once the acoustic impedances are known, it is possible to calculate the reflection R and transmission U coefficients at the boundary [91],

$$R = \frac{(Z_2 - Z_1)^2}{(Z_2 + Z_1)^2} \tag{3.23a}$$

$$U = 1 - R \tag{3.23b}$$

where Z_1 and Z_2 are the acoustic impedances of the source and target materials respectively. The reflection coefficient R is an indication of the fraction of incident acoustic energy that is reflected at the boundary due to the difference in the physical properties of the two materials. As long as $Z_2 \neq Z_1$, $R > 0$ and $U < 1$.

Transmission losses are the result of poor phonon coupling between device and transducer. Some common causes of this include improper sample mounting causing air gaps between device and transducer, poor sample adhesion to the transducer surface and presence of foreign particles at the device/transducer interface. Some strategies to improve the contact condition between device and transducer, alleviating transmission losses, are discussed in Section 3.5.3. The effects of transmission losses are significantly harder to quantify theoretically and are perhaps best represented by a coupling factor κ ($0 < \kappa < 1$) which should be experimentally measured from sample to sample. The higher the coupling factor, the better the transmission properties and lesser the transmission losses at the interface.

Hence, including the effects of interface reflection and transmission losses, the voltage-displacement relationship (Equation (3.21)) for characterizing resonator devices is modified to be,

$$V_P = \frac{d_{31} E_{PZT} h}{r \varepsilon_p} \frac{2\kappa U}{\left(\sqrt{W/w}\right)^3} u(t) \tag{3.24}$$

In summary, the necessary hardware components for the in-vacuum phonon detection test setup have been described. The selection of an appropriate piezo sensing element is of key importance as it determines the operating bandwidth of the test system. As

the resonator structures to be characterized in future experiments operate at frequencies ranging from 100 – 200 kHz, the test setup has been optimized to have a bandwidth of ~212 kHz. Interface reflection and transmission losses have also been identified as the two main factors affecting detection sensitivity. In the following section, some proof-of-concept experiments that were carried out on clamped-clamped beam resonators and MEMS switches to verify the phonon voltages they generate during actuation will be presented.

3.5. Proof-of-concept experiments on MEMS switches and resonators

Having established the hardware for the in-vacuum phonon detection system, a simple set of tests were carried out on contact and vibrating MEMS structures as a proof-of-concept for motion detection. The devices utilized were MEMS switches and electrostatic actuated clamped-clamped beam resonators. Several techniques for improving the phonon coupling between device and transducer and reducing transmission losses were investigated and these results will be discussed. Calibration tests were also performed to determine the voltage-displacement transfer function for resonator devices since this relation is required for monitoring displacement drift in later experiments on resonator long-term stability.

3.5.1. Phonon waveforms generated by switches and resonators

Phonon characterization of MEMS switches

The contact-mode device selected for the experiment is the DowKey Microwave M1C06-CDK2 magnetically-latched SPDT RF MEMS switch. An optical image of the

device is shown in Fig. 3.6 along with a schematic diagram representing the electrical connections. The switch utilizes low-power magnetic actuation to shift the position of a short-travel cantilever between open and closed states to effect latched switching. Both the switch cantilever and contact pads are made of gold.

To characterize the motion the switch exhibits during actuation, a specimen of the packaged device is first mounted onto the piezo transducer in the test system (as shown in Fig. 3.4) using silver paste as an adhesive. The paste also acts as a medium through which the phonons generated during actuation are coupled to the transducer sensor. The switch is operated to change state at 1 kHz by supplying a periodic square wave of the same frequency at the X1-X2 contacts. During switching, the cantilever contacts the J2 electrode first followed by the J3 electrode as it alternates between the on and off states. Hence, an observation of two distinct phonon waveforms representing the two contact events is expected.

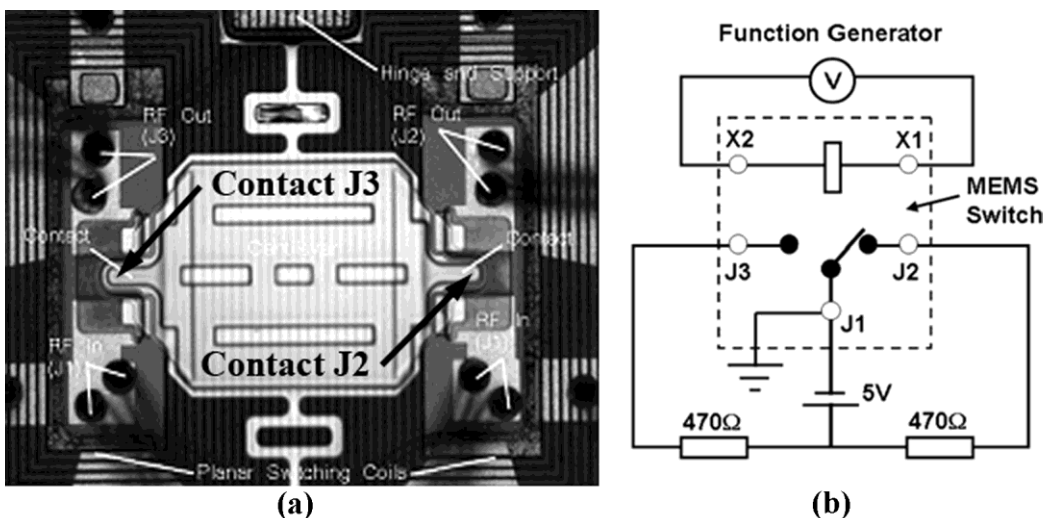

Fig. 3.6. (a) Optical image of the MEMS switch and (b) electrical schematic diagram.

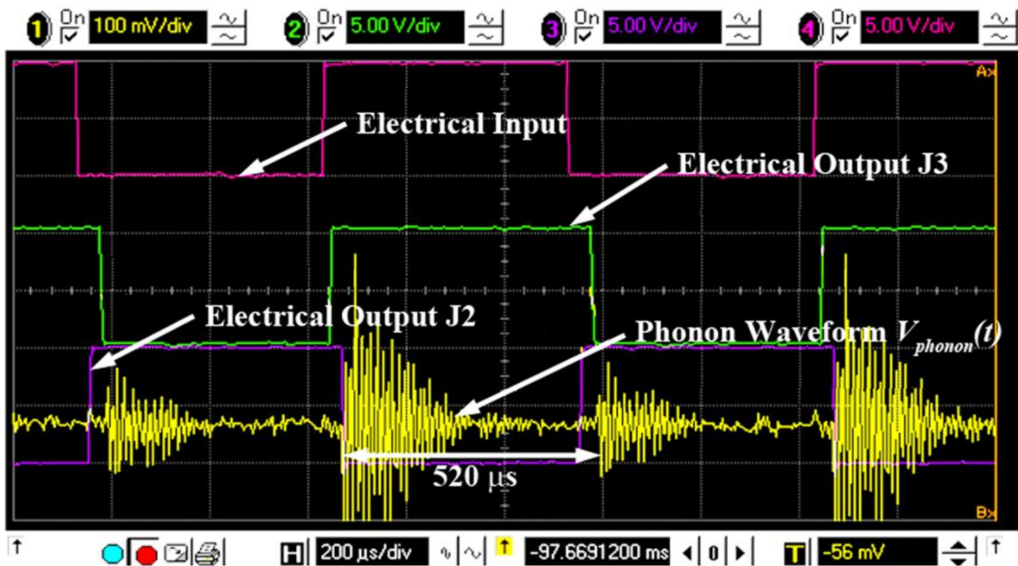

Fig 3.7. Screenshot of voltage measurements recorded by the oscilloscope during ~2 cycles of switch operation.

A screenshot of the voltage measurements recorded by the oscilloscope during ~2 cycles of switch operation is shown in Fig. 3.7. The waveforms displayed include the 1 kHz square wave electrical input (10 V_{pp} magnitude), the corresponding 5 V switch electrical outputs at J2 and J3 and the phonon waveforms generated during the contact events. The phonon waveforms $V_{phonon}(t)$ can be analyzed as follows. From the screenshot, it can observed that there are indeed two different $V_{phonon}(t)$ recorded during the operating cycle, one with larger peak-to-peak amplitude of ~180 mV_{pp} resultant from contact at J3 and the other ~100 mV_{pp} waveform from contact at J2. At first glance, the most obvious implication of the two waveforms is that a greater amount of stress is generated on the electrode during contact at J3 (i.e. the cantilever is hitting the electrode harder at J3). A possible ill-effect of this larger stress is increased mechanical degradation of the cantilever/J3 electrode during long term operation. Since V_{phonon} is representative of the stress which is present at the point of contact (as predicted by Equation (3.17)), the entire waveform is hence an indication of the change in the stress during and after the switching event.

It is apparent from the phonon waveforms that the cantilever does not immediately settle to a steady state when contact occurs, but persists in a state of under-damped vibration for some time. However, the amplitude of this vibration is not sufficient to break the electrical contact as evidenced by the electrical outputs. The time it takes for the transient vibration to dissipate, this time is labeled as the settling time t_S, is also different for each switching event and the measured t_S during J3 and J2 contact are 264 μs and 212 μs respectively. The shape of the phonon waveforms and hence t_S is expected to vary over the operating life of the switch as the contact surfaces suffer from mechanical degradation and wear. A good means by which this change in waveform shape can be monitored is through performing frequency analysis on the waveform itself. This is achieved by applying Fast Fourier Transform (FFT) to obtain the frequency components and a significant disparity in the intensity of one or more components would indicate a variation in the time-domain waveform.

To summarize, Table 3.2 provides a comparison of the quantitative data that can be obtained during switch testing from the switch electrical output and from the phonon waveform (see Fig. 3.7 for both waveforms). It is apparent that conventional electrical testing can only provide information on very basic switch operation parameters. Phonon detection, on the other hand, is able to offer a more comprehensive mechanical perspective to complement the parameters obtained from electrical testing. For example, both the stress amplitude (which gives the actuation force) and cantilever settling time t_S are properties representative of the mechanical state of the switch which cannot be quantified by simply observing the electrical outputs alone.

Table 3.2. Comparison of switch performance parameters that can be obtained by electrical testing and by phonon detection. ✗ denotes parameter is not quantifiable by the technique.

	Electrical parameters			**Mechanical parameters**			
	Rise time (μs)	Fall time (μs)	Open/ Close	Force (mN)	Settling time (μs)	Surface properties	Energy dissipation
Electrical testing	5	8	✓	✗	✗	✗	✗
Phonon detection	✗	✗	✓	0.269 (J2) 0.484 (J3)	212 (J2) 264 (J3)	✓	✓

Although examining the electrical outputs is sufficient to provide short-term performance parameters, such as rise time, fall time and switching delay, studying the mechanical state can offer a more long-term performance assessment of the device since these mechanical characteristics will invariably change with the tribological properties of the contact surfaces over many cycles of actuation. Hence, the phonon detection technique can provide a good body of information to switch designers to complement the performance parameters that can be obtained via electrical testing.

Phonon characterization of micromechanical resonators

A second proof-of-concept experiment was carried out on a non-contact mode device. The aim was to sense the vibration motion of a micromechanical electrostatic actuated clamped-clamped beam resonator. An SEM image of the device is shown in Fig. 3.8. When actuated by a DC bias V_B and an AC drive input v_d at its fundamental resonance frequency f_0, the resonator produces simple sinusoidal in-plane motion. Since the device is designed to operate in its fundamental mode, the peak displacement occurs at the mid-point of the clamped-clamped beam.

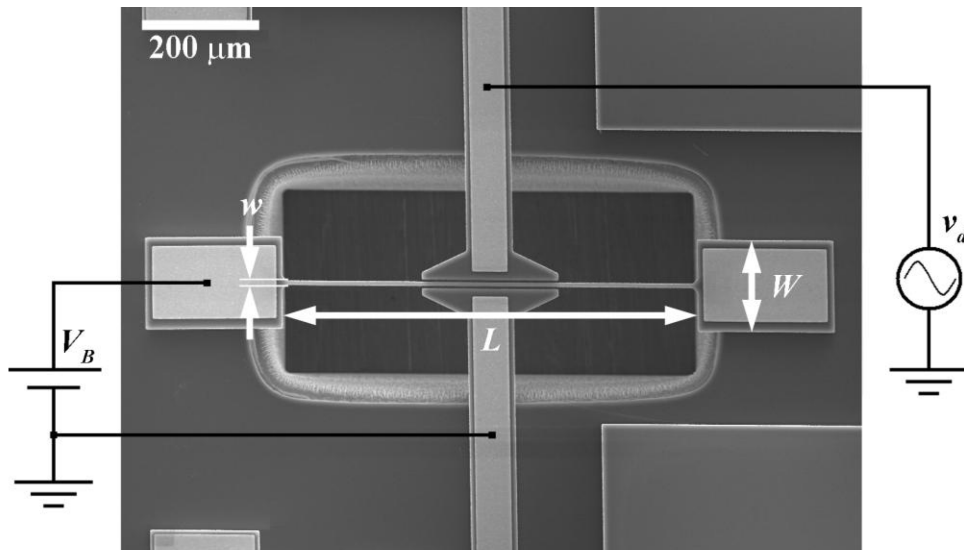

Fig. 3.8. SEM image of the clamped-clamped beam resonator. For this particular device design L = 480 µm and w = 6 µm, therefore the theoretical resonance frequency f_0 = 200 kHz. The anchor width W = 100 µm.

The peak-to-peak vibration amplitude *u(t)* of the beam is less than 0.5 µm when operating in linear mode and therefore its motion cannot be detected using optical imaging techniques. However, a physical verification of the resonator motion is required, in the form of a direct measurement of its motion amplitude, for comparison with the generated phonon waveform. Hence, a stroboscopic scanning electron microscopy (SEM) technique was developed to provide the required nanoscale resolution for measuring resonator dynamic motion. A detailed description of this technique will be provided in Chapter 4.

The resonator was mounted onto the piezo transducer using silver paste in the same manner as the switch (described earlier). However, the device is not packaged and hence the phonon transmission occurs directly from the silicon substrate to the transducer. The device was actuated to operate in its linear region with V_B = 10 V and v_d = 25 mV and in a vacuum ambient of pressure ~10^{-3} Pa.

The resultant phonon waveform $V_{phonon}(t)$ generated by the device at resonance is shown on the oscilloscope screenshot in Fig. 3.9(a). To visualize the actual physical motion of the resonator, a phase-resolved stroboscopic SEM image of its vibration was simultaneously taken and the resulting micrograph is shown in Fig. 3.9(b). Fig 3.9(b) suggests that the motion of the clamped-clamped beams is sinusoidal in nature with peak-to-peak amplitude u = 112 nm which corresponds well with the observed sinusoidal phonon waveform with V_{phonon} ~ 230 mV_{pp}. This indicates that the physical motion of the device is directly represented by its phonon waveform. The measured peak-to-peak vibration amplitude u is related to the recorded phonon voltage V_{phonon} by Equation (3.24). Subsequent calibration experiments, presented in Section 3.5.2, confirm that V_{phonon}, in fact, increases/decreases linearly with u. The phonon waveform also indicates that the resonator vibration has a phase lag of 54° with respect to the actuation voltage, and this is in good agreement with the displacement measurements (i.e. both methods detect the same device phase shift).

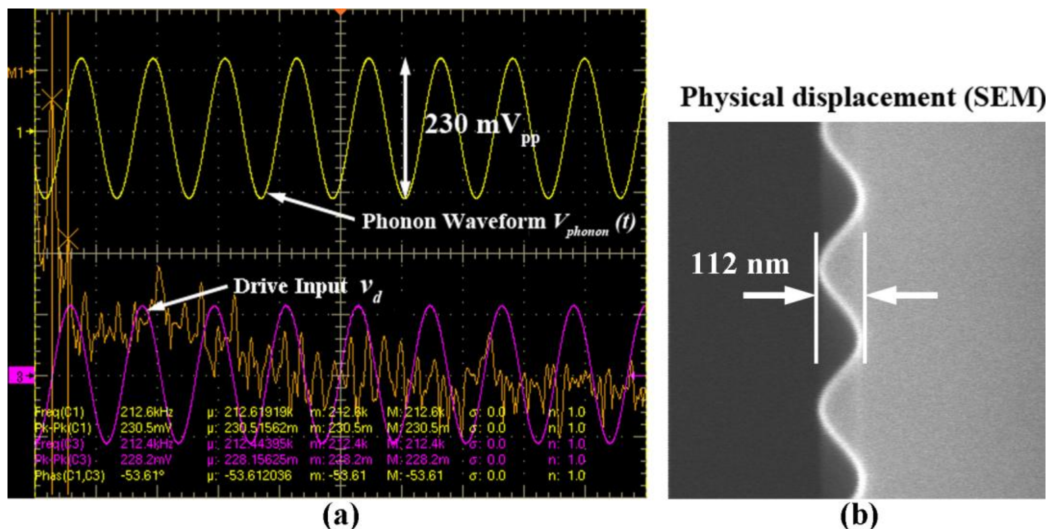

Fig. 3.9. (a) Phonon waveform $V_{phonon}(t)$ generated by the resonator device actuated with DC bias V_B = 10 V and AC drive input v_d = 25 mV in a vacuum ambient (pressure ~10^{-3} Pa). The peak-to-peak voltage of the phonon waveform is 230 mV_{pp}. (b) Corresponding sinusoidal physical displacement of the device observed with stroboscopic SEM. The measured peak-to-peak displacement is 112 nm.

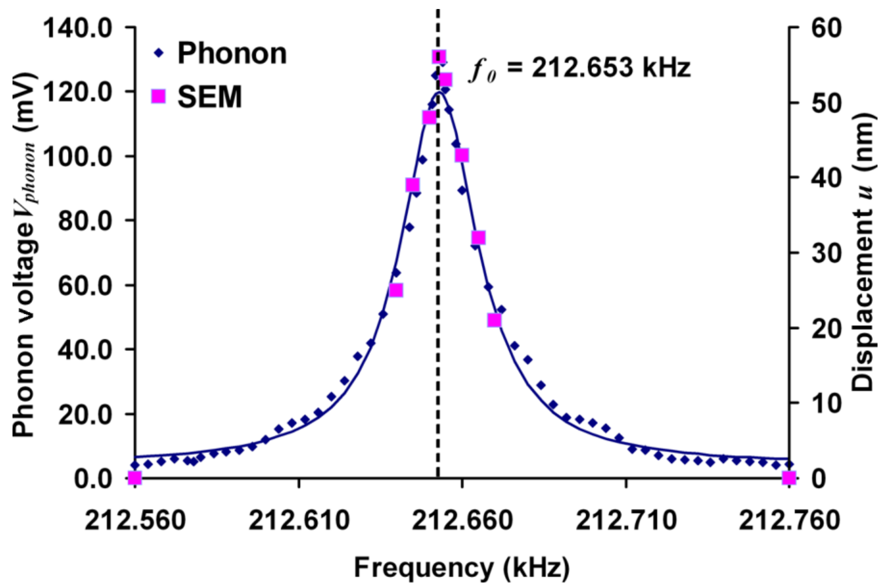

Fig. 3.10. Frequency response of the resonator, actuated with DC bias V_B = 10 V and AC drive input v_d = 25 mV, obtained using phonon detection and stroboscopic SEM (displacement measurements). Both techniques predict the same resonance frequency f_0 = 212.653 kHz and Q-factor ~ 10,600 for the device.

The phonon detection test system can be further utilized to obtain the frequency response of the resonator. This is accomplished by performing a frequency sweep around the resonance frequency f_0 of the device and recording the peak-to-peak voltages of the phonon waveform at each frequency point. As the process only involves measurement and recording of voltages, very high throughput can be achieved, limited only by the rate of the frequency sweep and the sampling rate of the oscilloscope. A similar characterization can be carried out using stroboscopic SEM, albeit at the expense of measurement efficiency since the high resolution imaging requires a significantly longer time. To provide a basis for comparison for phonon detection, the device frequency response was obtained using both techniques and the resulting response curves are presented in Fig. 3.10. The response curves in Fig. 3.10 show that both techniques predict the same resonance frequency (212.653 kHz) and Q-factor (10,600) for the device, with both curves displaying an almost exact same shape. As direct physical measurement of resonator amplitude are considered as the gold

standard for motion detection, this excellent agreement in the frequency response data further establishes the reliability of phonon detection for dynamic motion sensing of non-contact mode MEMS devices.

Having established that phonon detection can accurately measure the short-term operating parameters of the resonator, such as resonance frequency and *Q*-factor, its potential in evaluating the long-term performance of the device will be highlighted at this point. Over long-term operation, it is reasonable to expect deterioration in the mechanical state of the resonator that could manifest itself in a variety of ways. Crack initiation and propagation is a possibility (see Section 2.6.3). Considering that the clamped beam regions near the anchors experience the greatest stress during bending, if cracks were to occur, they would likely begin at or near the anchors. A weakening of the beam near the anchor would no doubt alter the anchor's phonon dissipation properties and hence keeping track of the phonon voltage would actually be a useful method for monitoring the health of the device. This concept is utilized in later experiments on the long-term frequency stability of resonators. While electrical measurements (see Section 2.5) can similarly provide information on resonator f_0 and *Q*-factor, they lack the ability of monitoring the mechanical state of the device, a capability that can be provided by phonon detection.

Table 3.3 provides a comparison of state-of-the-art resonator characterization techniques with phonon detection. The sensitivities and measurement capabilities listed are based on hardware setups that have been published in literature. It is first worth noting that phonon detection is able to measure the same device functional parameters (f_0 and *Q*-factor) as current techniques while achieving the high

measurement throughput of electrical methods (network analyzer). In terms of sensitivity, phonon detection is able to provide nanometer resolution, as evidenced by the proof-of-concept experiment in which the peak vibration amplitude of the resonator tested was <50 nm. This is comparable to high sensitivity techniques such as SEM and the network analyzer. In addition, imaging methods, such as optical microscopy and SEM, are not feasible for long-term testing due to their poor measurement throughput and electrical methods can only provide information on resonator frequency drift over time. It is doubtful that any of these current test methodologies will be able to identify long-term fatigue or failure modes since the measured parameters (displacement and capacitive currents) in no way reflect device mechanical state. Phonon detection, on the other hand, has immense potential for resonator long-term testing since it is able to keep track of the mechanical state of the device in terms of its anchor dissipation properties. It is this property that is likely to change during long-term operation.

Table 3.3. Comparison of state-of-the-art micromechanical resonator characterization techniques with phonon detection.

	Sensitivity	**Throughput**	**Measured parameter**	**Functional testing**	**Long-term testing**
Optical microscopy (Serio et al. [28])	~0.5 µm	Poor	Displacement	f_0, Q-factor	Not feasible
SEM (Roy et al. [35])	~2 nm	Poor	Displacement	f_0, Q-factor	Not feasible
Network analyzer (Bruschi et al. [44])	< 10 nm	High	Capacitive-induced current	f_0, Q-factor	Yes, freq. performance only
Phonon detection	nm range	High	Mechanical energy dissipation	f_0, Q-factor	Yes, freq. performance & fatigue

To summarize, the proof-of-concept experiments show that the motion of the two contact mode and non-contact mode MEMS device samples that were used generate measurable phonon waveforms that are representative of their respective mechanical motion. In both instances, the phonon waveforms are able to provide similar information on the short-term performance parameters of the devices as more established electrical characterization techniques. In addition, phonon detection also offers additional insight into the mechanical state of the devices, supplying data that can be used to assess their long-term performance. In the following section, a method for calibrating the motion measurement capability of the phonon detection test setup is presented since voltage-to-displacement conversion is required in later experiments on resonators.

3.5.2. Voltage-displacement calibration and experimental determination of coupling factor *κ*

Calibrating the phonon detection setup is fairly straightforward, although it requires high resolution imaging of dynamic motion. The procedure heavily involves another technique developed in this work: the stroboscopic SEM. The process is demonstrated on the mounted resonator device that was used in the proof-of-concept experiments described in the previous section. The mounted sample was actuated to operate in its linear mode and its motion was simultaneously measured using phonon detection and stroboscopic SEM. The phonon voltage and physical displacements were recorded at several frequency points at and around its resonance frequency f_0 = 212.653 kHz. This was repeated for two other bias conditions within the linear operating regime of the resonator. The voltage-displacement relation can be represented by,

$$V_{phonon}(t) = Ku^n(t) \tag{3.25}$$

ln $V_{phonon}(t)$ against ln $u(t)$ is plotted for each drive condition as shown in Fig. 3.11. From the best-fit curve through all three sets of points a value of n ~ 1 is obtained, indicating a linear first-order relationship between $V_{phonon}(t)$ and $u(t)$. Therefore, the relation can be simplified to,

$$V_{phonon}(t) = Ku(t) \tag{3.26}$$

The voltage-displacement gain K can then be obtained by plotting the recorded voltage against measured displacement at all the frequency points and finding the slope of the best-fit curve through the points. The voltage-displacement plots for the sample at all three operating biases are shown in Fig. 3.12 and from the best-fit curve through the points, the average K is determined to be 2.246 mV nm^{-1} (or 2.264×10^6 V m^{-1}).

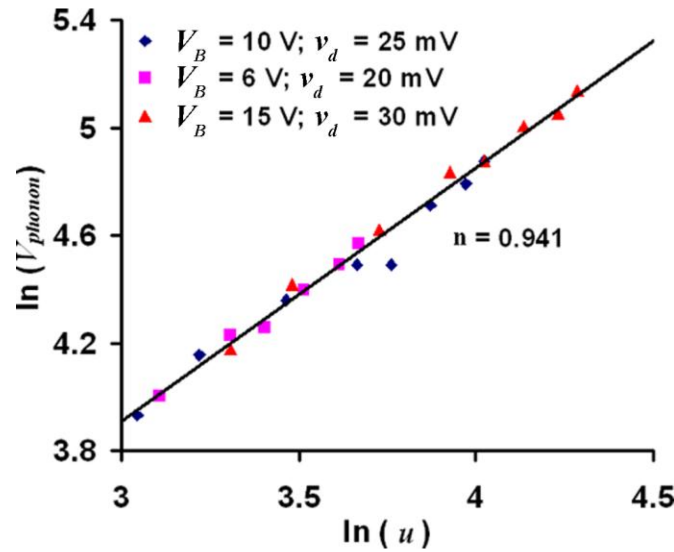

Fig. 3.11. ln (V_{phonon}) vs. ln (u) at various linear drive conditions. From the slope of the best-fit line though all the points, n ~ 1.0 indicating a linear first-order relationship between the two parameters.

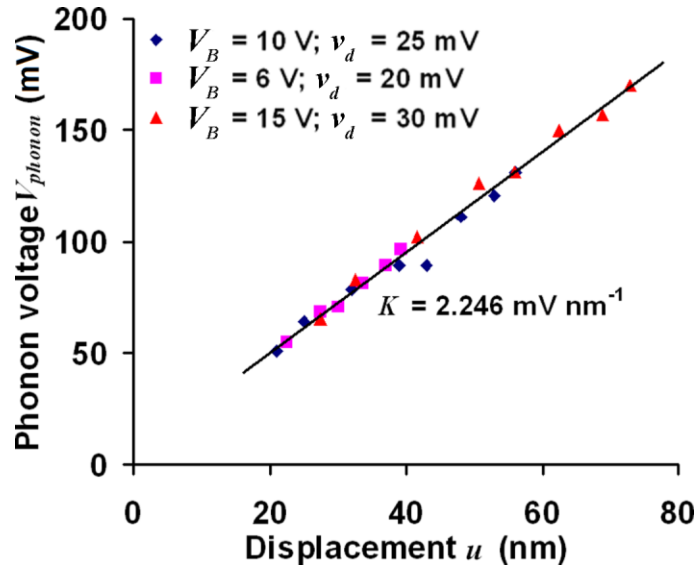

Fig. 3.12. Phonon voltage vs. displacement plots for the sample at the three linear operating biases. From the best-fit line through all three sets of points, the average K is determined to be 2.246 mV nm^{-1}.

Considering Equation (3.24) and the physical and dimensional characteristics of the resonator and piezo transducer, this measured value of K can be used to determine the coupling factor κ of this particular device. Hence,

$$\kappa = \frac{r\varepsilon_p}{d_{31}E_{PZT}h}\frac{K}{2GU}\left(\sqrt{W/w}\right)^3 \tag{3.27}$$

where G = 200 is the electrical gain of the test setup. For the device in question, the relevant dimensions are W = 100 μm and w = 6 μm, and since it is directly mounted onto the transducer, U = 0.985. Applying Equation (3.27) κ is calculated to be 0.00243. The small coupling factor suggests that the transmission losses across the sample-transducer interface are substantial, owing largely to the contact condition between the two surfaces. To enhance the motion sensitivity of the technique, it is necessary to investigate approaches for enhancing the phonon coupling between sample and transducer. Some of the methods that have been explored, and their respective effectiveness, are presented in the next section.

3.5.3. Sample mounting for improved phonon coupling

The approaches that have been tested revolve around the concept of maximizing the contact surface area between sample and transducer to improve phonon coupling. A direct mating of the sample and transducer surfaces usually suffers from issues such as uneven mounting which introduces air gaps at the contact interface, presence of foreign particles and poor sample adhesion, all of which reduce the contact surface area between the two entities. A direct way of circumventing these issues would be to introduce a thin layer of filler material in-between the two surfaces so as to lessen the air gaps and increase the contact area. Some of the materials experimented with include acoustic friendly Braycote oil, thermal conductive tape, carbon paint and silver paste. All four materials are good thermal conductors which, by default, also make them good conductors of phonon energy.

To assess their effectiveness, the voltage-displacement gain K was determined while using each of the four materials to mount a resonator sample (the same device was used in the four K measurements) onto the piezo transducer. In each case, a thin layer of each material was applied onto the bottom surface of the sample die. The control case is a filler-free mount with only silver paste applied to the die corners as an adhesive to anchor the sample onto the transducer. The coupling factor κ was then calculated from the measured K values using Equation (3.27). The data obtained is summarized in Table 3.4.

Table 3.4. Measured phonon coupling factor improvement provided by applying various filler materials in between sample and piezo sensor.

Material	**Measured *K* (V m^{-1})**	**Coupling factor *κ***	**% improvement**
No filler (control)	2.264×10^6	0.00243	–
Braycote oil	9.410×10^6	0.0101	315.6
Thermal tape	5.031×10^6	0.00540	122.3
Carbon paste	3.857×10^6	0.00414	70.2
Silver paste	7.938×10^6	0.00852	250.7

From the collected data, it appears that Braycote oil is the most effective filler material, providing about 4X improvement to the gain K when applied. This is likely due to the fact that it is a liquid, making it more effective at plugging air gaps. In addition, the oil is vacuum friendly, making it well-suited to be used in the in-vacuum phonon detection test setup. The other materials all provide some degree of coupling enhancement and may be utilized in situations when Braycote oil is deemed unsuitable.

Hence, applying a suitable filler material at the device-transducer interface can significantly improve the phonon coupling and boost its transmission properties. This serves to enhance the overall signal-to-noise ratio (SNR) of the detection system and consequently its motion detection sensitivity.

3.6. Conclusions

In this chapter, a phonon detection technique for sensing the dynamic motion of MEMS devices was presented. Motion detection is achieved by utilizing a piezoelectric transducer to sense the mechanical waves or phonons generated during surface interaction or energy dissipation which occurs during device actuation. Proof-of-concept experiments carried out on MEMS switches and resonators show that

phonon detection is able to provide similar information on the short-term performance parameters of the devices as more established electrical characterization techniques. In addition, the technique also offers additional insight into the mechanical state of the devices, supplying data that can be used to assess their long-term performance. Although the test setup has currently been optimized for motion characterization of low frequency devices, the detection concept can be extended to higher frequency sensing by utilizing more advanced piezo materials and supporting electronics. Motion detection calibration of the test setup for resonator characterization was discussed and it was found that the setup is capable of sensing the nanoscale (~100 nm) linear vibration of resonators. Some considerations for enhancing detection sensitivity were also presented. In the next chapter, a high-resolution stroboscopic SEM technique developed for directly measuring the in-plane physical displacement of dynamic MEMS devices with nanoscale accuracy is introduced. The technique was applied extensively in subsequent calibration tests to compliment phonon detection.

CHAPTER 4

STROBOSCOPIC SCANNING ELECTRON MICROSCOPY FOR NANO-SCALE IN-PLANE MOTION MEASUREMENT

4.1. Introduction

Most MEMS devices exhibit motion or vibration upon actuation and hence, in order to characterize and evaluate device performance, it is necessary to be able to detect and measure their momentary displacement. State-of-the-art MEMS structures are already exhibiting motion amplitudes in the nano regime and it is likely that their displacements will continue to scale downwards with their physical dimensions. Laser and optical measurement methods have proven to be popular motion detection techniques because of their good performance, low cost and operational simplicity (refer to Sections 2.2 and 2.3). Although some of these optical techniques have nanometer spatial resolution when determining structure displacement [22], the displacement readings are based on image sequence processing by optical flow techniques, such as gradient methods, rather than actual physical measurements. Hence,

on top of possible aberrations already present in the imaging system, errors in the mathematical algorithms applied during image processing will contribute to larger measurement inaccuracies. It is fundamentally impossible for an optical microscope to resolve microstructure motion in the nanometer regime in far-field imaging due to visible light diffraction limits (~0.5 µm).

A possible solution to this limitation is to utilize an imaging technology that can achieve the required nano-scale resolution. The scanning electron microscope (SEM) is a well-established option for high resolution imaging down to about 2 nm. However, SEM is conventionally used for imaging static samples and not dynamic behaviour such as motion in MEMS devices. SEM stroboscopy, on the other hand, allows direct imaging and measurement of physical microstructure displacement with nanometer resolution [92]. The concept of stroboscopic SEM has already been demonstrated in IC testing [93] and magnetic domain analysis [94]–[95] and will be extended to micromechanical motion measurement in this work. This chapter presents the development of a stroboscopic imaging system for phase-resolved motion freezing and displacement tracking as well as time-resolved velocity estimation of micromechanical electrostatic comb actuated resonators. Using the implemented hardware, it is possible to obtain a full profile of the resonator's displacement over one or several cycles of its motion as well as a fairly accurate estimate of the resonator's instantaneous velocity at various phases of its motion. The stroboscopic SEM imaging system is heavily utilized for calibration of the phonon detection setup in subsequent experiments.

4.2. Principle of stroboscopic imaging using SEM

There are two typical methods to realize stroboscopy in the SEM. The first is to blank the primary electron beam as it scans the sample surface [93]. The second is to gate the secondary electron (SE) signal [94]–[95], which has the advantages of simpler implementation and does not degrade the electron-optical performance (unlike primary beam blanking). Continuous chopping of the electron beam in primary beam blanking reduces the signal-to-noise ratio (SNR) of the SEM. It also introduces beam jitter and beam motion at the target plane [96] and both these effects are detrimental to the primary beam's resolution and imaging capabilities. Gating the SE signal circumvents the above-mentioned issues since stroboscopy is realized under continuous illumination of the primary beam. Hence, the stroboscopic SEM imaging system is built around the concept of SE signal gating which is described in this section.

In typical SEM imaging, the primary electron beam is scanned in a raster pattern over the sample surface. The secondary electrons generated by the primary electron beam are detected by an SE detector, usually a scintillator-photomultiplier Everhart-Thornley Detector (ETD) [97], and the resulting analogue image signal is rendered into a gray level intensity distribution that is viewed as a two-dimensional image. For a digitally-controlled SEM, the pixel dwell time t_{pixel} of the raster scan can be defined as

$$t_{pixel} = \frac{t_{scan}}{N} \tag{4.1}$$

where t_{scan} is the frame scan time and N is the total number of pixels in the frame.

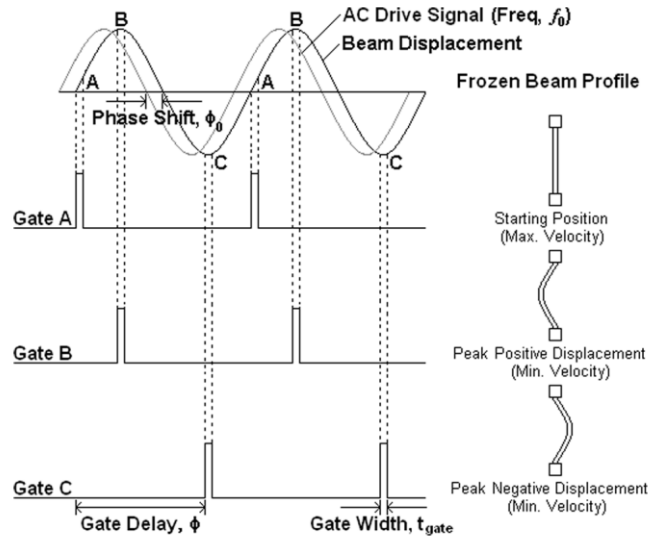

Fig. 4.1. Schematic diagram of time-gated signal detection for stroboscopic imaging.

Hence, the lateral scan rate of the SEM is,

$$v_{scan} = \frac{d_{pixel}}{t_{pixel}} \quad (4.2)$$

where d_{pixel} is the spatial resolution per pixel which is dependent on the magnification setting of the SEM.

During conventional SEM imaging of an actuating MEMS device, the device features will show up blurred in the final capture due to lack of synchronization between the primary electron beam and MEMS device movement (e.g. see Fig. 4.4(f)). It is possible to observe the actual position of the structure at a specific point in time by taking a time-gated sample of the SEM SE signal at a specific phase of the structure's motion. The principle of time-gated sensing is illustrated in Fig. 4.1. Consider the simple case of a resonant microstructure actuated by an AC sine input with frequency f_0. The expected change in displacement of the structure's moving parts would follow the periodicity of the AC drive waveform. If the SE signal is synchronously acquired at a constant gate delay ϕ of every cycle of the drive voltage with a sufficiently narrow

gate width t_{gate}, a stationary image of the vibrating sample can be obtained as the electron beam scans the sample. By varying ϕ, a plurality of stroboscopic images of the sample at various phases of its motion can be obtained.

In order to effectively freeze structure motion during the stroboscopic image capture, a crucial consideration is the choice of an appropriate value of t_{gate} determined by the peak in-plane velocity of the moving structure. The threshold gate width is given by

$$t_0 = \left(\frac{v_{scan}}{v_{\max}} \right) t_{pixel} = \frac{d_{pixel}}{v_{\max}} \tag{4.3}$$

where v_{max} is the peak velocity of the structure. A frozen image of the moving structure is obtained only when a gate width below t_0 is applied. From Equation (4.3), it can be seen that for a given SEM scan rate, a smaller gate width is required to freeze the motion as the peak velocity of the structure increases. For example, a 160 kHz comb actuated resonator with v_{max} = 0.24 m s^{-1} at spatial resolution d_{pixel} = 24 nm pixel^{-1} would require t_{gate} of 100 ns or below to freeze its motion.

Having established the necessary timing and signal gating requirements for motion freezing and stroboscopic imaging, the practical implementation of the stroboscopic SEM system will now be presented. The required instrumentation is described in the next section.

4.3. Experimental setup

The stroboscopic imaging system is presented in Fig. 4.2. The main system components include a Hitachi S-3500N SEM, a PC-controlled SEM scanning and

signal digitizer system (SEMICAPS 2000), a Tektronix AFG3102 signal generator and a Stanford Research System SR250 gated-integrator/boxcar averager. The SEM chamber has a nominal base pressure of $10^{-4} – 10^{-3}$ Pa.

During SEM imaging, a 512 × 512 pixel scan with 4096 sample averaging takes approximately 150 s, yielding a pixel dwell time t_{pixel} = 572 µs. At a magnification of 10,000X, the digital SEM image has a resolution of 24 nm per pixel. Therefore, at these settings, v_{scan} is 41.9 µm s^{-1}. t_{pixel} can be varied by changing the frame resolution (from 256 × 256 to 2048 × 2048) as well as the sample averaging (1 – 4096X). The analogue SE signal is fed into the gated-integrator/boxcar averager. The boxcar amplifies and integrates the image signal during the set gate width, samples it and holds the result till the next gate trigger. The boxcar is triggered by an external pulse which is synchronized with the MEMS device AC drive. By adjusting the relative phase delay ϕ of the boxcar gate trigger pulse, it is possible to selectively freeze the MEMS device at various phases of its motion down to about 2 ns (or 0.115° for a MEMS device vibrating at 160 kHz), limited by the minimum gate delay of the gated-integrator/boxcar averager. The averaged boxcar analogue output signal is subsequently digitized by the SEMICAPS system for image display and storage. Charge build-up on the devices due to electron bombardment during imaging is minimal as most MEMS devices are fabricated from polysilicon, which is a conducting material with a good charge sink path to ground.

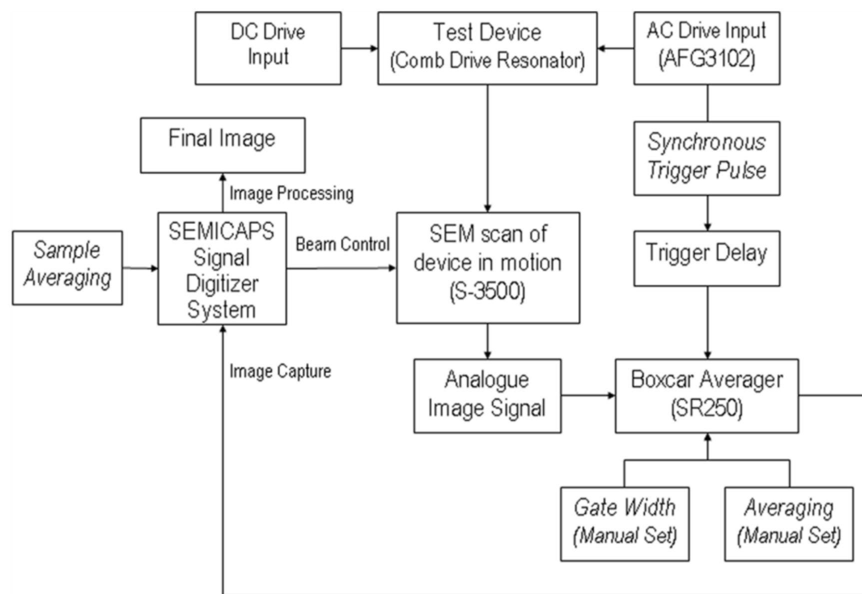

Fig. 4.2. Block diagram of the stroboscopic imaging system.

In the following section, the test setup is demonstrated on a micromechanical resonator. The stroboscopic system is not only able to measure dynamic motion parameters such as peak displacement, phase and velocity, it is also capable of obtaining a quantitative time-domain displacement plot which is particularly useful if a study of the device motion is required.

4.4. Stroboscopic imaging for measuring in-plane motion of micromechanical resonators

To evaluate the capabilities of the stroboscopic imaging system, a set of experiments to characterize the motion of a micromechanical comb actuated clamped-clamped beam resonator was carried out. The resonator, when actuated by a sinusoidal AC drive voltage v_d under linear (small-signal) drive conditions, produces simple sinusoidal vibrational motion in the plane of the substrate [98]–[99]. This vibration occurs in the fundamental mode and its amplitude peaks at the natural resonance frequency of the

resonator design. For a drive voltage $v_D = V_B + v_d \sin(\omega t)$, where V_B is the DC proofmass bias and v_d is the AC drive amplitude, the in-plane displacement, u of the resonator at the midpoint of the 6 μm support beam (refer to Fig. 4.3) at resonance is given by [98],

$$u(t) = \frac{V_B Q}{k_{sys}} \frac{\partial C}{\partial x} v_d \sin\left(\omega t - \frac{\pi}{2}\right) \tag{4.4}$$

where k_{sys} is the system spring constant, $\partial C/\partial x$ is the incremental comb capacitance as a function of in-plane displacement, and Q is the quality factor at resonance.

Therefore, during resonance, the instantaneous velocity at the same point on the beam at time t is,

$$v(t) = \frac{du(t)}{dt} = \frac{V_B Q}{k_{sys}} \frac{\partial C}{\partial x} v_d \omega \cos\left(\omega t - \frac{\pi}{2}\right) \tag{4.5}$$

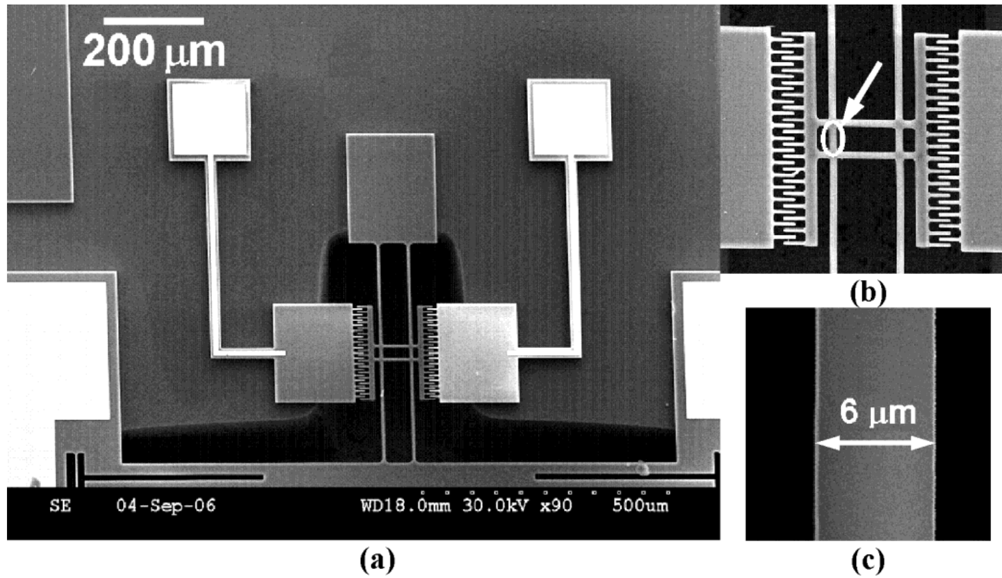

Fig. 4.3. SEM images showing the comb actuated resonator (labeled Device 1) used for measurement. (a) The overall resonator device. (b) 200X magnified image of the comb structures. Circled in white (arrowed) is the portion of the 6 μm support beam used for imaging. (c) The portion of the 6 μm beam circled in (b) at 10,000X magnification.

In these experiments, the sample device utilized was (labeled Device 1) driven at its fundamental resonance frequency of 161.762 kHz. The drive conditions applied were: DC bias, V_B = 24.0 V and AC drive, v_d = 0.10 V. The device has a measured Q of approximately 12,000 under a 10^{-3} Pa vacuum with theoretical values of k_{sys} = 237 N m^{-1} and $\partial C/\partial x$ = 1.8 nF m^{-1}. The Q values were found to be relatively constant within the 10^{-4} – 10^{-3} Pa base pressure range of the SEM. The theoretical peak velocity of the resonator given by Equation (4.5) is 0.222 m s^{-1}. Hence, from Equation (4.3), in order for the image capture system to freeze the motion of the resonator within one 24 nm digital pixel (10,000X SEM magnification) at t_{pixel} = 572 μs, the sampling gate width, t_{gate} of the boxcar integrator must not exceed 108 ns. A test of this motion freezing concept is presented next.

4.4.1. Stroboscopic motion freezing of dynamic resonator actuation

To show the effects of varying gate width, t_{gate} on stroboscopic image capture, the sample was driven at the above-mentioned drive conditions at its resonance frequency. Strobed image captures of a section of the sample's 6 μm support beam (refer to Fig. 4.3) were performed using t_{gate} between 10 ns – 3 μs, with the gating phase fixed at the resonator's peak instantaneous velocity (Gate A in Fig. 4.1). The resultant micrographs are presented in Fig. 4.4.

For t_{gate} of 100 ns and below (Fig. 4.4(a) – (c)), well-defined beam edges were obtained, indicating that the sampling gate width was narrow enough to freeze the resonator beam's motion. However, for t_{gate} of 300 ns and above, an increasing blurring of the beam edges is observed. These observations are in excellent agreement with the previous calculations of $t_{gate} < 108$ ns for stroboscopic motion freezing.

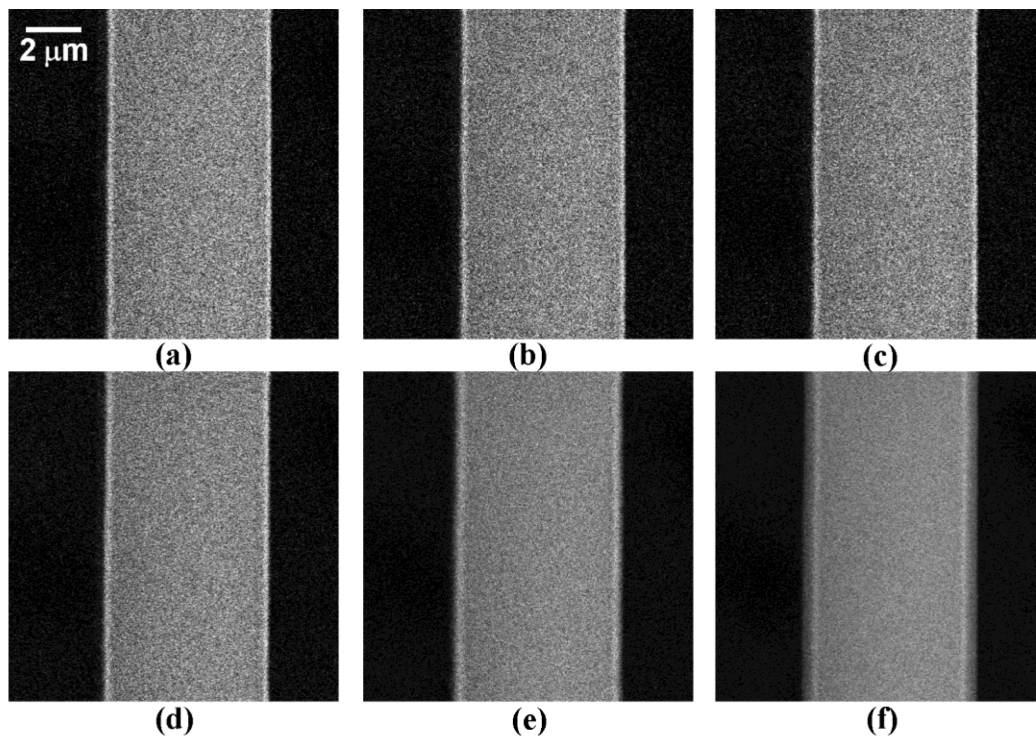

Fig. 4.4. Stroboscopic micrographs of 6 μm support beam at its peak velocity point captured using gate width t_{gate} of (a) 10 ns, (b) 30 ns, (c) 100 ns, (d) 300 ns, (e) 1 μs and (f) 3 μs.

As the SR250 provides a minimum t_{gate} of 2 ns, the stroboscopic system can effectively freeze the motion of a microstructure with a maximum instantaneous in-plane velocity of d_{pixel}/t_{min} = 24 nm pixel^{-1}/2 ns = 12.0 m s^{-1} (using Equation (4.3)).

4.4.2. Stroboscopic phase imaging

In the next set of experiments, the gate delay (or phase) was ramped at 1° (or 17.2 ns at 161.762 kHz resonance) per step during an image capture. A micrograph which tracks the displacement of the resonator over a single cycle (360°) or more can be generated. By increasing the gate delay ramp rate, it is possible to capture several cycles of resonator beam motion within one micrograph.

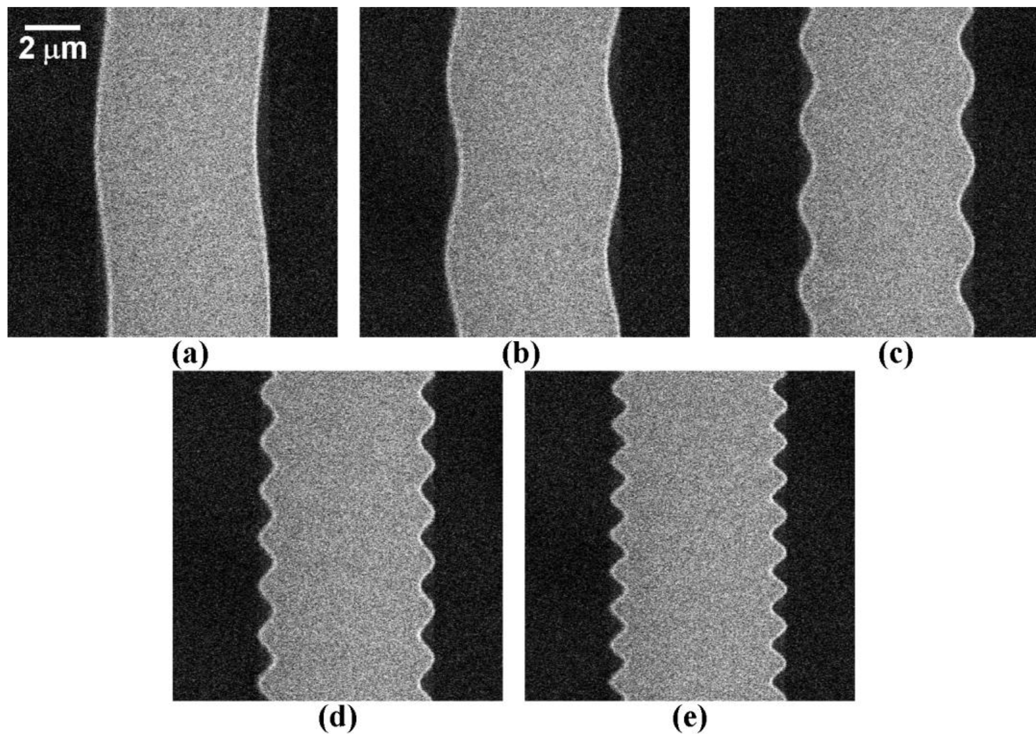

Fig. 4.5. Micrographs captured with different gate delay ramp rates to show several cycles of resonator beam displacement in a single micrograph. (a) Ramp rate 2.4° s^{-1} – 1 cycle, (b) ramp rate 4.8° s^{-1} – 2 cycles, (c) ramp rate 9.6° s^{-1} – 4 cycles, (d) ramp rate 16.8° s^{-1} – 7 cycles and (e) ramp rate 21.6° s^{-1} – 9 cycles. The gate width t_{gate} for all the captures is 30 ns.

The entire 512 × 512 pixel frame capture requires 150 s and hence, in order to obtain a displacement profile for one cycle of the resonator's motion, the gate delay ramp rate required would be 360°/150 s = 2.4° s^{-1} or 41.2 ns s^{-1}. Fig. 4.5 shows micrographs captured with five different gate delay ramp rates in order to obtain 1, 2, 4, 7 and 9 cycles of beam displacement. A gate width of 30 ns was used for each of the captures.

Note that increasing the delay ramp rate reduces the phase resolution of the final image. Taking the line scan time for the capture system as 150 s/512 = 0.293 s, the phase resolution of a 2.4° s^{-1} ramp rate is 2.4° s^{-1} × 0.293 s = 0.703°. If a smaller minimum resolvable phase is required, a lower phase delay ramp rate and a higher digital scanning resolution should be used. Table 4.1 summarizes the relationship between the delay ramp rate and phase resolution for the micrographs in Fig. 4.5.

Table 4.1. Ramp rate and phase resolution values for the micrographs in Fig. 4.5.

Ramp rate ($° s^{-1}$)	**Number of cycles**	**Minimum resolvable phase (°)**
2.4	1	0.703
4.8	2	1.41
9.6	4	2.81
16.8	7	4.92
21.6	9	6.33

The phase-resolved micrographs provide a qualitative picture of device motion and in the case of the resonator sample the vibration which occurs during actuation is observed to be sinusoidal in nature. In order to extract quantitative displacement data from the micrographs, some image processing is necessary and the procedure is described next.

4.4.3. Phase-resolved stroboscopic displacement quantification

Quantitative displacement data of resonator motion can be acquired from the phase-resolved stroboscopic images shown in Fig. 4.5. The displacement profiles can be extracted from the gray level intensities of the micrographs. Taking the upper-left corner as the origin (0, 0), a gray level line-profile at *y-y'* is obtained as shown in Fig. 4.6. The *x*-location of a resonator edge, i.e. the instantaneous displacement, is determined using the Full Width Half Maximum (FWHM) criterion.

By determining the edge *x*-pixel values for all 512 *y*-lines, a quantitative plot of the resonator's displacement (in nm) is obtained. Fig. 4.7 presents the displacement profile data extracted from micrographs (a), (c) and (e) in Fig. 4.5.

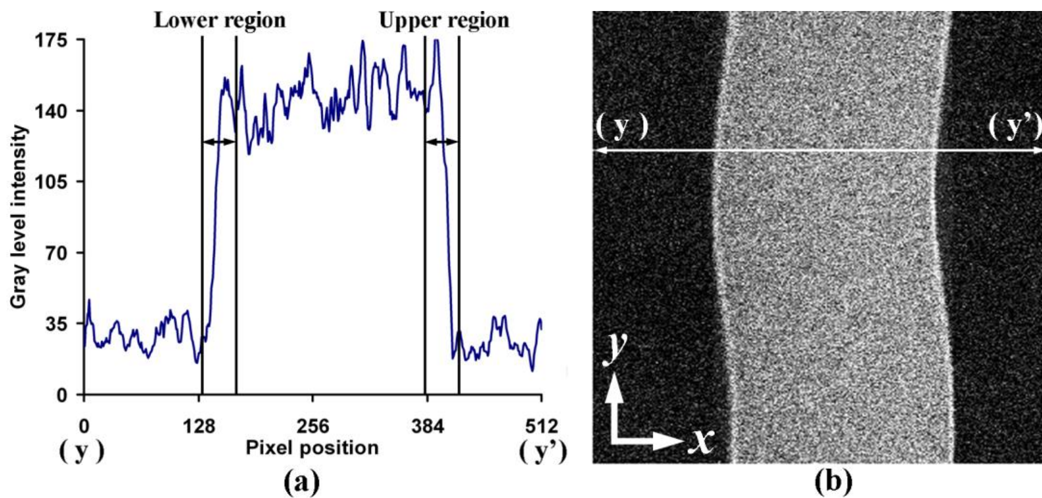

Fig. 4.6. (a) A 512 pixel-wide gray level intensity lineprofile of *y-y'* in the stroboscopic micrograph (b).

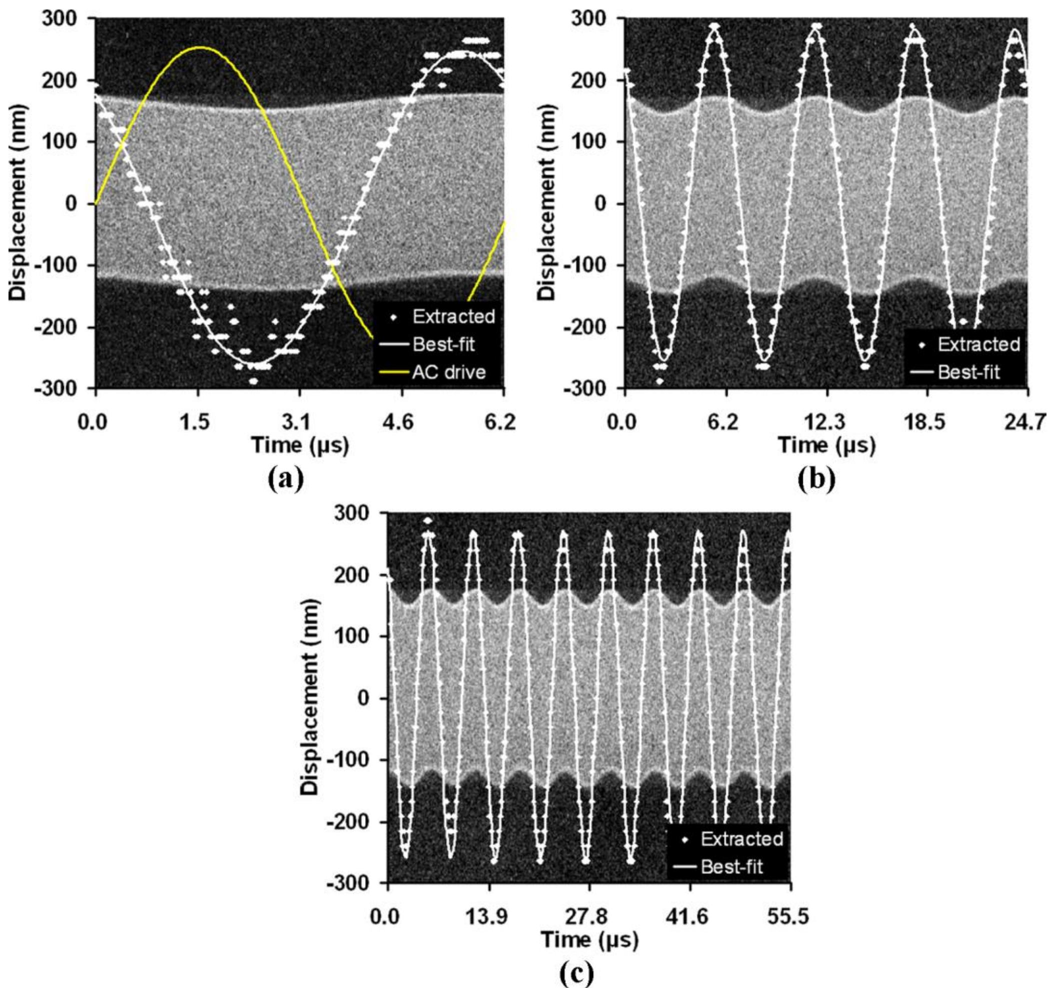

Fig. 4.7. Quantitative displacement plots (shown in white) for stroboscopic resonator imaging over (a) one (ramp rate 2.4° $s^{-1)}$, (b) four (ramp rate 9.6° s^{-1}) and (c) nine (ramp rate 21.6° s^{-1}) cycles of motion. The solid line shows the best-fit curve through the extracted data points. From (a), the fitted parameters for resonator peak displacement A_0 was 265 nm and the phase shift ϕ_0 was 127° (phase lead with respect to the AC drive signal).

Table 4.2. Standard deviation of the data points in the three resonator displacement.

Ramp rate (° s^{-1})	2.4	9.6	21.6
Standard deviation (nm)	19.61	22.78	22.29

Applying the method of least squares, the extracted data points were fitted to the equation

$$u(t) = A_0 \sin(\omega t - \phi_0) \quad (4.6)$$

where A_0, ω and ϕ_0 are the three fitting parameters. The best-fit curve represents the time-domain displacement variation of the vibrating beam from which the maximum amplitude A_0, vibration frequency ω and phase shift ϕ_0 (refer to Fig. 4.1) of the resonator can be obtained.

From Fig. 4.7(a), the best-fit parameters indicate that the resonator motion has a peak displacement of 265 nm with a 126º phase lead over the AC drive signal. Table 4.2 summarizes the standard deviation of the data points for the displacement profiles in Fig. 4.7. The current setup has an error tolerance of about 20 nm, with the primary electron probe size and digital scan resolution being the primary contributors. These will be discussed in more detail in Section 4.4.5. Aside from momentary displacement and phase measurements, the stroboscopic SEM technique can also provide vibration velocity estimates and these are discussed in the following section.

4.4.4. Time-resolved velocity estimation

Here, the stroboscopic motion freezing and phase-resolved imaging discussed previously in Sections 4.4.1 and 4.4.2 are combined. Keeping the gate delay ramp rate constant at 2.4° s^{-1} so that each micrograph would capture exactly one cycle of the

resonator's motion, the gate widths were varied from 10 ns – 3 μs to obtain the displacement profiles shown in Fig. 4.8.

The micrographs for t_{gate} < 100 ns show a sinusoidal shaped beam with well-defined edges as discussed previously. For t_{gate} > 300 ns, edge blurring was observed at positions where the resonator's in-plane velocity tends towards is peak. The greatest blurring occurs at the mid-point (zero-crossing) of the beam's sinusoidal motion where the instantaneous velocity is at its highest. At the positive and negative displacement peaks, the instantaneous velocity of the beam is zero and hence well-defined edges are always obtained.

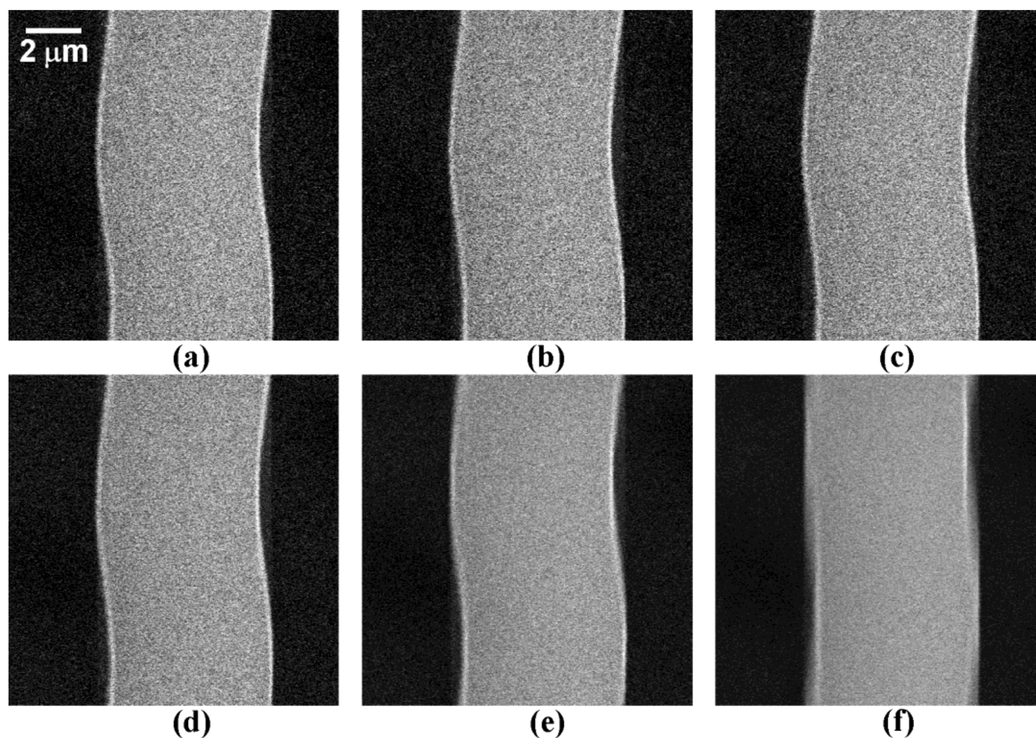

Fig. 4.8. Motion of 6 μm support beam (one cycle) captured using varying gate widths t_{gate} (a) 10 ns, (b) 30 ns, (c) 100 ns, (d) 300 ns, (e) 1 μs and (f) 3 μs.

Using the pixel spread from edge blurring and assuming a piecewise linear velocity interpolation, the instantaneous velocity of the resonator beam at various points of its motion can be estimated. Since the image capture only occurs within the sampling gate width, the pixel-spread divided by the gate width itself gives the velocity of the beam at the point of capture. This velocity measurement approach is only applicable for t_{gate} above the threshold width for freezing motion, and is also limited by the single-pixel digital resolution limit. On the other hand, t_{gate} must also not be so large that the entire amplitude of the beam's displacement is revealed by the edge blurring during capture. Due to the piecewise linear velocity interpolation, applying a smaller t_{gate} would provide a more accurate velocity measurement. However, decreasing t_{gate} also reduces the pixel-spread. As a pixel-spread of p pixels is required to obtain p distinct resonator velocity measurements, smaller pixel-spread would limit velocity resolution.

A t_{gate} value that is exactly ¼ of the resonator's period and synchronized to the 0° phase (zero crossing) would result in an edge blurring that is equivalent to its peak displacement. As the sample was actuated to vibrate at 161.762 kHz, the largest allowable t_{gate} which can be used to estimate its velocity is 1.55 μs. Therefore, for this particular resonator sample, 108 ns $< t_{gate} <$ 1.55 μs can be used for velocity measurement. With reference to the micrographs in Fig. 4.8, only t_{gate} = 300 ns (d) and t_{gate} = 1 μs (e) are applicable for velocity measurement based on the above-mentioned t_{gate} criteria. Here, Fig. 4.8(e) is used to demonstrate stroboscopic velocity measurement. To determine the amount of blurring which occurs at the resonator beam edges for a particular y-line, the previous FWHM criterion is applied to obtain the length of the blurred beam portion in pixels.

Table 4.3. Measured velocity values for the 8 resonator beam motion positions shown in Fig. 4.9. The deviation is the difference between the estimated and best fit values.

Time (μs)	**Measured velocity (m s^{-1})**	**Deviation (m s^{-1})**
0.072	–0.132	0.0131
1.12	–0.156	–0.0188
2.11	0.012	–0.0021
3.02	0.132	–0.0237
3.74	0.240	0.0366
4.34	0.144	–0.0064
4.90	0.036	–0.0321
6.13	–0.108	0.0229

The instantaneous velocity of the resonating beam was estimated for several points of its motion using Fig. 4.8(e). Table 4.3 tabulates the velocity values obtained using this approach. The resultant velocity profile is presented in Fig. 4.9 along with a best-fit curve obtained by the method of least squares estimation. The equation used for fitting was,

$$v(t) = V_0 \cos(\omega t - \phi_0) \qquad (4.7)$$

with V_0, ω and ϕ_0 being the fitting parameters. The estimated maximum velocity of beam vibration is hence given by the V_0 parameter.

The estimated maximum velocity of 0.192 m s^{-1} (from the best-fit curve) is in good agreement with the theoretical value of 0.222 m s^{-1} obtained using Equation (4.5). The velocity estimates have a standard deviation of 0.0224 m s^{-1} and represents the overall measurement accuracy of the technique. The maximum velocity which can be resolved by this method is equivalent to the maximum velocity of motion which the system can freeze, i.e. 12 m s^{-1}. At t_{gate} = 1 μs, the velocity resolution is 0.012 m s^{-1}.

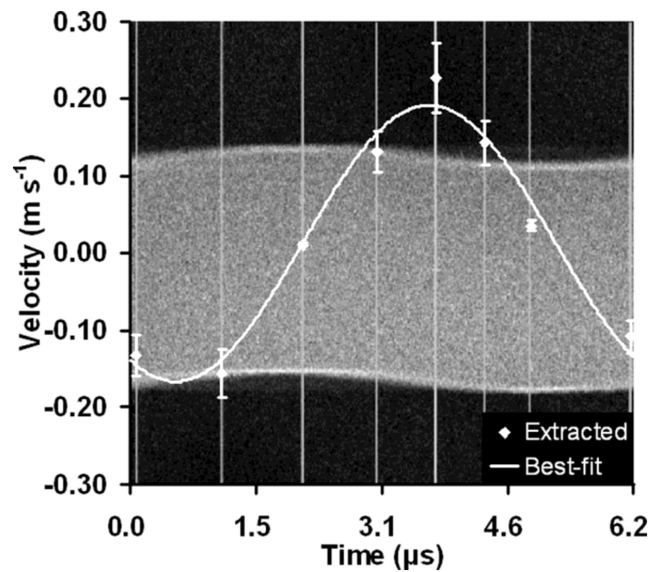

Fig. 4.9. Velocity profile (white curve) of resonating beam at 8 selected points of its motion. The peak velocity of the structure occurs at the point where the micrograph (Fig. 9(e)) shows the most blurring. From the best-fit curve, the estimated maximum velocity is 0.192 m s^{-1}.

In summary, the experiments on Device 1 have demonstrated the ability of the stroboscopic SEM setup in motion freezing, phase-resolved displacement imaging and motion velocity estimation. Phase-resolved displacement imaging is of particular importance as it is the means by which the physical motion of the device can be quantified. Next, the overall resolution capabilities of the technique for both displacement and velocity measurement are considered. Factors that limit resolution arise from two main sources: the electron probe of the SEM and the supporting digital electronics that sample the SE signal. These factors are discussed in the next section.

4.4.5. Experimental errors and limitations

Spatial and temporal factors

The SEM probe resolution is examined first. For the experiments presented, the S-3500 was configured with a working distance of 17.8 mm. At this setting, the best spatial resolution of the SEM is approximately 20 nm at 30 keV. This was determined

using the gold on carbon resolution test image in Fig. 4.10(a) obtained using identical SEM imaging conditions as the stroboscopic images presented here. The spatial resolution figure determines the smallest displacement which the stroboscopic system can possibly resolve (20 nm). With the S-3500 optimally configured for high resolution imaging, this measurement limit can be reduced to 10 nm (Fig. 4.10 (b)) or less. Since the sample resonators are expected to exhibit ~100 nm peak-to-peak in-plane displacement during linear operation, the detection threshold of 10 – 20 nm is sufficient for future experiments.

The digital sampling limits of the SEMICAPS SEM scanning and acquisition system must also be considered. The digital sampling rate of the SEM digital capture is 7.16 MHz for a 512 × 512 pixel, 4096X averaging, 150 s frame time image capture. Therefore, the stroboscopic imaging system is limited to resolving microstructure motion with frequencies below 3.58 MHz due to the Nyquist (2X) sampling limit. The digital sampling rate can, of course, be bettered by upgrading the system hardware, hence allowing for the motion of devices with higher frequency to be characterized.

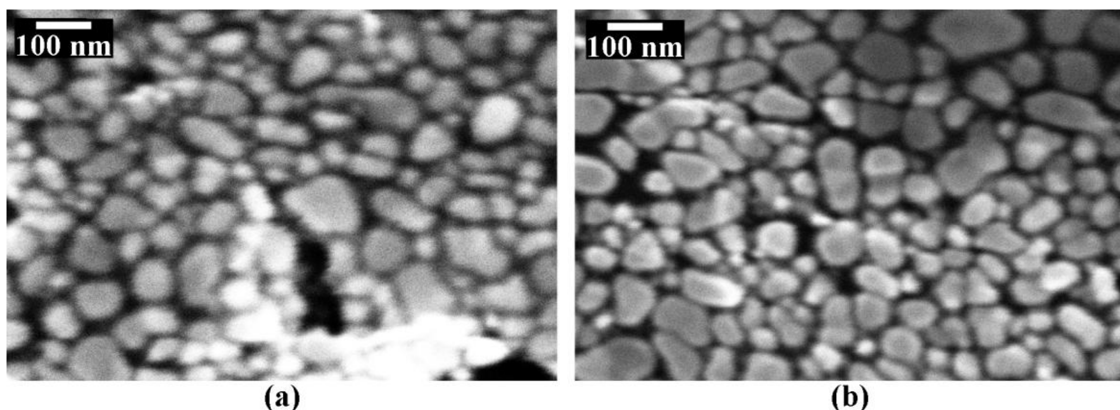

Fig. 4.10. 30 keV gold on carbon calibration micrographs (120,000X magnification) used for determining effective resolution of the S-3500 SEM: (a) Spatial resolution of ~20 nm for in-situ resonator experiments with working distance (WD) = 17.8 mm. (b) Best case resolution of ~10 nm with WD = 11.0 mm.

Ideally, the gate signal provided by the gated integrator/boxcar averager should be a perfect square waveform (Fig. 4.11). However, noise in the external trigger signal as well as the boxcar give rise to jitter in the final sampling gate. Fig. 4.11 shows the actual gate signal provided by the gated integrator/boxcar averager for t_{gate} = 1 μs compared with the ideal. The actual gate signal has finite rise and fall times of 42 ns and 94 ns respectively and a width of 1.1 μs, i.e. 10% larger than the specified t_{gate}. The SR250 gated-integrator/boxcar averager has a specified error of up to 20% in the gate timing. Since t_{gate} determines the extent of the observable edge blurring for velocity estimation, a 20% uncertainty in t_{gate} translates to an equivalent 20% error in the velocity estimates as well. Trigger delays also result in the gate signal being right-shifted by 365 ns when it should ideally be synchronized with the resonator's AC drive signal. This 365 ns delay contributes to a phase offset error during displacement/velocity profiling.

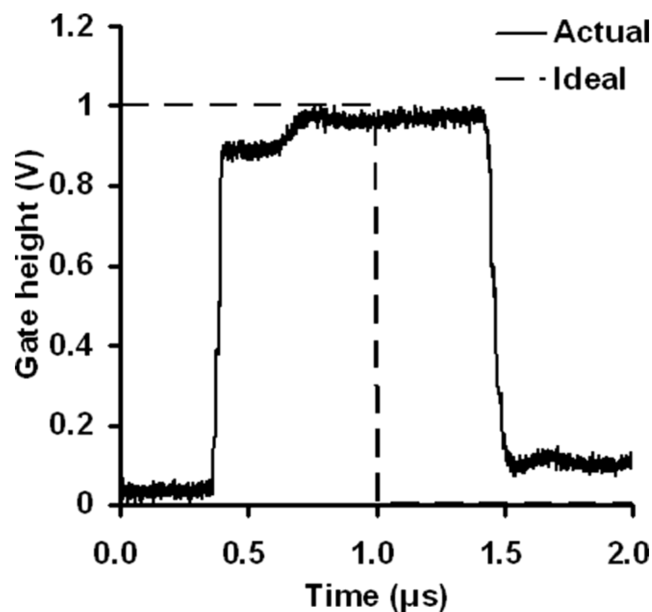

Fig. 4.11. Actual 1 μs gate signal provided by the SR250 gated-integrator/boxcar averager compared with ideal.

The issues presented in this section reflect the physical limitations on resolution and accuracy of the technique imposed by the system hardware (which includes the SEM itself and the signal gating and digital sampling electronics). When considering the accuracy of the displacement data obtained, it is also necessary factor in the error sources contributed by the image processing step (Section 4.4.3). These are discussed next.

SEM image noise and other contributions to inaccuracies

During the SEM scan, the electron beam introduces several types of noise to the image signal and these include shot noise, secondary electron noise and partition noise [100]. The gated integrator/boxcar averager also contributes to noise in the final image signal.

As the individual noise components cannot be quantified, a final image-based approach to analyzing overall system noise is hereby adopted. Consider the 30 ns gate micrograph in Fig. 4.4(b). In the dark areas of the image, the gray level intensity of these areas has a mean of 24 intensity units and a standard deviation of 24. Hence, it can be assumed that all the noise sources for this particular capture give rise to an uncertainty of ±24 gray level intensity units per pixel. Table 4.4 shows the average gray level intensities for all 512 y-pixels at 12 x-lines obtained from the 30 ns gate micrograph in Fig. 4.4(b). The asterisk (*) marks the average cut-off point found by adhering to the FWHM criterion, with 90.4 being the average threshold intensity. Considering the ±24 intensity units uncertainty provided by the noise, it is possible for both pixels 152 and 154 to have an intensity which comes within range of the threshold value and be taken as the cut-off pixel also.

Table 4.4. Average gray level intensity for all 512 y-pixels at 12 x-lines around the cut-off pixel (obtained from Fig. 4.4(b)).

***x*-pixel no.**	150	151	-152	* 153	-154	155	156	157	158	159	# 160	161
Gray level intensity	48.3	58.4	72.1	87.9	106	129	149	166	176	179	181	180

Hence, in the worst case, the background noise contributes a ±1 pixel error to the displacement profile obtained. Since the pixel-to-displacement conversion is 24 nm pixel^{-1}, the error in the profile extraction is hence ±24 nm. This error can be improved by reducing the pixel-to-displacement conversion (i.e. by using a larger SEM magnification during imaging), although the ultimate resolution of the technique is still determined by the SEM probe size as discussed in the previous section.

Applying the same analysis to the remaining five micrographs in Fig. 4.4, it was found that the gray level uncertainty caused by the background noise decreases when a larger gate width is used. The numbers are summarized in Table 4.5. This is not unexpected as increasing the gate width raises the signal to noise ratio (SNR). For the 1 µm and 3 µm gate widths, the SNR is large enough such that the gray level variation caused by the noise does not cause significant error in the displacement extraction. However, such large gate widths are not practical due to the t_{gate} < 108 ns requirement for stroboscopic motion freezing discussed previously.

Table 4.5. Mean and standard deviation of gray level intensity variation caused by background noise for image captures performed using different t_{gate}. This variation translates into a pixel error during the displacement profile extraction.

Gate width	**Mean intensity**	**Std dev**	**Error (pixel)**
10 ns	24	27	±1
30 ns	24	24	±1
100 ns	25	23	±1
300 ns	26	20	±1
1 µs	26	13	0
3 µs	24	9	0

Table 4.6. Comparison of other techniques for measuring the dynamic motion of micromechanical structures with the stroboscopic SEM developed in this work.

	In-plane resolution	**Accuracy**	**Displacement quantification**
LDV (Ferraris et al. [25])	5 µm	pm range	Doppler shift measurements
Optical stroboscopy (Rembe et al. [34])	600 nm	100 nm	Motion freezing, sub-pixel image processing
SEM (Roy et al. [35])	~2 nm	Poor	Blur synthesis
Stroboscopic SEM	20 nm	nm range	Phase-resolved imaging

In summary, stroboscopic SEM is able to freeze and image device motions down to about 20 nm, limited by the electron probe size of the SEM. The frequency limit of the system is determined to be ~3.58 MHz with the sampling rate of the digital image acquisition system being the main bottleneck. With a more advanced imaging system, devices of higher frequency can be characterized. Uncertainties in the gate signal from the gated integrator/boxcar averager also result in some phase offset error during displacement/velocity profiling. When extracting quantitative displacement information from the stroboscopic phase-resolved images, errors contributed by image noise must also be considered. These errors, however, can be effectively regulated by using an appropriate SEM magnification during imaging.

To highlight its dynamic motion quantification capabilities, stroboscopic SEM is compared to other resonator displacement measurement techniques and these are summarized in Table 4.6. In terms of in-plane resolution, stroboscopic SEM is significantly better than optical and laser-based (LDV) techniques since both these methods are diffraction limited. Although it cannot achieve the 2 nm resolution of conventional SEM imaging, the phase-resolved imaging and displacement

quantification in stroboscopic SEM provide substantially better accuracy when obtaining measurements compared to the blur synthesis method used in conventional SEM. In any case, the minimum displacements of most micromechanical structures currently under development have yet to reach the sub-10 nm regime. Overall, there is a good compromise between resolution and accuracy which allows stroboscopic SEM to be employed for measuring the dynamic motions of most micromechanical structures.

4.5. Conclusions

A system for dynamic in-plane stroboscopic SEM imaging and displacement-velocity quantification of MEMS devices was presented in this chapter. Stroboscopy was achieved by time-gated sampling of the SEM SE signal. Stroboscopic imaging experiments were carried out on a comb actuated clamped-clamped beam resonator. By varying the phase delay of the gate signal, the instantaneous displacement of the resonator at various phases of its motion can be captured. The technique can further be applied to obtain a phase-resolved image of the motion of resonator during actuation by ramping the phase delay of the gate signal while imaging. The current hardware implementation can achieve a displacement resolution of about 20 nm, limited mainly by the electron probe size, for motion frequencies up to 3.58 MHz. Resonator instantaneous velocity for in-plane motions up to 12 m s^{-1} can also be measured using pixel blurring analysis with a velocity resolution of 0.012 m s^{-1}. Improvements to various hardware components can enhance both resolution and frequency limits of the system. Overall, when compared to other dynamic motion measurement techniques, there is a good compromise between resolution and accuracy which allows

stroboscopic SEM to be employed for measuring the dynamic motions of most micromechanical structures. The following chapter presents long-term frequency stability experiments that were carried out utilizing the two motion detection tools introduced in Chapters 3 and 4. Stroboscopic SEM has the function of calibrating the phonon setup for monitoring device displacement drift over long-term actuation.

CHAPTER 5

LONG-TERM FREQUENCY STABILITY OF SILICON CLAMPED-CLAMPED BEAM RESONATORS

5.1. Introduction

Silicon based micromechanical resonators have long been recognized as a promising alternative technology to quartz oscillators for many frequency reference and timing applications [50]–[55]. In fact, companies including Discera Inc., SiTime and Silicon Clocks are already marketing a wide range of oscillator products based on silicon resonators. However, very little published information exists on the long-term stability of these devices despite its importance in assessing device reliability. Current studies on resonator long-term stability are carried out using network analyzer-based systems. However, as mentioned in Chapter 2, these test setups have their own short-comings when determining the frequency characteristics of test devices, some of which include parasitic effects and feedthrough interference [46].

This chapter presents an automated test setup based on phonon detection for monitoring the long-term stability of micromechanical resonator devices. Phonon detection does not suffer form parasitic effects since the characterization signal is mechanical in nature (acoustic phonons). The automated test system developed is able to continuously actuate up to four devices (which can be scaled up easily) and characterize them at regular intervals to monitor resonance frequency f_0 and Q-factor changes resultant from long-term operation. Device displacements at resonance can also be derived from the phonon voltage V_{phonon} recorded, with the voltage displacement conversion being provided by stroboscopic SEM.

The subject of this long-term stability study is comb actuated clamped-clamped beam resonators. Due to their simple structure, compact size and power efficiency, clamped-clamped beam resonators are ideal candidates for various frequency reference and signal processing applications [101]–[102]. The short term stability parameters of clamped-clamped beam devices, such as phase noise [55],[103] and thermal frequency stability [61],[66], are well explored, but their long-term performance has not been investigated sufficiently. A summary of some published studies on micromechanical resonator long-term performance is shown in Table 5.1. Of notable interest is the fact that most of these studies are based on a fairly small number of devices and hence it would be difficult to generalize the observed long-term behaviour to the device population. In addition, no resonator failure mode has been identified in any of these tests, quite possibly because the measurement method used was an electrical technique (network analyzer) which does not assess/track changes in the mechanical state of the device over time.

Table 5.1. Summary of some published studies on long-term performance of micromechanical resonators.

	Resonators studied	Actuation time	Measurement method	Freq. drift	Failure modes
Koskenvuori et al. [70]	4 x length ext.	1,000 hrs	Network analyzer	~1 ppm day^{-1}	None
Kaajakari et al. [71]	2 x square ext. 2 x cantilever 2 x c-c beam 2 x piston	700 hrs	Network analyzer	0.5 – 15 ppm day^{-1}	None
Kim et al. [72]	6 x ring resonator (2 designs)	~9,000 hrs	Network analyzer	>>1 ppm day^{-1}	None

The phonon detection methodology used in this work, on the other hand, does have the capability of evaluating the phonon transmission or energy dissipation properties of resonator devices (see Section 3.2.2). Hence it is possible for the technique to identify device failure modes associated with changes in this particular aspect (i.e. energy dissipation) of device mechanical state. Applying the phonon detection technique, the experiments performed here focus on f_0, Q-factor and in-plane displacement variation over time. These three parameters were used to analyze the long-term performance of the devices.

5.2. Micromechanical comb actuated clamped-clamped beam resonators

A specimen of the comb actuated clamped-clamped beam resonators that are studied in these long-term stability experiments is shown in Fig. 5.1. These devices were fabricated using the SOIMUMPs process provided by MEMSCAP. This process features a structural layer of phosphorus doped silicon with thickness h = 25 µm and has minimum feature sizes of 2 µm [104]. The resonators are actuated by applying a

DC proof-mass bias V_B to the clamped-clamped beam and an AC drive voltage v_d to one of the comb actuators. The periodic electrostatic force generated by the applied voltages excites the resonator into vibration and the in-plane vibration amplitude reaches a maximum as the frequency of v_d approaches the resonance frequency f_0 of the resonator. As these resonators are designed to operate in the fundamental mode, the peak displacement occurs at the mid-point of the clamped-clamped beam. The fundamental f_0 is determined by the length L, width w and height h of the beam structure and is given by [105],

$$f_0 = \frac{\beta_0^{\;2}}{4\sqrt{3}\pi}\sqrt{\frac{Ew^3h}{ML^3}} \tag{5.1}$$

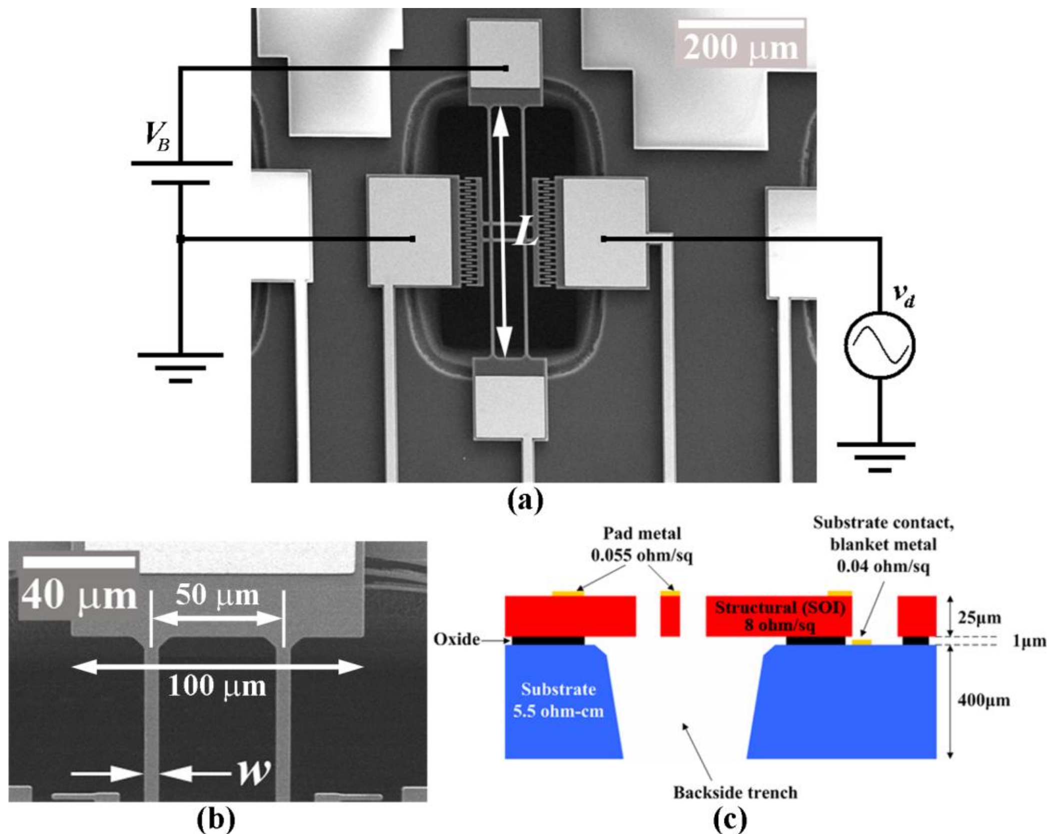

Fig. 5.1. (a) SEM micrograph of a specimen of the comb actuated clamped-clamped beam devices used in the long-term stability experiments. The devices were fabricated using the SOIMUMPs process. (b) Magnified image of the resonator anchor structures with W = 100 µm and w = 6 µm. The beam length L = 400 µm is shown in (a). (c) Cross-section schematic of the device showing the SOI structural layer and the substrate.

where E is the Young's modulus of the resonator material (silicon in this case), M is the mass of the beam (volume × density of silicon), L and h are the length and height of the beam respectively, w is the width of the beam in the direction of vibration and β_0 is the mode constant. For these resonator samples, L = 400 µm, w = 6 µm (h = 25 µm as determined by the SOIMUMPs process) and β_0 = 3.40 which gives f_0 ~ 167 kHz.

To examine the long-term performance of these devices, they are continually actuated and observed for changes in their resonance frequency f_0, Q-factor and in-plane displacement over time. However, while monitoring the Q-factor and in-plane displacement parameters are fairly straight-forward, assessing f_0 stability is tricky as there are multiple contributing factors which can give rise to f_0 shift.

One of these is fluctuations in the ambient temperature. The clamped-clamped architecture of the device means that the structure is particularly prone to axial stress since the beam is anchored at both its ends. Temperature fluctuations cause the clamped-clamped beam to expand and contract, thereby altering the magnitude of axial stress on the beam. Since it is well-known that this stress tends to cause the f_0 of the resonator to shift [62], it can be deduced that temperature fluctuations also have an adverse effect on f_0 stability. To isolate the f_0 shift caused by fatigue degradation, it is therefore necessary to decompose the effects of temperature. Some knowledge of the temperature frequency sensitivity of the device is required, and this is discussed in the following section.

5.2.1. Temperature frequency sensitivity

The thermal frequency sensitivity of a resonant structure is characterized by the temperature coefficient of resonance frequency TC_f which is the rate of change of its resonance frequency with temperature with respect to a reference frequency. In this section, a simple theoretical model is presented for the TC_f of clamped-clamped beam resonators along with a method for determining the TC_f value of a sample device. Determining the sample TC_f allows decomposition of the effects of ambient temperature fluctuations on the measured frequency drift during long-term frequency stability experiments.

First consider the clamped-clamped beam resonance frequency f_0 expression given in Equation (5.1). The temperature dependent parameters in Equation (5.1) include the mode constant, the silicon Young's modulus and the beam dimensions which expand when heated. Hence, the TC_f of the resonator is,

$$\begin{aligned} TC_f &= \frac{1}{f_0}\frac{\partial f}{\partial T} = \frac{2}{\beta_0}\frac{\partial \beta}{\partial T} + \frac{TC_E}{2} + \frac{\alpha}{2} \\ &= \frac{2}{\beta_0}\frac{\partial \beta}{\partial \sigma}\frac{\partial \sigma}{\partial T} + \frac{TC_E}{2} + \frac{\alpha}{2} \end{aligned} \tag{5.2}$$

with TC_E being the temperature coefficient of Young's modulus of silicon and α being the coefficient of thermal expansion of the resonator material. To find $\partial\beta/\partial T$, first consider the effects of axial stress σ on β and then determine how σ changes with temperature.

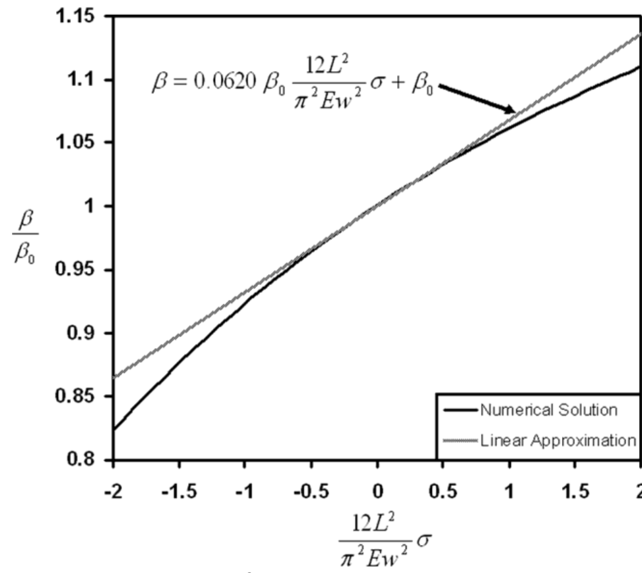

Fig. 5.2. Variation of mode constant β with axial stress. The numerical solution predicts a non-linear relationship between β and the stress parameter. For small stresses, a linear approximation about the zero stress point can be applied.

The mode constant β has a non-linear dependence on axial stress acting on the resonator structure (see Fig. 5.2) [105]. However, for small stresses, a linear approximation about the zero stress point can be applied,

$$\begin{aligned} \beta &= 0.0620\beta_0 \frac{12L^2}{\pi^2 E w^2}\sigma + \beta_0 \\ \frac{\partial \beta}{\partial \sigma} &= 0.744\beta_0 \frac{L^2}{\pi^2 E w^2} \end{aligned} \tag{5.3}$$

Changes in the axial stress on the clamped-clamped beam with temperature can be caused by a mismatch in the thermal coefficients of expansion α in the die or even in the packaging material and can be expressed as,

$$\frac{\partial \sigma}{\partial T} = E\frac{\partial \delta}{\partial T} \tag{5.4}$$

where E is the Young's modulus of silicon and $\partial\delta/\partial T$ is the thermal induced axial strain acting on the clamped-clamped beam structure. Combining Equations (5.2), (5.3) and (5.4),

$$TC_f = 0.151\left(\frac{L}{w}\right)^2 \frac{\partial \delta}{\partial T} + \frac{TC_E}{2} + \frac{\alpha}{2} \tag{5.5}$$

TC_E of silicon is approximately –77.56 ppm $^{o}C^{-1}$ due to material softening [58] and with α = 2.6 ppm $^{o}C^{-1}$, these last two terms in Equation (5.5) account for –37.48 ppm $^{o}C^{-1}$ change in f_0 with increasing temperature. From Equation (5.5), it is immediately evident that for clamped-clamped beam resonators which experience thermal induced strain (i.e. $\partial\delta/\partial T \neq 0$), the TC_f will be moderated by the first term in the equation.

The TC_f of a resonator sample can be determined simply by characterizing the device and determining its f_0 at several temperature steps within a certain temperature range. By plotting f_0 against temperature, the slope of the plot gives the TC_f of the device. Fig. 5.3 shows the variation in resonance frequency f_0 of a specimen of the clamped-clamped beam resonators (labeled as Device R01) for temperatures between 25 °C and 80 °C. From the slope of the f_0-temperature plot in Fig. 5.3, the TC_f of Device R01 can be determined to be –12.67 Hz $°C^{-1}$ or –73.87 ppm $°C^{-1}$. Having established the TC_f, this value can then be used to account for the resonator frequency shift contributed by temperature fluctuations in later experiments.

Aside from providing a basis for compensating the effects of temperature fluctuations, the TC_f data of the device can also provide some insight on the axial stress that is present on the beam structure. This is discussed in the next section.

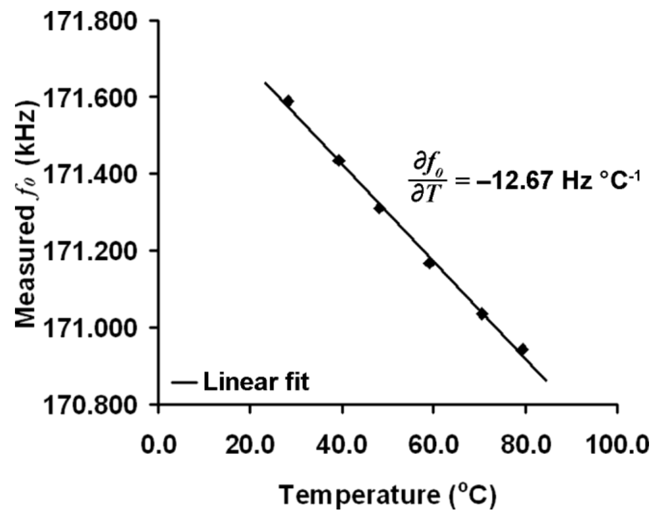

Fig. 5.3. f_0-temperature plot for Device R01. The temperature coefficient of resonance frequency TC_f of the device is determined from the slope of the linear best-fit line. The best-fit line is obtained using line regression by the method of least squares. In this case, the TC_f of Device R01 is –12.67 Hz °C^{-1} or –73.87 ppm °C^{-1}.

5.2.2. Axial stress on clamped-clamped beams

The presence of axial stress on the resonator is expected due to the clamped-clamped disposition of the vibrating beam structures. As it is possible that the presence of this stress could have a detrimental effect on the long-term performance of the resonator, it is therefore necessary to estimate the magnitude of the axial stress on the beams. The axial stress can, in fact, be derived from the f_0-temperature measurements carried out on the sample device.

Referring back to Equation (5.5) of the TC_f model presented in the previous section, it can be deduced that there are two main contributors to the temperature frequency sensitivity of the resonator: its material properties (E which is temperature dependent) and thermal induced strain.

For packaged resonators, the most common source of thermal induced strain is from the package materials which have thermal expansion coefficients and material

properties that differ substantially from the resonator material (silicon) [61]. However, as the devices are tested at the die level, they do not experience these package stresses when heated. This suggests that the strain arises at a more fundamental level: from a mismatch in the thermal expansion coefficients of the resonator SOI structural layer and the silicon substrate (see Fig. 5.1 for structural layer and substrate). Hence,

$$\frac{\partial \delta}{\partial T} = -(\alpha_{SOI} - \alpha_{sub}) \tag{5.6}$$

where α_{SOI} and α_{sub} are the thermal expansion coefficients of the SOI structural layer and the substrate respectively. Combining Equations (5.5) and (5.6),

$$TC_f = -0.151(\alpha_{SOI} - \alpha_{sub})\left(\frac{L}{w}\right)^2 + \frac{TC_E}{2} + \frac{\alpha}{2} \tag{5.7}$$

Hence, after the TC_f of a sample has been determined, its coefficient mismatch can be worked out as,

$$(\alpha_{SOI} - \alpha_{sub}) = \frac{1}{0.151}\left(\frac{w}{L}\right)^2\left(TC_f - \frac{TC_E}{2} - \frac{\alpha}{2}\right) \tag{5.8}$$

In the case of Device 01 (in the previous section), $(\alpha_{SOI} - \alpha_{sub}) = -0.0542$ ppm °C^{-1} (with L = 400 μm and w = 6 μm). With the occurrence of this mismatch, the axial stress on the clamped-clamped beams can be estimated by,

$$\begin{aligned} \sigma_T &= E(\alpha_{SOI} - \alpha_{sub}) \times T \\ &= \frac{E}{0.151}\left(\frac{w}{L}\right)^2\left(TC_f - \frac{TC_E}{2} - \frac{\alpha}{2}\right) \times T \end{aligned} \tag{5.9}$$

with T being the temperature of the device. The derived σ_T is therefore the induced axial strain on the resonator beam at temperature T due to the thermal expansion

coefficient mismatch ($\alpha_{SOI} - \alpha_{sub}$). In the case of Device R01, $\sigma_T = -2.693$ MPa at 301 K (28 °C).

Hence, from the measured TC_f of the device, it is possible to approximate the axial stress on the clamped-clamped beam structure. These stress estimates will be useful in future experiments for comparing the effects of axial stress on resonator long-term performance across different device samples. In the following section, the test setup, designed based on the phonon detection technique, for monitoring long-term performance of resonators is presented.

5.3. Experimental setup

The phonon detection technique is capable of detecting the motion of multiple devices with the same transducer element and only a single set of electronics (a voltage preamplifier) is required for measurement. Hence, the test setup required for monitoring the performance of a large number of devices can be fairly simply implemented. This is particularly advantageous for long-term performance testing in the manufacturing process, since a large volume of samples has to be tested in order to generalize the performance of a batch of devices. Although the multiple devices have to be measured sequentially, the data acquisition time per resonator is short and the change-over time between devices is negligible (since the same piezoelectric element is used for all devices). The technique is therefore able to characterize a large number of devices in a relatively short time frame.

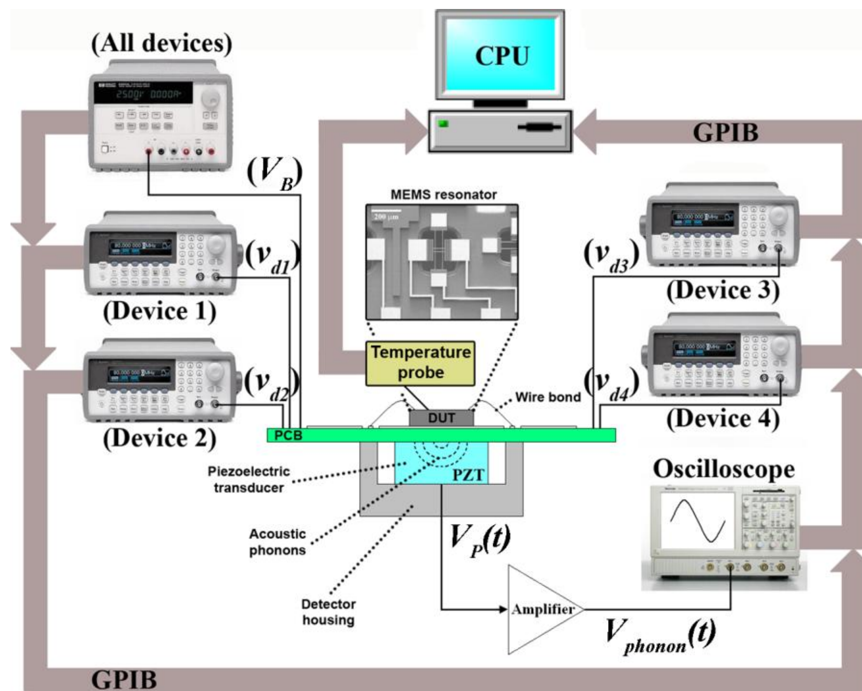

Fig.5.4. Automated phonon detection setup for monitoring the long-term stability of resonator devices.

The phonon detection setup for investigating the long-term stability of the resonator devices is shown in Fig. 5.4. The test die is mounted onto a copper-plated PCB board through which the actuation voltages are fed to the devices-under-test (DUTs). Wire bonds are made to the resonator contact pads to provide the electrical contacts to the devices. The temperature of the test die is monitored using a thermocouple probe which is held in place on the test die surface using a micromanipulator. In order to ensure that the PCB board does not couple additional stress onto the test die, only one corner of the die is attached to the board using silver conductive paste. This mounting holds the test die in place while minimizing external forces from coupling to the die.

The PCB board is then bolted on top of the phonon detector which consists of the piezoelectric transducer and the preamplifier circuitry. As the piezoelectric transducer can detect the motion of any device on the sample die, the same transducer can be used

to characterize multiple devices with high throughput. The output waveform of the piezoelectric transducer $V_P(t)$ is amplified by the preamplifier before being read on a digital oscilloscope to provide the phonon waveform $V_{phonon}(t)$. The preamplifier was redesigned to have a voltage gain of 1453 and 3-dB bandwidth of 206 kHz. Device characterization is carried out in a vacuum chamber which has a nominal base pressure of $10^{-3} - 10^{-2}$ Pa.

To characterize the resonator DUTs, a DC proof-mass bias V_B and an AC drive voltage $v_{d1} - v_{d4}$ are applied respectively to the four devices in sequence. This process is carried out using an automation and data acquisition software coded with LabView. The software is run on a control computer (CPU) which communicates with the instruments through the general-purpose interface bus (GPIB) port (see Fig. 5.4). The DC bias voltage is provided by a HP E3631A power supply and four Aglient 33250A arbitrary function generators supply the sinusoidal drive voltages. The phonon voltages are monitored by a Tektronix TDS5034B digital oscilloscope. In a typical characterization run, a DC voltage V_B is first applied to all four devices. Device 1 is then actuated with AC drive voltage v_{d1}. The frequency of the AC drive is swept upwards and the phonon voltage V_{phonon} at each frequency step is read by the oscilloscope and recorded in order to map the frequency response of the sample. When the frequency sweep for Device 1 is complete, v_{d1} is shut off. The automation software then repeats this process for Devices 2 to 4 by activating v_{d2} to v_{d4} sequentially.

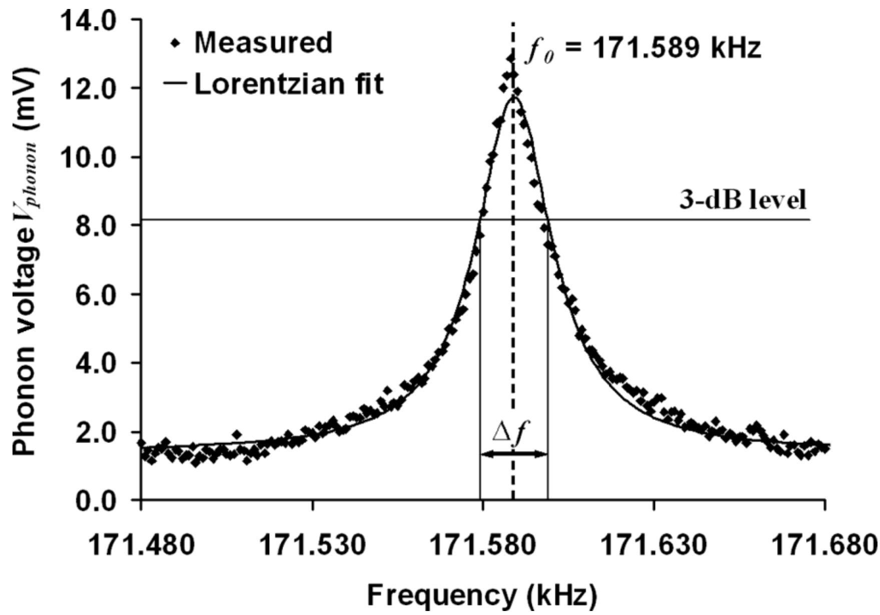

Fig. 5.5. Frequency response curve of Device R01 obtained using phonon detection at 28.6 °C and ~2 x 10^{-2} Pa. The device was actuated with V_B = 6.0 V and v_d = 30 mV. The measured f_0 = 171.589 kHz and Q = 10,200 as determined from the best-fit Lorentzian curve.

The frequency response of a typical device (labeled Device R01) is shown in Fig. 5.5. From the recorded frequency response, the resonance frequency f_0 and Q-factor of the sample can be ascertained. A best-fit Lorentzian curve is first drawn through the measured points (fitting is done by the method of least squares). The f_0 is determined from the point at which the best-fit curve is maximum which is 171.589 kHz.

The Q-factor is computed using the equation,

$$Q = \frac{f_0}{\Delta f} \tag{5.10}$$

where Δf is the range of frequencies for which the phonon voltage amplitude is at least 0.707 of the maximum phonon voltage at f_0 (3-dB level) as determined from the best-fit curve in Fig. 5.5. In this case, Q turns out to be 10,200.

This phonon detection setup was used to evaluate the long-term stability of the comb actuated clamped-clamped beam resonators. Since it is also necessary to monitor the

peak displacements of the devices over time, calibrating the voltage-displacement gain of the detection setup is therefore required. This is presented next.

5.3.1. Motion detection calibration

Before performing long-term stability tests, calibration experiments were carried out to determine the voltage-displacement gain of the phonon detection setup. Knowledge of the voltage-displacement gain allows for estimation of the in-plane displacement of the device from the recorded phonon voltage V_{phonon}. As the phonon coupling may vary across devices, depending on the condition of the contact between the sample die, PCB board and piezoelectric transducer, it is hence necessary to obtain the voltage-displacement gain for each DUT. In the calibration experiments, the mounted sample device is characterized simultaneously by phonon detection and stroboscopic SEM to derive its frequency response. Details of the technique were presented in Chapter 4.

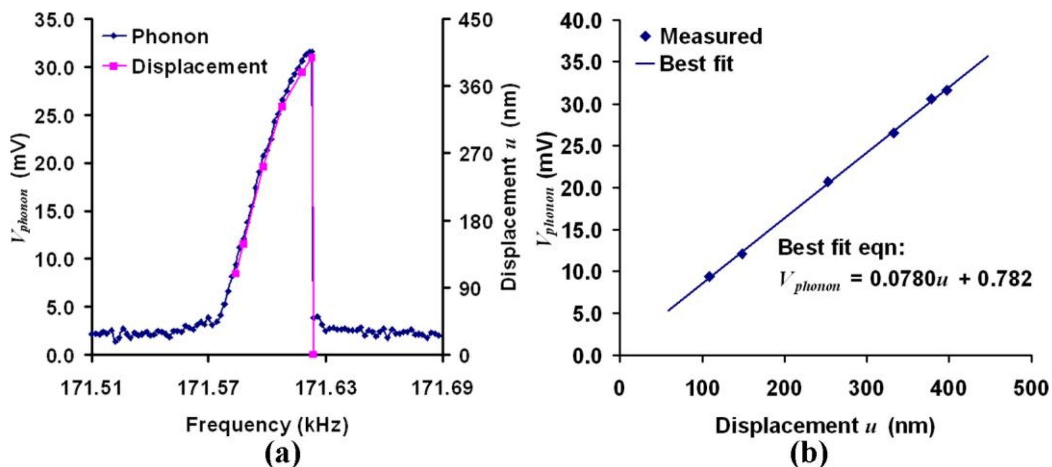

Fig. 5.6. (a) Non-linear frequency response of Device R01 obtained by phonon detection (V_{phonon}) and by stroboscopic SEM (displacement) at 28.6 ^{o}C and ~2 x 10^{-2} Pa. The resonator was actuated at with V_B = 15.0 V and v_d = 60 mV. (b) Voltage-displacement relation of the phonon detector obtained using six points from both curves in (a). The gradient of the best fit equation (by linear line regression) gives the voltage-displacement gain of the detector for this particular device.

To characterize the device, the frequency of the drive voltage v_d is swept upwards and the resonator motion is imaged at several frequency steps. The displacement measurements are then extracted from the SEM micrographs to obtain the final frequency response curve. Fig. 5.6(a) shows the frequency response curves obtained by both phonon detection and stroboscopic SEM when Device R01 was actuated with V_B = 15.0 V and v_d = 60 mV (non-linear mode). The resonator was actuated to non-linear displacements as the larger motion amplitudes provide a wider range of values for mapping the voltage-to-displacement. Even at large displacement amplitudes, the linear relationship between voltage and displacement is maintained as shown in Fig. 5(b). The gain of the detector is determined from the gradient of the curve in Fig. 5(b) to be 0.0780 mV nm^{-1}. This corresponds to a phonon coupling factor κ of 1.15×10^{-5} (calculated using Equation (3.27)) with G = 1453. This value is significantly lower than the coupling factors achieved in Chapter 3, but it is not unexpected as the addition of the PCB board in between the sample and the transducer introduces two addition interfaces between die and PCB and between PCB and transducer. These two interfaces are likely to contribute some transmission loss as the coupling at the interfaces is not perfect.

Once the voltage-displacement gain for each device is known, the physical in-plane displacements can then be calculated from the recorded phonon voltages V_{phonon}. These calculated displacements can be used to monitor device stability over time. In the next section, the measured long-term stability parameters for the resonators are presented using one device as an example. The same parameters were monitored for all the sample devices in this study.

5.3.2. Measured stability parameters

The long-term stability of the clamped-clamped beam resonators was examined by monitoring several sample devices of the same design (with L = 400 μm and w = 6 μm). Each resonator was actuated and characterized every 30 minutes over a period of 500 hours using the automated phonon detection test setup described earlier. From the recorded frequency response curves obtained over the actuation period, three key resonator parameters were extracted: the resonance frequency f_0, Q-factor and peak in-plane displacement (calculated using the voltage-displacement gain). The variation of these three parameters over time can be used to assess the long-term performance of the devices.

Figure 5.7(a) shows the recorded f_0 of Device R01 over the actuation period. The large local fluctuations in the f_0 are indicative that there is some form of external disturbance acting on the device and hence the frequency shift is not the true drift resultant from long-term actuation. An inspection of the recorded surface temperatures of the device over the actuation period (see Fig. 5.7(b)) reveals significant fluctuations of about ±1.8 °C over the 500 hours. Having established that the device TC_f is –73.87 ppm °C^{-1} (see Section 5.2.1), the effects of temperature on frequency shift can hence be decomposed. This is achieved by using the recorded temperature data to derive the temperature compensated resonance frequency f_C,

$$f_C(n) = f_0(n) - [T(n) - T_{ave}] \times [TC_f \times f_0(n)] \tag{5.11}$$

where $f_0(n)$ and $T(n)$ are the measured resonance frequency and temperature at measurement point n and T_{ave} is the average temperature over the actuation period.

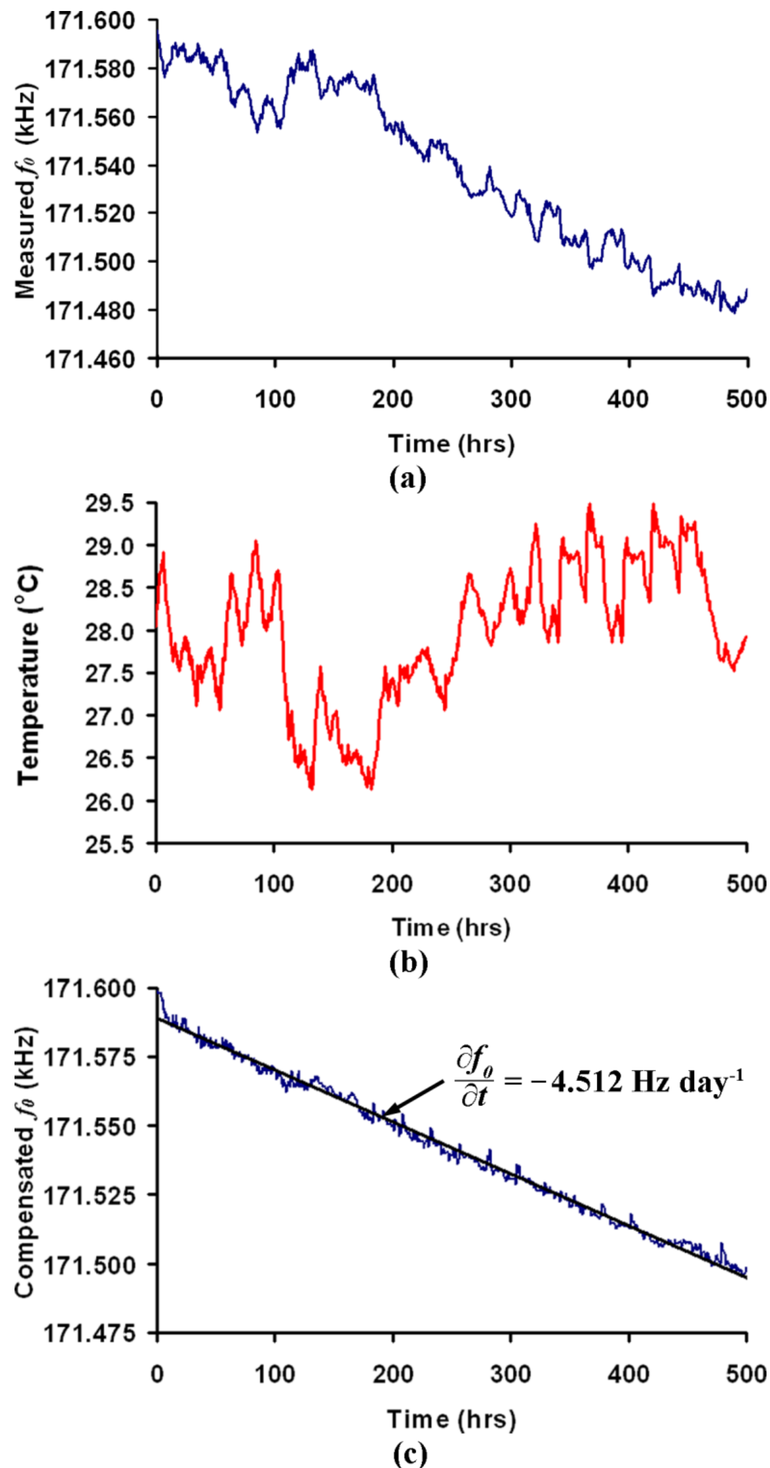

Fig. 5.7. (a) Recorded f_0 of Device R01 over the 500-hour actuation period. The resonance frequency of the device has a substantial dependence on temperature, resulting in large fluctuations in the measured f_0. (b) Measured surface temperature of Device R01. This data was used to decompose the effects of temperature variations on f_0. The average surface temperature over the actuation period was ~27.9 ±1.8 °C. (c) Plot of temperature compensated f_0 after temperature effects have been decomposed. The frequency drift $\partial f_0/\partial t$ of Device R01, obtained using linear line regression, is –4.512 Hz day^{-1}.

The final temperature compensated f_0 readings for Device R01 are shown in Fig. 5.7(c). The average surface temperature over the actuation period was ~27.7 ±1.8 °C. From the temperature compensated frequency plot (Fig. 5.7(c)), the frequency drift $\partial f_0/\partial t$ of Device R01 is determined using linear line regression to be –4.512 Hz day^{-1} over the 500-hour actuation period. This frequency drift value is the first of the three parameters which can be used for assessing resonator long-term stability.

The other two parameters monitored over the actuation period were the Q-factor and peak in-plane displacement of the resonator. Fig. 5.8 shows the Q-factor variation and displacement of Device R01 throughout the actuation period. The displacements are calculated from the recorded phonon voltages using the voltage-displacement gain of 0.0780 mV nm^{-1} (determined using the method detailed in Section 5.3.1).

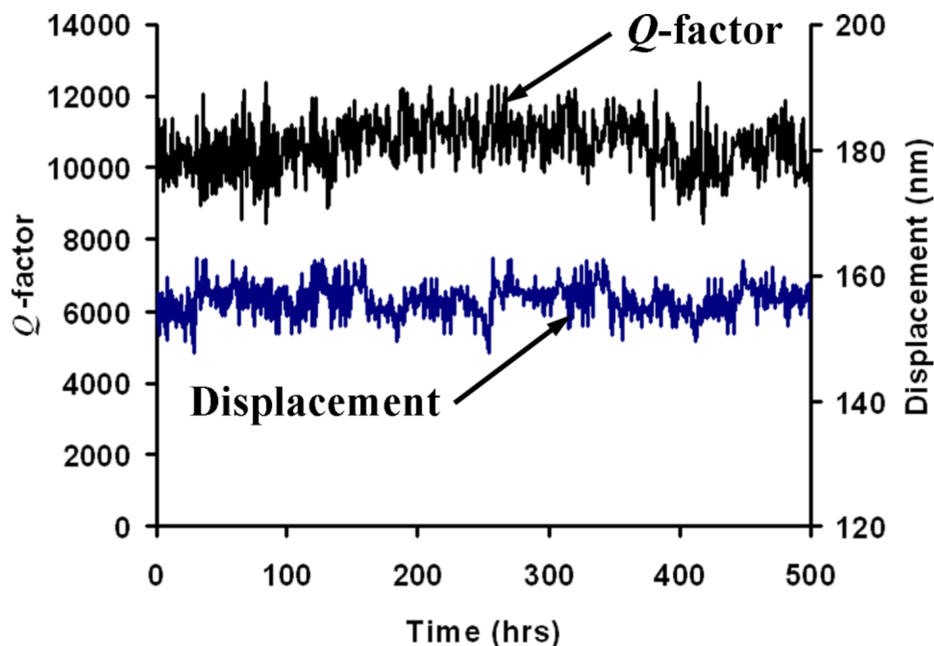

Fig. 5.8. Q-factor variation and in-plane displacement of Device R01 throughout the actuation period. The displacements were derived from the recorded phonon voltages at the resonance frequency f_0 using the voltage-displacement gain of 0.0780 mV nm^{-1}.

A total of fifteen sample devices (designed with L = 400 μm and w = 6 μm) were tested in these long-term stability experiments. The data obtained will be presented in the following section along with discussions on the observed trends in the variation of the three stability parameters.

5.4. Long-term frequency stability measurements for clamped-clamped beam resonators

The measured TC_f and voltage-displacement gain of the fifteen resonators used in these long-term stability experiments, along with their frequency characteristics, are listed in Table 5.2. The fifteen devices were located on four separate dies. Despite being of the same design and fabricated in the same process, the fifteen devices display some disparity in their temperature dependencies, as is evident from their varied TC_f values. However, this disparity is localized to the dies since samples on the same die have roughly the same TC_f and the variation occurs across the different dies.

The fifteen devices were monitored, for a period of 500 hours, in four separate batches with devices on the same die being tested together. They were actuated in their linear mode (V_P = 6.0 V and v_d = 30 mV) at ~28°C and ~10^{-2} Pa. The stability performance of the devices, in terms of their resonance frequency f_0, Q-factor and peak displacement amplitude, during the 500-hour actuation period is discussed below.

Table 5.2. Summary of the fifteen devices used in these long-term stability experiments. The voltage-displacement gain was derived as described in Section 5.3.1.

Die index	Label	f_0 (kHz)	Q-factor	TC_f (ppm °C^{-1})	Voltage-displacement gain (mV nm^{-1})
Die 1	R01	171.588	10,200	–73.87	0.0780
	R02	172.752	16,400	–76.82	0.0455
	R03	172.749	18,100	–80.76	0.0972
	R04	173.423	16,100	–65.95	0.0317
Die 2	R05	172.299	14,100	+49.16	0.0977
	R06	173.368	19,100	+46.77	0.0820
	R07	173.421	15,200	+51.23	0.0924
Die 3	R08	171.036	11,400	–176.38	0.0574
	R09	171.856	20,300	–221.16	0.0851
	R10	171.234	15,800	–158.24	0.0739
	R11	170.845	16,100	–166.51	0.0772
Die 4	R12	170.578	17,300	–101.04	0.0685
	R13	170.868	18,300	–117.42	0.0783
	R14	170.741	18,400	–93.57	0.0428
	R15	171.803	17,800	–105.97	0.0780

5.4.1. Measured frequency stability

The frequency stability of the twelve devices, obtained from their temperature compensated f_0 plots, is summarized in Table 5.3. Overall, the magnitude of the frequency drift displayed by the clamped-clamped beam devices is substantially higher than that of square extensional plate resonators and cantilever resonators [71]. One of the likely causes of this large frequency drift is the clamped-clamped design which tends to induce a fair amount of axial stress on the vibrating beam. The magnitude of this axial stress can be estimated from the TC_f of the device, as discussed previously in Section 5.2.2. From the TC_f measurements and applying Equation (5.9), σ_T for each of the samples at 28 °C (301 K), which is the average ambient temperature during testing, are calculated and summarized in Table 5.3.

Table 5.3. Measured frequency drift $\partial f_0/\partial t$ of the twelve devices compared with the derived axial stress σ_T (calculated using Equation (5.9)) at 28 °C (301 K) on the clamped-clamped beam. The devices are arranged in order of axial stress with positive values denoting tensile stress and negative values denoting compressive stress. [1]The frequency drift of Devices R04 and R13 could not be determined as they displayed large f_0 swings during the actuation period (see Fig. 5.10). Data recording for these two devices was terminated at 120 hours.

Die index	**Label**	**f_0 (kHz)**	**σ_T at 28 °C (MPa)**	**$\frac{\partial f_0}{\partial t}$ (Hz day^{-1})**
Die 2	R07	173.421	6.564	–6.852
	R05	172.299	6.412	–1.138
	R06	173.368	6.235	–3.874
Die 1	[1]R04	173.423	–2.107	-
	R01	171.588	–2.693	–4.812
	R02	172.752	–2.911	–0.9264
	R03	172.749	–3.203	+1.875
Die 4	R14	170.741	–4.151	+4.932
	R12	170.578	–4.704	+6.231
	R15	171.803	–5.069	+11.15
	[1]R13	170.868	–5.916	-
Die 3	R10	171.234	–8.937	+10.53
	R11	170.845	–9.549	+11.89
	R08	171.036	–10.28	+12.66
	R09	171.856	–13.59	+23.48

The calculated tensile and compressive stress for the fifteen devices is in fairly good agreement with results obtained by Miller et al. [106]. In their study of the stress characteristics of the SOIMUMPs process, the average measured axial stress magnitudes on 25 µm-thick test structures was less than 20 MPa. The data in Table 5.3 suggests that, for these clamped-clamped beam devices, resonators whose beam structures are subjected to larger magnitudes of compressive stress, as in the case of Device R08, R09 and R11, tend to display larger positive frequency drift over time and hence have poorer frequency stability. On the other hand, devices which experience tensile axial stress, as in the case of Device R05, R06 and R07, tend to display negative frequency drift.

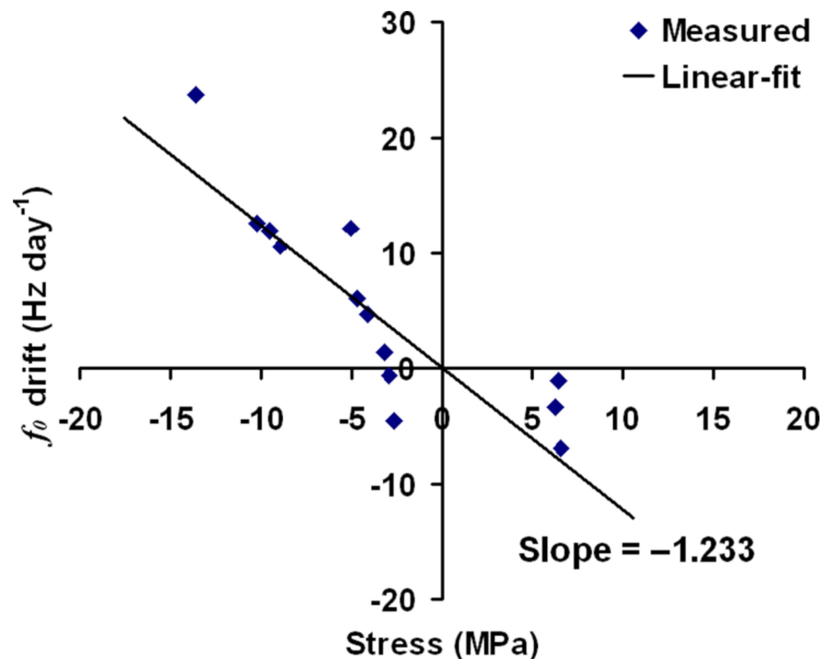

Fig. 5.9. Graphical representation of f_0 drift vs beam axial stress for thirteen of the fifteen test devices (Device R04 and Device R13 were omitted). The slope of the linear-fit line suggests that an f_0 drift of 1.233 Hz day^{-1} is induced for every 1 MPa of stress acting on the clamped-clamped beam.

A graphical representation of the data is shown in Fig. 5.9. Device R04 and Device R13 are omitted from the plot as their frequency stabilities could not be determined since they displayed large f_0 swings during actuation (see Fig 5.10). From the slope of the linear-fit line (obtained using the method of least squares) through the measured data points, it can deduced that an f_0 drift of 1.233 Hz day^{-1} is induced for every 1 MPa of stress acting on the clamped-clamped beams in the devices.

However, the fluctuations in the measured frequency stabilities of Device R01, R02 and R03 (in Table 5.3), whose compressive stress magnitudes are similar but have very different frequency drifts, also indicate the likely presence of other mechanisms which influence the frequency stability of the resonators. One of the possible mechanisms could be the adsorption/desorption of water onto/from the resonator beam, which alters the mass M of the vibrating structure and therefore its resonance frequency (refer to

Equation (5.1)). Although the devices were tested at low pressure in a vacuum chamber, the chamber cannot be considered as an ultra-clean environment and the presence of minute amounts of water vapor is a distinct possibility. This is a fairly reasonable explanation since all three devices were tested together under the same ambient conditions and the presence of water vapor affected all three samples. Experiments by Henry et al. showed that water adsorption can significantly decrease the resonance frequency of silicon paddle resonators over time, even when operating in a vacuum environment [107]. Pierron et al. have also observed a decrease in the resonance frequency of their resonant test structures when operating at higher relative humidity (R.H.) [108]. Hence, the long-term frequency stability of these clamped-clamped beam devices appear to be dependent on the magnitude of axial stress acting on the beam structure, although it is highly likely that axial stress is not the only factor.

Another interesting observation is the deviant frequency behaviour of two of the resonator samples. Fig. 5.10 shows the temperature compensated f_0 variation of Device R13 during actuation (f_0 drift in the first 120 hours is shown and testing was then terminated since device f_0 stability could not be determined). It can be observed that the resonator displayed large frequency swings which appear to be somewhat periodic with a peak-to-peak amplitude of ~100 Hz (the frequency drift hence cannot be determined). A similar phenomenon was observed for Device R04 with less severe swings of ~25 Hz. A check on the recorded characterization curves of both devices over the actuation period showed no signs of the devices displaying non-linear behaviour at the time of the frequency swings. There was also no appreciable degradation in Q-factor of both devices over the actuation period.

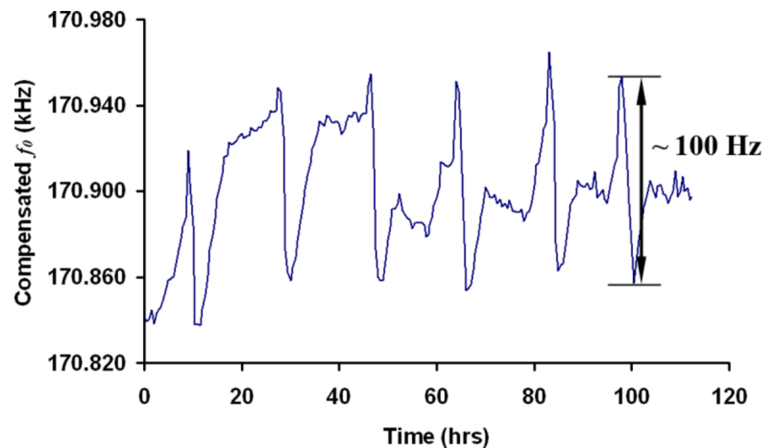

Fig. 5.10. Temperature compensated f_0 variation of Device R13 over the first 120 hours of the actuation period. The device displayed periodic frequency swings of ~100 Hz throughout the actuation period. Compare with Fig. 5.7(c) which shows the compensated f_0 variation for a typical device.

It is unlikely that these frequency swings were caused by environmental factors (e.g. ambient temperature and pressure) as each of the two devices were tested with three others, which did not show frequency swings, in the same vacuum chamber. Considering that the frequency swings in Device R04 and Device R13 were present from the beginning of the experiment, these swings could be a reflection of the poorer initial mechanical state of these two devices in particular, as compared to the other samples, rather than a sign of actuation fatigue.

Overall, this form of long-term device testing is able to provide information on device frequency drift and identify unusual patterns in frequency behaviour, both of which are important for wafer-level screening of devices during manufacturing. For example, the detection of frequency swings in Device R04 and Device R13 during testing would single them out as unsuitable for frequency reference applications which typically have very stringent requirements on frequency stability. From the recorded frequency drift data against beam axial stress, it is also clear that some form of stress-relief structure

would improve the long-term frequency stability of these clamped-clamped beam resonators.

5.4.2. *Q*-factor and peak displacement variation

To analyze the *Q*-factor and displacement fluctuation over time, the standard deviation of the recorded data points for each device was used. Table 5.4 shows the mean and standard deviation of the *Q*-factor and peak in-plane displacement of the fifteen devices over the actuation period. The coefficient of variation *CV* is given by,

$$CV = \frac{s}{\mu} \times 100\% \tag{5.12}$$

where s is the standard deviation and μ is the mean. The *CV* values in Table 5.4 indicate that the *Q*-factor of ten of the devices was relatively stable over the actuation period, deviating by less than 12% from their mean values over 500 hours. This is indicative that high *Q*-factor can be sustained as long as the device operating ambient is maintained at low pressure (10^{-3} – 10^{-2} Pa).

The peak displacements of these resonators were also consistent throughout, varying by less than 10% from the mean values. Data recording for Device R07 and R13 was stopped after 120 hours since the f_0 swings exhibited by both samples may already be an indication of poorer device condition. The *Q*-factor and displacement trends for Device R07, R10 and R14 are somewhat more interesting.

Table 5.4. Mean and standard deviation of the *Q*-factor and peak in-plane displacement of the fifteen devices over the 500-hour actuation period. The coefficient of variation *CV* is calculated using Equation (5.12). [1]Data recording for Device 04 and Device 13 was terminated at 120 hours. [2]Shows data recorded before bifurcation point.

Die index	Label	*Q*-factor			In-plane displacement		
		Mean	Std dev	*CV* (%)	Mean (nm)	Std dev (nm)	*CV* (%)
Die 1	R01	10,524	669	6.36	153	4.72	3.08
	R02	15,212	1,553	10.21	166	13.22	7.98
	R03	17,623	1,965	11.15	156	7.13	4.56
	[1]R04	16,525	1,315	7.96	126	12.18	9.67
Die 2	R05	13,862	927	6.69	163	6.75	4.15
	R06	18,214	1,165	6.40	172	8.22	4.79
	[2]R07	15,233	1,088	7.14	142	4.25	2.99
Die 3	R08	11,675	1,098	9.40	163	13.58	8.34
	R09	18,960	2,102	11.09	161	8.17	5.08
	[2]R10	14,674	1,207	8.23	149	6.11	4.10
	R11	15,392	1,156	7.51	162	8.24	5.09
Die 4	R12	16,431	1,877	11.43	155	10.24	6.60
	[1]R13	17,655	1,401	7.94	151	12.99	8.60
	[2]R14	17,849	1,750	9.80	155	14.66	9.46
	R15	18,810	1,108	5.89	151	12.06	7.98

While the *Q*-factor of Device R07, R10 and R14 was fairly stable initially (as noted in Table 5.4), a notable drop in this parameter was observed at one point during their operating cycles. The *Q*-factor variation for Device R014 is shown in Fig. 5.11. At t = 406 hr, the *Q*-factor stability of the device changes abruptly. The average *Q*-factor before (t < 406 hr) and after (t > 406 hr) the bifurcation point differs by about 3,400 points, which is higher than the standard deviations of the measured data points in both regions. This suggests that the drop in *Q*-factor is indeed resultant from a change in the performance of the sample and not from expected fluctuations or measurement uncertainties. Device R07 and R10 displayed similar drops in their *Q*-factors with bifurcation points at t = 387 hr and t = 321 hr respectively.

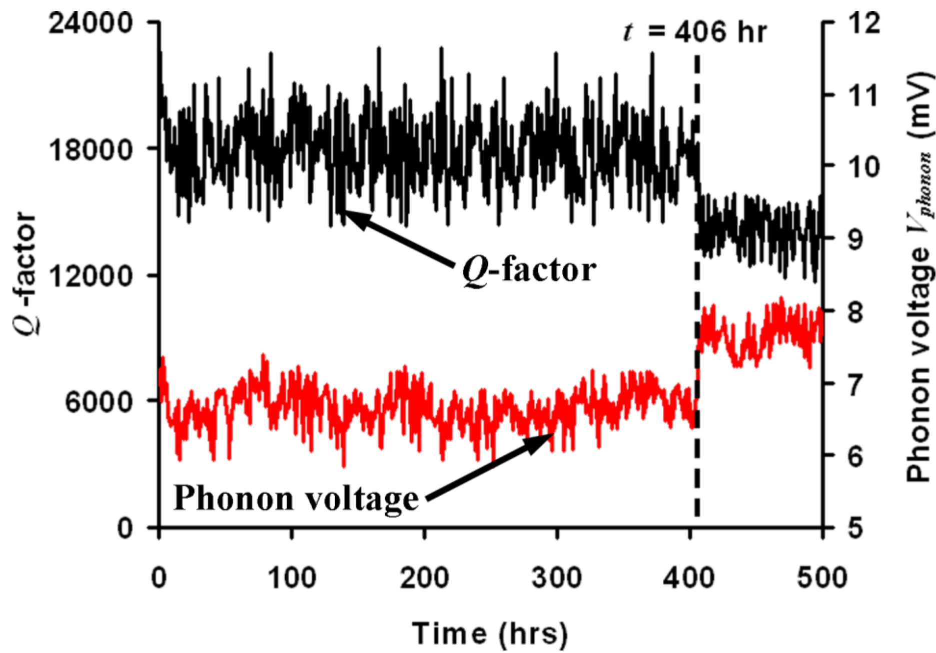

Fig. 5.11. Q-factor variation and phonon voltage V_{phonon} of Device R14 over 500 hours. Note the drop in Q-factor at the bifurcation point t = 406 hr. The concurrent observation of an increase in V_{phonon} prompted a recalibration of the voltage-displacement gain. It was found that the voltage-displacement gain this device increased from 0.0428 mV nm^{-1} to 0.0612 mV nm^{-1} (~43%) after t = 406 hr.

A survey of the average peak phonon voltages V_{phonon} before and after the bifurcation point also reveals some remarkable information. All three devices displayed a marked increase in their average V_{phonon} after the Q-factor drop (see Fig. 5.11). One possible implication of this occurrence is that the phonon transmission properties of the anchor structures in each device have been enhanced. This was confirmed by recalibrating the voltage-displacement gains of the three samples.

Table 5.5. Q-factor, in-plane displacement and voltage-displacement gain of Device R07, R10 and R14 before and after the bifurcation points for each device.

Label	Before bifurcation point			After bifurcation point		
	Voltage-disp. gain (mV nm^{-1})	Ave. Q	Ave. disp. (nm)	Voltage-disp. gain (mV nm^{-1})	Ave. Q	Ave. disp. (nm)
R07	0.0924	15,233	142	0.125	12,490	114
R10	0.0739	14,674	149	0.104	11,592	121
R14	0.0428	17,849	155	0.0612	14,087	125

The *Q*-factor variation, in-plane displacement and the recalibrated gains for the three devices are summarized in Table 5.5. The voltage-displacement gain of each device was determined after the *Q*-factor drop and it was found that the gain for each resonator increased by at least 35%. In effect, the anchors for each of the three devices were dissipating more energy than before which in turn gave rise to a drop in *Q*-factor of ~20%. The twin observations of *Q*-factor drop and corresponding increase in phonon transmission at the anchors is consistent with other studies [8],[86]–[87] which suggest that energy losses at the anchors give rise to *Q*-factor degradation.

The average in-plane displacements (determined using the new voltage-displacement gains) of all three devices also showed a similar decrease after the *Q*-factor drop (see Table 5.5) and showed no signs of increasing or decreasing for the remaining time period. This is to be expected since the electrostatic energy supplied to the samples was the same throughout the actuation period (i.e. the drive voltages remain unchanged) and with an increase in the phonon dissipation at the anchors, there is less energy in the vibrating system to bend the beam structures (i.e. displacement amplitude is reduced). It is worth noting that the reduction in in-plane displacement is less than the rise in voltage-displacement gain and hence the overall effect is still an increase in V_{phonon}. Therefore, by monitoring the magnitude of V_{phonon} alone, it is possible to track changes in the phonon dissipation properties of the resonator anchors over time.

Since the change in phonon dissipation of the three devices occurred after several hundred hours of continuous actuation, it may actually represent a form of fatigue response, i.e. phonon dissipation at the anchor structures of clamped-clamped beam

resonators tends to increase over long-term operation. The root cause of this increase in energy dissipation is difficult to pin-point. It is fairly well-known that surface crack initiation and propagation resulting in fracture is a possible failure mechanism for silicon structures which experience long-term cyclic stress [74]–[77]. However, no cracks were observed at the anchors or anywhere on the surface of the beam structures of the three samples under high resolution SEM imaging. Alternatively, the cyclic stresses during actuation of the samples may have resulted in sub-surface crack formation. Such a fatigue mechanism has been cited as the cause of mechanical failure (i.e. fracture) in LIGA nickel (Ni) [109] thin films used as MEMS structural layers. However, it has been argued that subcritical cracking (or surface wear) does not occur in silicon and that crack growth is initiated in the native oxide (SiO_2) instead (reaction layer fatigue) [74]–[75],[110]. Therefore, the possibility of sub-surface crack initiation occurring within the silicon is remote.

A more likely scenario is the presence of a volume defect at or near the anchor structures of the three devices that has aggravated during long-term actuation. The presence and variability of process-induced defects along the surface and within the volume of silicon structural thin films for MEMS devices is well-known and has often been used to explain the disparity in the material's tensile strength across samples of nominally similar dimensions [106],[111]–[112]. Hence, it is not unreasonable to expect the occurrence of these volume defects within the clamped-clamped beams. Defect growth near the anchors enhances the stress concentration (higher stress fields) in the region [113] which in turn raises its phonon dissipation properties. This would

therefore explain the observation of increased phonon dissipation at the anchors of the test structures during long-term operation.

The collection of data obtained by the test system allows analysis of the long-term performance of the devices in three key aspects: frequency stability, Q-factor stability and peak displacement. Aside from measuring the actual frequency drift of the devices the test system is also able to detect unusual patterns in the frequency stability of the resonators. The consistency of the Q-factor and the actuation amplitude (peak displacement) can also be derived from the data collected. All these information are important for filtering out devices which do not meet specifications for application in a manufacturing scenario. In addition, the change in the energy dissipation properties of the resonators is a mechanical characteristic which cannot be detected using state-of-the-art electrical testing techniques. This highlights the unique advantage that the phonon detection technique possesses for long-term testing of resonator devices. By monitoring the phonon voltage it is possible to identify various instances in the operating cycle where the mechanical condition of the anchor structures has changed. This in turn may be an indication of device fatigue.

5.5. Conclusions

An automated phonon detection test setup for monitoring the long-term stability of micromechanical resonators has been presented in this chapter. The key advantages of phonon detection are its ability to detect the motion of multiple devices with minimal use of electronics and the capability of sensing mechanical changes in the samples over long-term operation. The test setup was used to investigate the long-term stability of

fifteen identical comb actuated clamped-clamped beam resonators fabricated using the SOIMUMPS process. It was determined that one of the factors affecting the long-term frequency stability of these clamped-clamped beam devices is the magnitude of axial stress acting on the beam structure. Larger magnitudes of axial stress tend to result in higher frequency shift and poorer frequency stability in the resonators. From the measurements, it was established that an f_0 drift of 1.233 Hz day^{-1} was induced in these samples for every 1 MPa of axial stress on the beam structure. The Q-factors of most of the devices were relatively stable over the actuation period, deviating by less than 12% from the mean values over 500 hours. The peak displacements of the resonators were also fairly consistent throughout, varying by less than 10% from the mean values. Of the fifteen devices, three resonators showed possible signs of fatigue behaviour when the phonon dissipation properties of their anchor structures were enhanced after several hundred hours of operation. The enhanced dissipation gave rise to a 35% – 41% increase in the magnitude of the phonon voltage generated per nm of resonator displacement and also to a ~20% drop in the Q-factors of the three resonators. This enhanced dissipation may be attributed to the growth of existing volume defects within the silicon beam structures. The energy dissipation is a mechanical characteristic which cannot be detected using state-of-the-art electrical testing methods, highlighting the unique advantage the phonon detection technique possesses for long-term testing of resonator devices. By monitoring the phonon voltage it is possible to identify various instances in the operating cycle where the mechanical condition of the structures has changed.

CHAPTER 6

CONCLUSION

6.1. Conclusion

An acoustic phonon detection technique that can be applied for motion characterization of dynamic MEMS devices has been developed. Motion detection is achieved by utilizing a piezoelectric transducer to sense the mechanical waves or phonons generated during the surface interaction or energy dissipation which occurs during device actuation. On top of being able to provide similar information on the short-term performance parameters of MEMS devices as more established electrical characterization techniques, phonon detection also offers additional insight into the mechanical state of the devices. This particular attribute is unique to the technique and it is a capability which will be especially useful for assessing the long-term performance of MEMS devices. The reason for this is because the wear and tear that occurs during long-term device actuation invariably alters the mechanical state, a

property that cannot be assessed by imaging methods or electrical measurements. Both the hardware and software components for an automated phonon detection test system for MEMS devices have been established. With regards to sensitivity, the current setup is able to sense the vibration of state-of-the-art clamped-clamped beam resonators with less than 100 nm peak displacement at resonance.

To facilitate motion calibration for subsequent experiments, a high-resolution stroboscopic SEM technique for directly measuring the in-plane physical displacement of dynamic MEMS devices with nanoscale accuracy has also been introduced. Stroboscopy was achieved by time-gated sampling of the SEM secondary electron (SE) signal. By varying the phase delay of the gate signal, the instantaneous displacement of the device at various phases of its motion can be captured. The technique can further be applied to obtain a phase-resolved image of the motion of the device-under-test (DUT) during actuation by ramping the phase delay of the gate signal while imaging. This capability is particularly handy should one require a graphic visualization of the DUT motion, something which cannot be provided by optical imaging techniques that typically utilize blur synthesis for motion measurement. The current hardware implementation can achieve a displacement resolution of about 20 nm, limited mainly by the electron probe size, for motion frequencies up to 3.58 MHz. Further optimization can potentially allow the system to provide sub-10 nm imaging resolution.

The phonon detection test setup was applied to study the long-term performance of micromechanical comb actuated clamped-clamped beam resonators. Resonator devices were selected as the subject of study due to their potential as a commercially viable

product. From the test results on fifteen identical resonators, obtained over 500 hours of actuation for each device, it was determined that one of the factors affecting the long-term frequency stability of the clamped-clamped beam devices is the magnitude of axial stress acting on the beam structure. Larger magnitudes of axial stress tend to result in higher frequency shift and poorer frequency stability in the resonators. From the measurements, it was established that an f_0 drift of 1.233 Hz day^{-1} was induced in the samples for every 1 MPa of axial stress on the beam structure. The Q-factor and peak displacement of most of the samples remained fairly consistent throughout varying by less than 12% and 10% from their mean values respectively. Of the fifteen devices, three resonators showed possible signs of fatigue behaviour when the phonon dissipation properties of their anchor structures were enhanced after several hundred hours of operation. The enhanced dissipation gave rise to a 35% – 41% increase in the magnitude of the phonon voltage generated per nm of resonator displacement and also to a ~20% drop in the Q-factors of the three resonators. Previous reported studies on the long-term stability of micromechanical resonators, which were carried out using state-of-the-art electrical measurement methods, have not been able to identify any such signs of fatigue in devices. The energy dissipation is a mechanical characteristic which cannot be detected using electrical testing, highlighting the unique advantage the phonon detection technique possesses for long-term testing of resonator devices. By monitoring the phonon voltage it is possible to identify various instances in the operating cycle where the mechanical condition of the structures has changed.

6.2. Recommendations for future work

Future work on phonon detection can proceed on two fronts. The first is to extend the long-term testing capability of the technique to other MEMS structures, most notably contact-mode devices such as switches or micromirrors. The current results on resonator testing have essentially demonstrated the feasibility of phonon detection in identifying variations in the mechanical state (more specifically changes in the anchor dissipation) of the samples over time. Contact-mode devices are even more likely to experience wear and tear since their operation typically involves surface-to-surface interactions and hence it appears fitting that phonon detection be applied in the testing of these devices as well. Analysis of the phonon signal generated can potentially provide information on the intrinsic properties of the test structure, such as its natural resonance frequency, and also on the tribological properties of the contact surfaces. Once more, these are parameters which cannot be measured by electrical screen tests which are currently widely used for MEMS device testing.

The second is to further the long-term tests which have been presented in this work. The data obtained from the clamped-clamped beam resonators has revealed a possible form of fatigue behaviour which can eventually give rise to a failure mode. Some form of accelerated testing procedure would be necessary to induce the occurrence of the failure mode within a reasonable time period. Developing such a procedure would be a worthwhile endeavor as it can serve as a stepping stone to establishing a kind of 'burn-in' test for resonator manufacturers to screen out infant mortality failures. Accelerated aging techniques that are commonly applied for materials testing involve the application of elevated temperature, humidity and mechanical stress during testing.

However, selection of an appropriate method for the resonator structures should take into consideration their observed fatigue behaviour (i.e. enhanced anchor dissipation) and possible failure mechanism.

REFERENCES

[1] Y.-H. Cho, J.S. Ko, K. Lee, B.M. Kwak, K. Park and K.H. Kim, A skew-symmetric cantilever accelerometer for automotive airbag applications, Sens. Actuators A 50 (1995) 121–126.

[2] J. Valldorf and W. Gessner (eds.), Advanced Microsystems for Automotive Applications 2006, Springer, New York, 2006.

[3] J.-H. Park, H.-C. Lee, Y.-H. Park, Y.-D. Kim, C.-H. Ji, J. Bu and H.-J. Nam, A fully wafer-level packaged RF MEMS switch with low actuation voltage using a piezoelectric actuator, J. Micromech. Microeng. 16 (2006) 2281–2286.

[4] A. Yongchul, H. Guckel and J.D. Zook, Capacitive microbeam resonator design, J. Micromech. Microeng. 11 (2001) 70–80.

[5] H. Chandrahalim, D. Weinstein, L.F. Cheow and S.A. Bhave, High-κ dielectrically transduced MEMS thickness shear mode resonators and tunable channel-select RF filters, Sens. Actuators A 136 (2007) 527–539.

[6] Global MEMS/Microsystems – Markets and Opportunities, Yole Développement, 18 May 2010, http://www.yole.fr/pagesan/products/semi.asp.

[7] R. Lifshitz and M.L. Roukes, Thermoelastic damping in micro- and nanomechanical systems, Phys. Rev. B 61 (2000) 5600–5609.

[8] J. Yang, T. Ono and M. Esashi, Energy dissipation in submicrometer thick single-crystal silicon cantilevers, J. Microelectromech. Syst. 11 (2002) 775–783.

[9] D.A. Czaplewski, J.P. Sullivan, T.A. Friedmann, D. W. Carr, B.E.N. Keeler and J.R. Wendt, Mechanical dissipation in tetrahedral amorphous carbon, J. Appl. Phys. 97 (2005) 023517.

[10] K.Y. Yasumura, T.D. Stowe, E.M. Chow, T. Pfafman, T.W. Kenny, B.C. Stipe and D. Rugar, Quality factors in micron- and submicron-thick cantilevers, J. Microelectromech. Syst. 9 (2000) 117–125.

[11] M. Domnik and L.J. Balk, Quantitative scanning electron acoustic microscopy of silicon, Scanning Microsc. 7 (1993) 37–48.

[12] W.K. Wong, E.I. Rau and J.T.L. Thong, Electron-acoustic and surface electron beam induced voltage signal formation in scanning electron microscopy analysis of semiconducting samples, Ultramicroscopy 101 (2004) 183–195.

[13] A. Yongchul, H. Guckel and J.D. Zook, Capacitive microbeam resonator design, J. Micromech. Microeng. 11 (2001) 70–80.

[14] S. Pourkamali, R. Abdolvand, G.K. Ho and F. Ayazi, Electrostatically coupled micromechanical beam filters, in: Proceedings of the 17th IEEE International Conference on Micro Electro Mechanical Systems, Maastricht, Netherlands, Jan 25–Jan 29, 2004, pp. 584–587.

[15] D.S. Greywall, Sensitive magnetometer incorporating a high-Q nonlinear mechanical resonator, Meas. Sci. Technol. 16 (2005) 2473–2482.

[16] R.M.C. Mestrom, R.H.B. Fey, J.T.M. van Beek, K.L. Phan and H. Nijmeijer, Modeling the dynamics of a MEMS resonator: simulations and experiments, Sens. Actuators A 142 (2008) 306–315.

[17] J. Wylde and T.J. Hubbard, Measurement of MEMS displacements and frequencies using laser interferometry, in: Proceedings of the IEEE Canadian Conference on Electrical and Computer Engineering, Edmonton, Alberta, Canada, May 9–May 12, 1999, pp. 1680–1685.

[18] J.-M. Huang, A.Q. Liu, C. Lu and J. Ahn, Mechanical characterization of micromachined capacitive switches: design consideration and experimental verification, Sens. Actuators A 108 (2003) 36–48.

[19] J.A. Conway, J.V. Osborn and J.D. Fowler, Stroboscopic imaging interferometer for MEMS performance measurement, J. Microelectromech. Syst. 16 (2007) 668–674.

[20] M.R. Hart, R.A. Conant, K.Y. Lau and R.S. Muller, Stroboscopic interferometer system for dynamic MEMS characterization, J. Microelectromech. Syst. 9 (2000) 409–418.

[21] C. Rembe and R.S. Muller, Measurement system for full three-dimensional motion characterization of MEMS, J. Microelectromech. Syst. 11 (2002) 479–488.

[22] S. Petitgrand and A. Bosseboeuf, Simultaneous mapping of out-of-plane and in-plane vibrations of MEMS with (sub)nanometer resolution, J. Micromech. Microeng. 14 (2004) 97–101.

[23] P. Castellini, M. Martarelli and E.P. Tomasini, Laser Doppler Vibrometry: Development of advanced solutions answering to technology's needs, Mech. Syst. Signal Pr. 20 (2006) 1265–1285.

[24] J.S. Burdess, A.J. Harris, D. Wood, R.J. Pitcher and D. Glennie, A system for the dynamic characterization of microstructures, J. Microelectromech. Syst. 6 (1997) 322–328.

[25] E. Ferraris, I. Fassi, B.D. Masi, R. Rosing and A. Richardson, A capacitance and optical method for the static and dynamic characterization of micro electro mechanical systems (MEMS) devices, Microsyst. Technol. 12 (2006) 1053–1061.

[26] J.F. Vignol, X. Liu, S.F. Morse, B.H. Houston, J.A. Bucaro, M.H. Marcus, D. M. Photiadis and L. Sekaric, Characterization of silicon micro-oscillators by scanning laser vibrometry, Rev. Sci. Instrum. 73 (2002) 3584–3588.

[27] C. Rembe and Alexander Dräbenstedt, Laser-scanning confocal vibrometer microscope: Theory and experiments, Rev. Sci. Instrum. 77 (2006) 083702.

[28] B. Serio, J.J. Hunsinger and B. Cretin, In-plane measurements of microelectromechanical systems vibrations with nanometer resolution using the correlation of synchronous images, Rev. Sci. Instrum. 75 (2004) 3335–3341.

[29] K. Krupa, M. Józwik, C. Gorecki, A. Andrei, Ł. Nieradko, P. Delobelle and L. Hirsinger, Static and dynamic characterization of AlN-driven microcantilevers using optical interference microscopy, Opt. Laser Eng. 47 (2009) 211–216.

[30] C. Furlong, A.M. Siegel, P. Hefti and R.J. Pryputniewicz, Confocal optoelectronic holography microscope for materials and structural characterization of MEMS, in: Proceedings of the 12th International Conference on Solid-State Sensors, Actuators and Microsystems, Boston, MA, USA, Jun 8–Jun 12, 2003, pp. 420–423.

[31] D.M. Freeman, Measuring Motions of MEMS, MRS Bull. 4 (2001) 305–306.

[32] N.F. Smith, D.M. Tanner, S.E. Swanson and S.L. Miller, Non-destructive resonant frequency measurement on MEMS actuators, in: Proceedings of the 39th IEEE International Reliability Physics Symposium, Orlando, FL, USA, Apr 30–May 3, 2001, pp. 99–105.

[33] C.Q. Davis and D.M. Freeman, Using a light microscope to measure motions with nanometer accuracy, Opt. Eng. 37 (1998) 1299–1304.

[34] C. Rembe, B. Tibken and E.P. Hofer, Analysis of the dynamics in microactuators using high-speed cine photomicrography, J. Microelectromech. Syst. 10 (2001) 137–145.

[35] S. Roy, R.G. DeAnna, C.A. Zorman and M. Mehregany, Fabrication and characterization of polycrystalline SiC resonators, IEEE Trans. Electron Devices 49 (2002) 2323–2332.

[36] W.T. Pike and I.M. Standley, Determination of the dynamics of micromachined lateral suspensions in the scanning electron microscope, J. Micromech. Microeng. 15 (2005) S82–S88.

[37] I. Ogo and N.C. MacDonald, Application of time-resolved scanning electron microscopy to the analysis of the motion of micromechanical structures, J. Vac. Sci. Technol. B 14 (1996) 1630–1634.

[38] J.P. Gilles, S. Megherbi, G. Raynaud, F. Parrain, H. Mathias, X. Leroux and A. Bosseboeuf, Scanning electron microscopy for vacuum quality factor measurement of small-size MEMS resonators, Sens. Actuators A 145–146 (2008) 187–193.

[39] M. Zalalutdinov, B. Ilic, D. Czaplewski, A. Zehnder, H.G. Craighead and J.M. Parpia, Frequency-tunable micromechanical oscillator, Appl. Phys. Lett. 77 (2000) 3287–3289.

[40] H. Ashiba, S. Warisawa and S. Ishihara, Evaluation method of the quality factor of micromechanical resonators using electron beams, Jpn. J. Appl. Phys. 48 (2009) 06FG08.

[41] A.A. Trusov and A.M. Shkel, Capacitive detection in resonant MEMS with arbitrary amplitude of motion, J. Micromech. Microeng. 17 (2007) 1583–1592.

[42] W.C. Tang, T.-C.H. Nguyen, M.W. Judy and R.T. Howe, Electrostatic-comb drive of lateral polysilicon resonators, Sens. Actuators A21–A23 (1990) 328–331.

[43] C.T.-C. Nguyen and R.T. Howe, An Integrated CMOS micromechanical resonator high-Q oscillator, IEEE J. Solid-St. Circ. 34 (1999) 440–455.

[44] P. Bruschi, A. Nannini and F. Pieri, Electrical measurements of the quality factor of microresonators and its dependence on the pressure, Sens. Actuators A 114 (2004) 21–29.

[45] T.H. Lee, The design of CMOS radio-frequency integrated circuits, Cambridge University Press, U.K., 1998.

[46] J.R. Clark, W.-T. Hsu and C.T.-C. Nguyen, Measurement techniques for capacitively-transduced VHF-to-UHF micromechanical resonators, in: Proceedings of the 11th International Conference on Solid-state Sensors and Actuators, Munich, Germany, Jun 10–Jun 14, 2001, pp. 1118–1121.

[47] Discera Inc., 18 May 2010, http://www.discera.com/.

[48] SiTime, 18 May 2010, http://www.sitime.com/.

[49] Silicon Clocks, 18 May 2010, http://www.siliconclocks.com/.

[50] F.D. Bannon III, J.R. Clark, and C.T.-C. Nguyen, High-Q HF microelectromechanical filters, IEEE J. Solid-St. Circ. 35 (2000) 512–526.

[51] D.J. Young, İ.E. Pehlivanoğlu and C.A. Zorman, Silicon carbide MEMS-resonator-based oscillator, J. Micromech. Microeng. 19 (2009) 115027.

[52] V. Kaajakari, T. Mattila, A. Oja, J. Kiihamäki and H. Seppä, Square-extensional mode single-crystal silicon micromechanical resonator for low-phase-noise oscillator applications, IEEE Electr. Device L. 25 (2004) 173–175.

[53] J.E.-Y. Lee, B. Bahreyni, Y. Zhu and A.A. Seshia, A single-crystal-silicon bulk-acoustic-mode microresonator oscillator, IEEE Electr. Device L. 29 (2008) 701–703.

[54] M.A. Abdelmoneum, M.U. Demirci and C.T.-C. Nguyen, Stemless wine glass-mode disk micromechanical resonators, in: Proceedings of the 16th IEEE Intnternational Conference on Micro-Electro-Mechanical Systems, Kyoto, Japan, Jan 19–Jan 23, 2003, pp. 698–701.

[55] Y.-W. Lin, S. Lee, S.-S. Li, Y. Xie, Z. Ren and C.T.-C. Nguyen, Series-resonant VHF micromechanical resonator reference oscillators, IEEE J. Solid-St. Circ. 39 (2004) 2477–2491.

[56] M. Akgul, B. Kim, L.-W. Hung, Y. Lin, W.-C. Li, W.-L. Huang, I. Gurin, A. Borna and C.T.-C. Nguyen, Oscillator far-from-carrier phase noise reduction via nano-scale gap tuning of micromechanical resonators, in: Proceedings of the 15th International Conference on Solid-state Sensors, Actuators and Microsystems, Denver, CO, USA, Jun 21–Jun 25, 2009, pp. 798–801.

[57] D. Paci, M. Mastrangeli, A. Nannini and F. Pieri, Modeling and characterization of three kinds of MEMS resonators fabricated with a thick polysilicon technology, Analog Integr. Circ. Sig. Process. 48 (2006) 41–47.

[58] H H. Kahn, M.A. Huff and A.H. Heuer, Heating effects on the Young's modulus of films sputtered onto micromachined resonators, in: Proceedings of the Materials Research Society Symposium, San Francisco, CA, Apr 13–Apr 17, 1998, pp. 33–38.

[59] J.-H. Chae, J.-Y. Lee and S.-W. Kang, Measurement of thermal expansion coefficient of poly-Si using microgauge sensors, Sens. Actuators 75 (1999) 222–229.

[60] H. Tada, A.E. Kumpel, R.E. Lathrop, J.B. Slanina, P. Nieva, P. Zavracky, I.N. Miaoulis and P.Y. Wong, Thermal expansion coefficient of polycrystalline silicon and silicon dioxide thin films at high temperatures, J. Appl. Phys. 87 (2000) 4189–4193.

[61] R. Melamud, M. Hopcroft, C. Jha, B. Kim, S. Chandorkar, R. Candler and T.W. Kenny, Effects of stress on the temperature coefficient of frequency in double clamped resonators, in: Proceedings of the 13th International Conference on Solid-state Sensors, Actuators and Microsystems, Seoul, Korea, Jun 5–Jun 9, 2005, pp. 392–395.

[62] T. Roessig, Integrated MEMS tuning fork oscillators for sensor applications, PhD Dissertation, University of California, Berkeley, 1998.

[63] K. Wang, A.-C. Wong and C.T.-C. Nguyen, VHF free-free beam high-Q micromechanical resonators, J. Microelectromech. Syst. 9 (2000) 347–360.

[64] W.-T. Hsu, J.R. Clark and C.T.-C. Nguyen, A resonant temperature sensor based on electrical spring softening, in: Proceedings of the 11th International Conference on Solid-state Sensors and Actuators, Munich, Germany, Jun 10–Jun 14, 2001, pp. 1484–1487.

[65] K. Sundaresan, G.K. Ho, S. Pourkamali and F. Ayazi, A two-chip, 4-MHz, microelectromechanical reference oscillator, in: Technical Digest IEEE International Symposium on Circuits and Systems, Kobe, Japan, May 23–May 26, 2005, pp. 5461– 5464.

[66] W.-T. Hsu, J.R. Clark and C.T.-C. Nguyen, Mechanically temperature-compensated flexural-mode micromechanical resonators, in: Technical Digest IEEE International Electron Devices Meeting, San Francisco, California, Dec 11–Dec 13, 2000, pp. 399–402.

[67] W.-T. Hsu and C.T.-C. Nguyen, Stiffness-compensated temperature-insensitive micromechanical resonators, in: Technical Digest IEEE International Micro Electro Mechanical Systems Conference, Las Vegas, Nevada, Jan 20–Jan 24, 2002, pp. 731–734.

[68] G.K. Ho, K. Sundaresan, S. Pourkamali and F. Ayazi, Temperature compensated IBAR reference oscillators, in: Technical Digest IEEE International Micro Electro Mechanical Systems Conference, Istanbul, Turkey, Jan 22–Jan 26, 2006, pp. 910–913.

[69] K. Sundaresan, G.K. Ho, S. Pourkamali and F. Ayazi, Electronically temperature compensated silicon bulk acoustic resonator reference oscillators, IEEE J. Solid-st. Circ. 42 (2007) 1425–1434.

[70] M. Koskenvuori, T. Mattila, A. Häärä, J. Kiihamäki, I. Tittonen, A. Oja and H. Seppä, Long-term stability of single-crystal silicon microresonators, Sens. Actuators A 115 (2004) 23–27.

[71] V. Kaajakari, J. Kiiham, A. Oja, S. Pietik, V. Kokkala and H. Kuisma, Stability of wafer level vacuum encapsulated single-crystal silicon resonators, Sens. Actuators A 130–131 (2006) 42–47.

[72] B. Kim, R.N. Candler, M.A. Hopcroft, M. Agarwal, W.-T. Park and T.W. Kenny, Frequency stability of wafer-scale film encapsulated silicon based MEMS resonators, Sens. Actuators A 136 (2007) 125–131.

[73] D.M. Tanner, R.H. Olsson III, T.B. Parson, S.M. Crouch, J.A. Walraven and J.A. Ohlhausen, Stability experiments on MEMS aluminum nitride RF resonators, Proc. SPIE 7592 (2010) 759209.

[74] C.L. Muhlstein, R.T. Howe and R.O. Ritchie, Fatigue of polycrystalline silicon for microelectromechanical system applications: crack growth and stability under resonant loading conditions, Mech. Mater. 36 (2004) 13–33.

[75] C.L. Muhlstein, Characterization of structural films using microelectromechanical resonators, Fatigue Fract. Engng. Mater. Struct. 28 (2005) 711–721.

[76] H. Kahn, N. Tayebi, R. Ballarini, R.L. Mullen and A.H. Heuer, Fracture toughness of polysilicon MEMS devices, Sens. Actuators 82 (2000) 274–280.

[77] H. Kahn, R. Ballarini and A.H. Heuer, Dynamic fatigue of silicon, Curr. Opin. Solid St. M 8 (2004) 71–76.

[78] J. Bagdahn and W.N. Sharpe Jr., Fatigue of polycrystalline silicon under long-term cyclic loading, Sens. Actuators A 103 (2003) 9–15.

[79] D.H. Alsem, O.N. Pierron, E.A. Stach, C.L. Muhlstein and R.O. Ritchie, Mechanisms for fatigue of micron-scale silicon structural films, Adv. Eng. Mater. 9 (2007) 15–30.

[80] C.L. Muhlstein, E.A. Stach and R.O. Ritchie, A reaction-layer mechanism for the delayed failure of micron-scale polycrystalline silicon structural films subjected to high-cycle fatigue loading, Acta Mater. 50 (2002) 3579–3595.

[81] J.L. Davis, Wave propagation in solids and fluids, Springer-Verlag, New York, 1988.

[82] R.A. Coutu Jr., P.E. Kladitis, K.D. Leedy and R.L. Crane, Selecting metal alloy electric contact materials for MEMS switches, J. Micromech. Microeng. 14 (2004) 1157–1164.

[83] T. Corman, P. Enoksson and G. Stemme, Gas damping of electrostatically excited resonators, *Sens. Actuators* A 61 (1997) 249–255.

[84] R.N. Candler, A. Duwel, M. Varghese, S.A. Chandorkar, M.A. Hopcroft, W.-T. Park, B. Kim, G. Yama, A. Partridge, M. Lutz and T. W. Kenny, Impact of geometry on thermoelastic dissipation in micromechanical resonant beams, J. Microelectromech. Syst. 15 (2006) 927–934.

[85] K.Y. Yasumura, T.D. Stowe, E.M. Chow, T. Pfafman, T.W. Kenny, B.C. Stipe and D. Rugar, Quality factors in micron- and submicron-thick cantilevers, J. Microelectromech. Syst. 9 (2000) 117–125.

[86] M.C. Cross and R. Lifshitz, Elastic wave transmission at an abrupt junction in a thin plate with application to heat transport and vibrations in mesoscopic systems, Phys. Rev. B 64 (2001) 085324.

[87] Y.-H. Park and K.C. Park, High-fidelity modeling of MEMS resonators – Part 1: Anchor loss mechanisms through substrate, J. Microelectromech. Syst. 13 (2004) 248–257.

[88] R.S.O. Moheimani and A.J. Fleming, Piezoelectric transducers for vibration control and damping, Springer, London, 2006.

[89] Physical and piezoelectric properties of APCI materials, APC International Ltd., 18 May 2010, http://www.americanpiezo.com/materials/apc_properties.html.

[90] F. Dauchy and R.A. Dorey, Thickness mode high frequency MEMS piezoelectric micro ultrasound transducers, J. Electroceram. 19 (2007) 383–386.

[91] M.J. Crocker (ed.), Handbook of acoustics, John Wiley and Sons, New York, 1998.

[92] H. Ishikawa, H. Dobashi, T. Kodama, T. Furuhashi and Y. Uchikawa, Investigation of micro mechanical vibration of piezoelectric actuators using a stroboscopic SEM, J. Electron Microsc. 42 (1993) 35–40.

[93] H. Fujioka, K. Nakamae and K. Ura, Function Testing of Bipolar ICs and LSIs with the stroboscopic scanning electron microscope, IEEE J. Solid-state Circuits SC-15 (1980) 177–183.

[94] E. Mivehchi, P. Beckley, D.H. Horrocks and C.H. Porter, Stroboscopic observation of domain motion on coated Si-Fe sheet using scanning electron microscope, IEEE Trans. Magn. 26 (1990) 1975–1977.

[95] I. Varga, L. Pogany, C. Hargitai and I. Bakonyi, Extracting domain wall patterns from SEM magnetic contrast images, J. Magn. Magn. Mater. 302 (2006) 405–412.

[96] M. Gesley, An electron optical theory of beam blanking, Rev. Sci. Instrum. 64 (1993) 3169–3190.

[97] J.I. Goldstein, D.E. Newbury, P. Echlin, D.C. Joy, A.D. Romig, Jr., C.E. Lyman, C. Fiori and E. Lifshin, Scanning electron microscopy and X-ray microanalysis, Plenum Press, New York, 1992, p. 177.

[98] W. Tang, T. Nguyen and R. Howe, Laterally driven polysilicon resonant microstructures, Sens. Actuators A 20 (1989) 25–32.

[99] A.A. Seshia, M. Palaniapan, T.A. Roessig, R.T. Howe, R.W. Gooch, T.R. Schimert and S. Montague, A vacuum packaged surface micromachined resonant accelerometer, J. Microelectromech. Syst. 11 (2002) 784–793.

[100] H. Fujioka, K. Nakamae and K. Ura, Signal-to-noise ratio in the stroboscopic scanning electron microscope, J. Phys. E: Sci. Instrum. 18 (1985) 598–603.

[101] C.T.-C. Nguyen, Micromechanical resonators for oscillators and filters, in: Proceedings of the 1995 IEEE Ultrasonics Symposium, Seattle, WA, USA, Nov 7–Nov 10, 1995, pp. 489–99.

[102] L.W. Lin, R.T. Howe and A.P. Pisano, Microelectromechanical filters for signal processing, J. Microelectromech. Syst. 7 (1998) 286–94.

[103] T. Mattila, O. Jaakkola, J. Kiihamäki, J. Karttunen, T. Lamminmäki, P. Rantakari, A. Oja, H. Seppä, H. Kattelus and I. Tittonen, 14 MHz micromechanical oscillator, Sens. Actuators A 97–98 (2002) 497–502.

[104] K. Miller, A. Cowen A, G. Hames and B. Hardy, SOIMUMPs design handbook, MEMSCAP, Paris, 2004.

[105] D.J. Gorman, Free vibration analysis of beams and shafts, John Wiley and Sons, New York, 1972.

[106] D.C. Miller, B.L. Boyce, M.T. Dugger, T.E. Bunchheit and K Gall, Characteristics of a commercially available silicon-on-insulator MEMS material, Sens. Actuators A 138 (2007) 130–144.

[107] J.A. Henry, Y. Wang and M.A. Hines, Controlling energy dissipation and stability of micromechanical silicon resonators with self-assembled monolayers, Appl. Phys. Lett. 84 (2004) 1765–1767.

[108] O.N. Pierron, C.C. Abnet and C.L. Muhlstein, Methodology for low- and high-cycle fatigue characterization with kHz-frequency resonators, Sens. Actuators A 128 (2006) 140–50.

[109] Y. Yang, B.I. Imasogie, S.M. Allameh, B. Boyceb, K. Lian, J. Loua and W.O. Soboyejo, Mechanisms of fatigue in LIGA Ni MEMS thin films, Mat. Sci Eng. A 444 (2007) 39–50.

[110] D.H. Alsem, M.T. Dugger, E.A. Stach and R.O. Ritchie, Micron-scale friction and sliding wear of polycrystalline silicon thin structural films in ambient air, J. Microelectromech. Syst. 17 (2008) 1144–1154.

[111] D.A. Lavan, B.L. Boyce and T.E. Buchheit, Size and frequency of defects in silicon MEMS, Int. J. Damage Mech. 12 (2003) 357–363.

[112] B.L. Boyce, J.M. Grazier, T.E. Buchheit and M.J. Shaw, Strength distributions in polycrystalline silicon MEMS, J. Microelectromech. Syst. 16 (2007) 179–190.

[113] J. Bagdahn, W.N. Sharpe Jr. and O. Jadaan, Fracture strength of polysilicon at stress concentrations, J. Microelectromech. Syst. 12 (2003) 302–312.

LIST OF PUBLICATIONS

Journal publications

1. **C.-L. Wong** and W.-K. Wong, In-plane motion characterization of MEMS resonators using stroboscopic scanning electron microscopy, Sensors and Actuators A 138 (2007) 167–178.

2. L.C. Shao, **C.-L. Wong**, M. Palaniapan and W.K. Wong, Study of nonlinearities in micromechanical clamped-clamped beam resonators using stroboscopic SEM, Journal of Micromechanics and Microengineering 18 (2008) Art. no. 085019.

3. **C.-L. Wong** and M. Palaniapan, Phonon detection technique for the study of temperature coefficient of resonance frequency in clamped-clamped beam resonators, Journal of Micromechanics and Microengineering 19 (2009) Art. no. 065021.

4. **C.-L. Wong** and M. Palaniapan, Study of the long-term performance of micromechanical resonators using automated acoustic phonon detection technique, Measurement Science and Technology (submitted in January 2010, under review).

5. **C.-L. Wong,** M. Annamalai and M. Palaniapan, Characterization of nanomechanical graphene drum structures, Journal of Micromechanics and Microengineering 20 (2010) Art. no. 115029.

Conference proceedings

1. W.K. Wong, M. Palaniapan, **C.L. Wong**, S.R. Wang, F.E.H. Tay, Non-invasive acoustic phonon characterization of dynamic MEMS, in: Proceedings of the 32nd International Symposium for Testing and Failure Analysis (ISTFA), Austin, Texas, November 12–16, 2006, pp. 6–12.

2. W.K. Wong, **C.L. Wong**, M. Palaniapan, F.E.H. Tay, Non-destructive functionality and reliability assessment of dynamic MEMS using acoustic phonon characterization, in: Proceedings of the 14th International Conference on Solid-state Sensors, Actuators and Microsystems, Lyon, France, June 10–14, 2007, pp. 371–374.

3. **C.-L. Wong**, L.C. Shao, L. Khine, M. Palaniapan and W.K. Wong, Novel acoustic phonon detection technique to determine temperature coefficient of frequency in MEMS resonators, in: Proceedings of Eurosensors XXII, Dresden, Germany, September 7–10, 2008, pp. 429–432.

4. L.C. Shao, **C.-L. Wong**, L. Khine, M. Palaniapan and W.K. Wong, Study of various characterization techniques for MEMS devices, in: Proceedings of Eurosensors XXII, Dresden, Germany, September 7–10, 2008, pp. 1470–1473.

5. **C.-L. Wong** and M. Palaniapan, Characterization Techniques for NEMS/MEMS Devices, in: Proceedings of SPIE Smart Structures, Devices and Systems IV, Melbourne, Australia, December 10–12, 2008.

6. **C.-L. Wong** and M. Palaniapan, An acoustic phonon detection test setup for evaluating the frequency stability of clamped-clamped beam resonators, in: Proceedings of SPIE Photonics West MOEMS-MEMS 2009, San Jose, CA, USA, January 24–29, 2009.